THE UNIVERSITY OF CHICAGO

STRUCTURE-PROPERTY RELATIONSHIPS OF POLYELECTROLYTE COMPLEX MICELLES FOR TARGETED DELIVERY OF RNA TO ATHEROSCLEROTIC PLAQUES

A DISSERTATION SUBMITTED TO

THE FACULTY OF THE DIVISION OF THE PHYSICAL SCIENCES

IN CANDIDACY FOR THE DEGREE OF

DOCTOR OF PHILOSOPHY

DEPARTMENT OF CHEMISTRY

BY

MICHAEL JAMES MELLAS

CHICAGO, ILLINOIS

DECEMBER 2021

To my blockmates and 'bashmates, my family, and all the educators who supported my enthusiasm for science.

TABLE OF CONTENTS

LIST OF FIGURES

polydisperse ideal spheres. The -2 slope at high q agrees with an internal structural model of Gaussian neutral polymers, which also indicates that the polymer complexes are of overall neutralized charge. The Gaussian neutral polymer-like structure is a common feature of liquid PECs. The peak at q = 0.21 A^{-1} (red arrow) corresponds to a length scale of 3 nm, which is consistent the interhelix spacing resulting from parallel packing of DNA helices (cite Michael and toroid paper). The peak results from parallel packing of the double-stranded portion of the dhDNA, which is short enough to pack with PLK10 in the core (Also cite Michael). b) An example of wormlike nucleic acid/PEG-PLK micelles. QQQQQQQ-2k30 mixed with miR inhibitor (a dhRNA) fits to a flexible cylinder reasonably well, with a 7.3 nm radius and 23 nm Kuhn length. The calculated length is in excess of 1μm, indicating very long micelles. The -2 slope at low q is characteristic of wormlike chains. The fit underestimates the intensity at low q, indicating some degree of aggregation present. Note the -2 slope at high q is also present here, indicating the core behaves like Gaussian neutral polymers as in the spherical case and is likely liquid. Note the broad peak at q = 0.22 A^{-1} (red arrow) indicating that the PEC core exhibits interhelix packing of the RNA in the core of the wormlike micelles. 32

2.5. Aggregated nucleic acid/PEG-PLK micelles, modeled here as mass fractals. a) KKKKKKK-2k30/miR inhibitor fits a fractal polydisperse sphere model, as a mass fractal with a 2 nm sphere radius and aggregate size > 400 nm. Again we can observe the -2 slope at high q indicating Gaussian chain structure in a liquid core, and the broad peak at q = 0.22 A^{-1} (red arrow) indicating that the PEC core exhibits some interhelix packing of the RNA in the core. The low q behavior is not as well modeled, because the model assumes an infinitely large aggregate. At sufficiently large length scale, the scattering behavior becomes indistinguishable from that of smooth masses, and scatters with a lower power law. b) 10:1 volume fraction of Schulz spheres:fractal spheres. Sum model corrects fractal sphere radius to 1.6 nm, indicating that droplets in the core are very small and prone to

miR-92a expression in lung endothelial cells isolated from tamoxifen-injected *mi*R-*92a*$^{EC\text{-}TG}$/*Apoe*$^{-/-}$ mice compared to lung endothelial cells isolated from tamoxifen-injected *Cdh5(PAC)-CreERT2/ Apoe*$^{-/-}$ *(CDH5-Cre/ Apoe*$^{-/-}$*)*mice (n= 4-5 biological samples). *(D)* Increased miR-92a expression in the endothelium-enriched intima of carotid artery in tamoxifen-injected *mi*R-*92a*$^{EC\text{-}TG}$/*Apoe*$^{-/-}$ mice compared to tamoxifen-injected *CDH5-Cre/Apoe*$^{-/-}$ mice (n= 7 biological samples). *(E, F)* Reduced atherosclerosis in the aortic root in tamoxifen-injected *mi*R-*92a*$^{EC\text{-}TG}$/*Apoe*$^{-/-}$ mice compared to tamoxifen-injected *CDH5-Cre/Apoe*-/- mice (n= 7 biological samples). *(G)* The plasma cholesterol was not significantly affected by endothelial miR-92a overexpression in tamoxifen-injected *mi*R-*92a*$^{EC\text{-}TG}$/*Apoe*$^{-/-}$ mice compared to tamoxifen-injected *CDH5-Cre/Apoe*$^{-/-}$ mice (n= 8 biological samples). Statistical significance determined by multiple unpaired one-tailed t-test. All error bars are means ± standard deviation. n.s., not significant. *P ≤ 0.05; **P ≤ 0.01; ***P ≤ 0.001. 90

5.2 The formulation and characterizations of VCAM1-targeting polyelectrolyte complex micelles which encapsulate miRNA inhibitor. *(A)* The illustration of formation of VCAM1-targeting polyelectrolyte complexes encapsulating miRNA inhibitors in the core. *(B)* Condensation of miRNA inhibitor by the VHPKQHR-PEG-K30 at the mass ratio (polymer/miRNA inhibitor) of 2 or above demonstrated by an agarose gel retardation assay. *(C)* Encapsulation of miRNA inhibitor by the VHPKQHR-PEG-K30 demonstrated by the EthBr competitive binding assay. *(D)* Zeta potentials of the VHPKQHR-PEG-K30 and VCAM1-tageting micelles encapsulating miRNA inhibitor (n= 3). *(E)* Isothermal titration calorimetry (ITC) therogram of the assembling of VCAM1-targeting polyelectrolyte complex micelles encapsulating miRNA inhibitor. *(F)* A transmission electron microscopy (TEM) image of miRNA inhibitor encapsulated, VCAM1- targeting polyelectrolyte complex micelles in dry condition. *(G)* The hydrodynamic diameter of the miRNA inhibitor-encapsulated, VCAM1-targeting polyelectrolyte complex micelles. Statistical significance determined

LIST OF TABLES

ACKNOWLEDGEMENTS

Coming to the end of this road, I have such complicated thoughts about the journey. I was told there really is nothing like a Ph.D., that the experience is arduous but rewarding. I'm inclined to agree: truly a once-in-a-lifetime experience! This doctoral study really feels like such a manifestation of the saying that no plan survives contact with the enemy. But that's the nature of the beast, that science so often goes completely sideways from what we expect, but that's where the discoveries are to be made. I think that is the most valuable lesson these years have taught me. Despite the pandemic, with perseverance I find myself at the threshold of scholarship and advancement of human knowledge, having but a small discovery to add for now and ready for new experiences and new problems to take on. Not an end, but a beginning. It has truly been a growth experience, and I am very grateful to everyone who has supported me on the way.

First of all, I thank my advisor, Professor Matthew Tirrell, for accepting me across departments into his group, for broadening my experience of chemistry and its applications, and supporting me all the way throughout. I thank my committee for their support and consideration of my defense: Professor Yun Fang, Professor Bozhi Tian, and Professor Ka Yee Lee. Many thanks to everyone in the Tirrell Group whom I learned from and worked with throughout: Eun Ji Chung, Lorraine Leon, Handan Acar, Blair Brettmann, John Barrett, Samanvaya Srivastava, Amanda Marciel, Jeffrey Vieregg, Sean Mao, Michael Lueckheide, Mathew Schnorenberg, Lu Li, Hao Wu, Jeffrey Ting, Adam Levi, Guilhem De Hoe, Angelika Neitzel, Harrison Paul, Whitney Fowler, Ge Zhang, Qiming He, Kaden Stevens, Carlos Medina Jimenez, Yu Tian, Alexander Marras, Dean Mastropietro, Siqi Meng, and Zhengjie Zhou. I thank my 'bashmates, Ada Palmer, Lauren Schiller, and Jonathan Sneed, for their friendship, for broadening my Ph.D. experience, for the scientific outreach and networking opportunities, for the many historical anecdotes and precedents to our current events, and for their support, understanding,

and generally putting up with me whenever it all got overwhelming. Special thanks to my mentors and friends Michael Lueckheide and Joseph Mastron, whose insight and knowledge of physical chemistry guided my experience and who have remained good friends at work and in life. So many thanks to Myung-Jin Oh, and Ru-Ting Huang, for their work in collaboration with us and for the *in vivo* work. Many thanks to the university staff who made much of my research possible: Maria Rubio, LaKesha Lloyd, Melinda Moore, Vera Dragisich, Phil Griffin and Tera LaVoie. Thank you also to Xiaobing Zuo of Beamline 12-ID-B at Argonne APS, without whom most of my work would not exist, and to Wei Chen, for extending the use of his lab for my peptide syntheses. I also thank my undergraduate mentees Arundhati Pillai and Ben Indeglia, for their work and company as we studied the behavior of our micelles. Thanks to my Ph.D. class friends Polina Navotnaya and Julia Zinkus for the many hours in the Kent basement studying and pushing each other through candidacy and beyond, and the many others for making the whole experience richer: Andriy, Luke, Becca, Austin, Jo, Tamara, Nick, Preston, Tom, Tim, Airi, among others. I thank the Vampyre Unicorns for their love and support throughout, especially while the pandemic was full-swing: Michael, Jennifer, Julie, Lauren, Jelle, Patrick, Aisha, Yifan, Naomi, and Naomi. I'm really looking forward to what the future brings!

Finally, I thank my family, my parents Carol and James Mellas, my brother Matthew, my sister Makayla, and the rest of my family for their love, support, and room to grow.

Chapter 1
Introduction

Dissertation Abstract

Polyelectrolyte complex (PEC) micelles are of immense therapeutic interest because of their ability to encapsulate nucleic acid and protect it from degradation. Formed by mixing the nucleic acid with a block copolymer of one neutral hydrophilic block and one charged block, the micelles can be injected as therapeutic agents to deliver the nucleic acid to an area of interest. PEC micelles are highly versatile, as a targeting moiety can be attached to the block copolymer modularly, allowing for a wide range of potential targets for the encased nucleic acid. To take advantage of this potential for modular design, and to understand the dynamics of the micelles *in vivo*, it is important to understand the fundamental structural properties of the micelles: their shape, size, and internal structure. Using small-angle X-ray scattering (SAXS) and light scattering, we can observe and characterize these properties in PEC micelles, and compare micelles of different assembly inputs such as nucleic acid structure, charged block length, neutral block length, salinity of solution, and charge of targeting moiety. Therefore, we can elucidate what properties influence the shape, size, and internal structure of the micelles. Then, I demonstrate that these micelles are an effective RNA delivery vehicle for the treatment of atherosclerosis, a chronic cardiovascular disease.

1.1 The aim of this research

The use of nanoparticles in biology and medicine is of great interest because of their potential in

pharmaceutical and surgical applications, but faces challenges of reliable and replicable assembly, delivery, biocompatibility and clearance. The scientific community has worked to address these challenges via several strategies, as well as to understand the trade-offs among these strategies, wherein one may be more suitable for some applications than others. There are multiple approaches to making functional nanoparticles, but our strategy of self-assembling peptides allows for quick and efficient synthesis using known solid-phase peptide synthesis methods that can make fixed-length polylysine while permitting attachment of PEG and other modular steps such as biologically active peptides, then followed by mixing with RNA to form polyelectrolyte-complex (PEC) micelles by taking advantage of the charges of lysine and nucleic acids. To evaluate the best applications for our synthesized particles, it is important to understand the shape and size of the particles we are making, so we employ light scattering methods such as dynamic light scattering (DLS) and small-angle X-ray scattering (SAXS), as well as visualization with transmission electron microscopy (TEM), to show that our micelles are appropriate for injectable delivery. Because of the modular design of our PEG-polylysine micelles, it is possible to encapsulate RNA as a functional part of the PEC micelle core while functionalizing the micelle surface with ligands targeting specific tissues, and here we demonstrate that such a strategy successfully reduces plaque load in mouse models of atherosclerosis by delivering miR92a inhibitor.

1.2 Micelles for Materials Delivery

Our work utilizes nanoscale micelles for treatment. Micelles consist of a monolayer of material surrounding a phase-separated structure. Engineered micelles are studied because the layer of separation allows for protected delivery of materials in the phase-separated core or in the encapsulation layer itself, while allowing nearly orthogonal manipulation of targeting moieties on the

outer surface for specific active targeting. These properties permit a high degree of modularity in the engineering of the micelles, which can be of use for developing a platform for multiple diseases of interest[1].

1.2.1 Strategies for Achieving Polymer-Based Nanoparticle Assembly

There are three important properties to consider when designing a polymer to be a micelle envelope. First, what is the target, and how will the micelle target it? Second, what is the payload, and how will it be protected in the core of the micelle? Finally, how will the micelle remain stable until it reaches the target, then make its payload available for effect? Much of our knowledge addressing these questions has been discovered through chemotherapy delivery research. Most small-molecule chemotherapy is toxic and systemic, leading to a wide array of off-target effects in a patient. Therefore, developing systems to contain chemotherapy drugs and localize their release has drawn much attention, especially in cases where the tumor is not solid and cannot be injected into directly. Like many small-molecule drugs, chemotherapeutics are generally hydrophobic, and solubilize poorly in the body. However, their hydrophobicity becomes an advantage for crossing the bilayer of the cell membrane once they have reached the tumor site, so delivery strategies have focused on using amphiphilic polymers that will self-assemble via the hydrophobic effect[2,3] and solubilize the drug in the hydrophobic core, but remain hydrophilic at the surface of the vesicle shell to remain soluble and take advantage of passive targeting.

Israelachvili's theoretical work laid the foundations for describing and predicting the shape of self-assembled amphiphilic molecules. Importantly, he described the packing parameter[4,5] for controlling the shape of amphiphile micelles, which takes the form of the equation $P = v_0/al$, where v_0 is the Van der Waals volume of the amphiphile, a is the area subtended by the hydrophilic head, and l is the length of the hydrophobic tail. In other words, P describes the fraction of the hypothetical

cylinder that circumscribes the amphiphile that is physically occupied by the amphiphile in the assembled structure. At values near $P = 1/3$, the amphiphile is roughly conical, so the resulting assembly is spherical. Near $P = 1/2$, the assembly is more wormlike or cylindrical. Finally, near $P = 1$, the resulting assembly forms bi- or multilayer vesicles.

Earlier attempts at drug delivery used a hydrocarbon, monoglyceride or diglyceride attached to a hydrophilic moiety, most often polyethylene glycol (PEG). PEG was initially used for its hydrophilic properties, but as it became clear that PEG could also evade immune response, it has remained a mainstay of vesicle design. The PEG could also be functionalized with MRI-contrast complexes, which opened research opportunities in diagnostics. Harrington et al.[6] showed that it was possible to target solid tumors in the clinic with ^{111}In-labeled PEGylated liposomes, which would accumulate at tumor sites. Viglianti et al.[7] showed similarly that it was possible to track the location and concentration of liposomal chemotherapy by loading the liposomes with both doxorubicin and Mn contrast agent, because the liposomes could retain both at the same time. More recently, Chung et al.[8] explored atherosclerosis as another diagnostic application, demonstrating targeted delivery of 1,2-distearoyl-*sn*-glycero-3-phosphoethanolamine-PEG (DSPE-PEG) micelles to monocytes involved in chronic disease, which Yoo et al.[9] was able to develop upon by localizing Gd-labeled DSPE-PEG micelles to atherosclerotic lesions to assess likelihood of rupture. Given the tunability of the PEG, it became worthwhile to try a hydrophobic polymer as well, rather than a small molecule. After finding some success with polyesters such as poly(lactic acid) (PLA), poly(lactic-*co*-glycolic acid) (PLGA), and polycaprolactone (PCL)[10], the scientific community began to research new applications as well as more complex formulations[11]. Earlier study of PEG-polyesters focused on gel-like materials for use as scaffolds in tissue engineering of bone, cartilage, skin, and nerves[10]. However, PEG-polyesters that assembled into nanoparticles presented an opportunity to study drug delivery with

these materials. Using PEG-PCL micelles, Cho et al.[11] was demonstrated that delivering a cocktail of chemotherapy drugs to ovarian cancer-xenografted mice in a micelle formulation could increase the efficacy of the cocktail even as *in vitro* it was shown to have little additional effect over exposure to the non-encapsulated drugs, which suggested that the additional efficacy of the micelle formulation *in vivo* was caused by colocalization and concentration of the drugs within the micelle. The polyester-PEG amphiphilic block copolymers gave researchers a highly versatile tool which could be used in a wide variety of applications ranging from therapeutics to drug delivery to tissue regeneration[10,12–14].

In chemotherapy delivery, research initially focused on the enhanced permeation-retention (EPR) effect[15,16]. The EPR effect describes a phenomenon wherein disruptions of local vasculature allow increased interstitial fluid to permeate tumor sites, which then retain the fluid for extended periods of time relative to normally functioning tissue. The retention creates a passive localization, increasing the local availability of solubilized nutrients or, to our advantage, drugs. Furthermore, the separation of the drug from the environment provides protection from metabolic breakdown before reaching the target site. More recently, the EPR effect has come under contention[17,18], as our understanding of tumors developed further and challenged our assumptions (Figure 1.1). The original proposal assumed that drug carriers were able to permeate through relatively uniform gaps in the tissue surrounding the tumor, and that the tumor itself was relatively homogenous. However, the gaps are not uniform, and tumors are better understood to be composed of multiple clustered populations of tumor cells of variable phenotype and susceptibility to the drug. The nonuniform distribution of the tumor cells and the surrounding tissue create pockets where the drug cannot accumulate, reducing the effect of passive targeting. The EPR effect is mainly only seen at sites of vascular leakage, so other strategies are necessary to achieve drug accumulation where vasculature is not leaky. To improve drug delivery, active targeting has emerged as a promising strategy. The main

challenge is identifying and synthesizing a targeting moiety that improves delivery, does not accumulate or cause toxicity, and is readily attached to the carrier. The functionality of PEG provides an opportunity to attach biological ligands instead of chelation moieties. With some effort, the scientific community has discovered how to functionalize amphiphiles with biologically active peptides capable of binding specific cell receptors on tumors[19–21], immune cells[8,22–26], bone and connective tissue[13], and vasculature[27]. To briefly illustrate the extent of the work in the field of active targeting and delivery, Accardo demonstrated the use of the cholecystokinin hormone as the

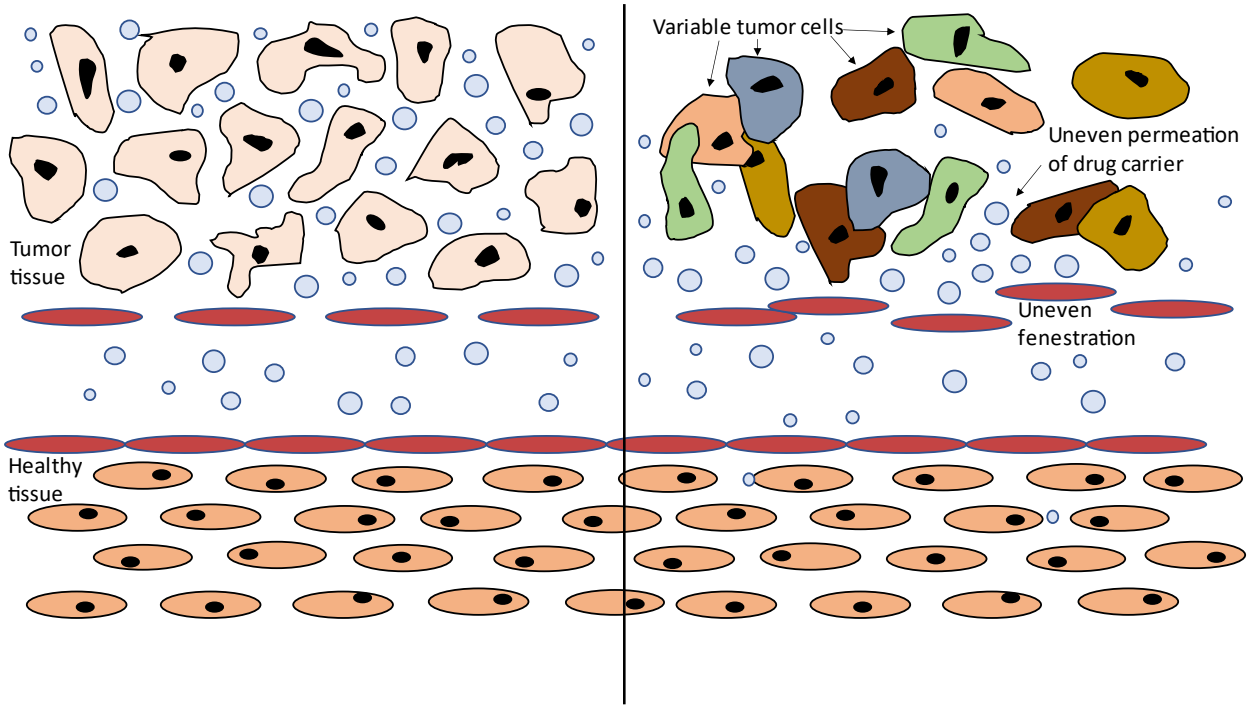

Figure 1.1. EPR schemes as originally proposed (left) and as currently understood (right). While there is some retention, variable flow disruption and tissue density at tumor sites cause uneven permeation. Originally, the effect was thought to operate via entry of drug carriers through porous fenestrations of the tissue surrounding the tumor when in fact, the fenestrations are of variable size. The tumors are also now best understood as a mixture of many variants, each with a different susceptibility to the drug. These effects make clear that while EPR does occur, often passive targeting is insufficient to deliver an effective dose of drug.

hydrophilic component of an amphiphilic assembly, to be used as a biological ligand, and showed that the resulting nanostructures could sequester chemotherapy drugs for delivery[19]. Javali et al.

showed similarly that C18-PEG-RGD micelles could be loaded with paclitaxel, and also that the loaded micelles could deliver toxic concentrations of paclitaxel to tumor cells *in vitro* with increased efficacy[20]. Chung, during her work in the Tirrell group, showed that fibrin-binding REKA peptide could be conjugated to DSPE-PEG to form fibrin-binding micelles that could localize at fibrin deposits at glioblastoma sites, for potential labelling or drug delivery[21], work that would inform the group's future work in active targeting of tissues involved in atherosclerosis, including fibrin, monocytes[8], and endothelial tissue[27]. Research of active targeting is also closely related to vaccination research, with the subtle difference that rather than use the surface peptide as a binding ligand for targeted delivery of an encapsulated payload, the surface peptide itself is used as an immunogenic epitope and the nanoparticle is a means of concentrating that epitope locally, like a viral protein shell. Indeed, some vaccination strategies refer to their approach as "Virus-like particles," because of the resemblance to actual viruses but without the internal nucleic acid necessary for replication. The advantage of the nanoparticles is that the concentration of antigen peptides available can stimulate the immune system against pathogens that normally are difficult to develop immunity to because they evade immune response. The approach shows great promise towards vaccinating against malaria[23,25,28], and there are active efforts to develop immunogenicity against tumors[22] and *Streptococcus* infection[24]. The scientific community has also shown that peptide amphiphiles can be used to combine therapeutic and diagnostic function, for example with a chelator amphiphile for MRI imaging as seen in the earlier example of Viglianti et al.[7]. A similar approach was taken by Xiao et al.[29], using poly-L-glutamate-PEG to load doxorubicin into the micelle and chelate ^{64}Cu for PET imaging, and Peters et al.[30], using fluorescently labeled DSPE-PEG-CREKA micelles loaded with hirulog, an anticoagulant, to treat atherosclerotic plaques. These examples show that micelles can be synthesized to target a specific tissue, release their contents where most effective, and be imageable in real time. Their

multifunctionality and modularity is a highly desirable outcome for the investment of time and resources to design them precisely.

1.2.2 Challenges of RNA Delivery

Recently, with the rise of biologics as therapeutic agents, encapsulation in micelles provides a potential strategy to deliver biomolecules and macromolecules via active targeting. While the COVID-19 pandemic and resulting mRNA vaccines have renewed interest in the subject, the scientific community has exerted much effort into RNA delivery, a foundation that indeed has borne fruit in the pandemic. The efforts toward effective RNA delivery stem both from the challenges incumbent to RNA stability, and from the potential applications that RNA is uniquely suited to address. RNA is a potent and versatile molecule in biology. Its most well-known function is as messenger (mRNA) from the genetic library of DNA in a cell to the protein manufacturing machinery of the ribosomes. Its chemical properties allow it to be a highly dynamic molecule, and part of the function of its noncoding regions is to control its stability and expression during protein synthesis, providing a very fine modulation of gene expression at the pre-protein level. This is further bolstered by other functions of RNA *in vivo* such as interfering RNA which can bind mRNA to reduce protein expression, and transfer RNA whose affinity for mRNA during protein synthesis can also play a role in overall expression. Commonly, viruses carrying their genetic structure as RNA will use these properties to maximize reproduction in cells, which in turn has generated defenses to foreign RNA. Many of the stability challenges of RNA delivery stem from the 2' alcohol (-OH) group that distinguishes it from DNA (Figure 1.2). The 2'-OH is nucleophilic, and in the right conditions can bind the 3' carbon on the ribose ring, cleaving the backbone via autolysis. On any RNA molecule, this autolysis threat can manifest anywhere along the sequence. Autolysis typically occurs chemically in the presence of divalent cations (e.g. Mg^{2+}, Ca^{2+}) or at pH > 9, and is catalytic, so care must be

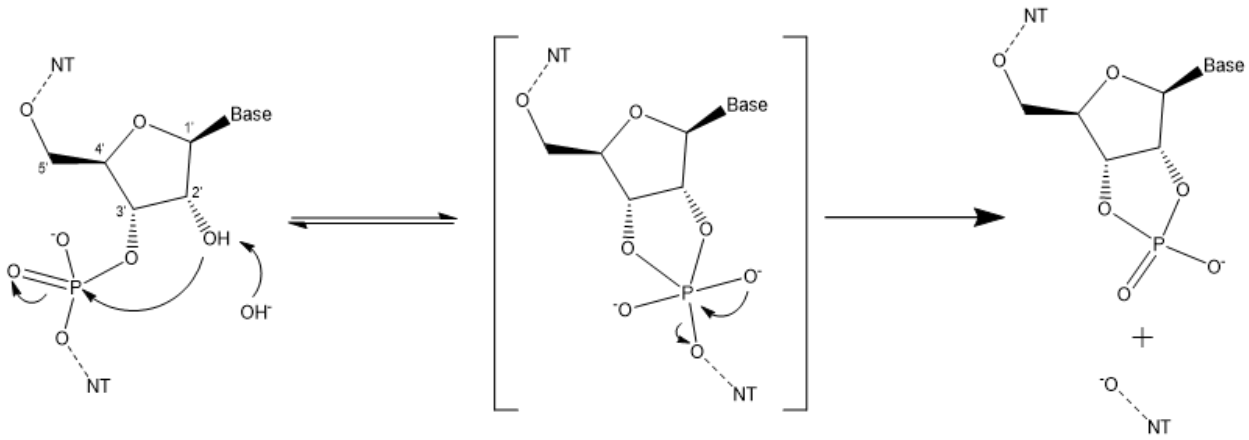

Figure 1.2. RNA degradation scheme. RNA is far more labile than DNA because of the 2' alcohol of the ribose, which can autohydrolyze the polynucleotide. The hydrolysis is catalyzed by basic pH, which increases $[OH]^-$, deprotonating the alcohol and driving nucleophilic attack of the phosphate bridge to yield the cyclic intermediate (middle picture). Divalent cations (Mg^{2+}, Ca^{2+}) stabilize the dianionic intermediate, and can drive hydrolysis at elevated temperatures (> 50°C). Therefore, preparations of micelles are made in pH < 9 buffered solution free of divalent cations. One must also take care to keep conditions Rnase-free, to prevent enzymatic hydrolysis.

taken to avoid exposing the RNA to these conditions. Furthermore, the near-universally present biological defense against foreign RNA, the aptly named RNase enzyme, is unusually stable owing to its eight disulfide bonds, so preparations to work with RNA must include disulfide oxidation on working surfaces and RNase-free solvent. Additional challenges await post-injection, which is where vesicle-based delivery can aid stability most. First, additional nucleases are retained to break down free-floating RNA and DNA outside cells. Similar to viruses, RNA within vesicles is shielded from breakdown by these nucleases. Second, RNA molecules can trigger immune reactions, so nanoparticles, especially PEGylated nanoparticles, can protect RNA cargo from the immune system during delivery. Finally, RNA is a large, charged molecule that will not easily enter through a cell membrane, so a nanoparticle is necessary to assist RNA transfection. However, the strong negative charge of RNA presents another problem: it is too hydrophilic to keep in the core of an amphiphilic nanoparticle. A different approach is required to shield the RNA successfully in a nanoparticle core.

1.2.3 Hydrophilic Phase Separation: Polyelectrolyte Complex (PEC) Coacervation

The negative charge of RNA also presents an opportunity to use a polycation to condense the RNA in the core of a particle and neutralize its charge. Using design principles for block copolymers, the scientific community focused on making polycationic polymers such as polyethyleneimine, polylysine, and polyarginine. Mixing RNA or DNA with a polycation condenses it, driving liquid-liquid phase separation, or coacervation[31]. Attaching a neutral block like PEG yields micelles with the condensed nucleic acid in the core with the polycation, enveloped by a PEG layer. Polycations can also overcome the other major challenge to transfection, endocytosis. Endocytosis is the major nutrient uptake mechanism for a cell, in which the cell depresses part of its membrane to form a vesicle within the cytosol, which is then oxidized to digest the materials within to monomers before final release into the cell. To prevent digestion of the nucleic acid, the polymer vesicle must be capable of disrupting endocytosis to allow escape, and the polycation can assist that escape. Some polycations are self-sufficiently capable of effecting endosomal escape[32], but as with toxicity, endosomal escape is largely determined empirically using overall transfection as a proxy or using fluorescence measurements. To improve transfection when cationic polypeptides like polyarginine or polylysine have poor escape properties, a common first step is to add histidine to the synthetic scheme[33–35]. Endosomes acidify as they process their contents, crossing the pKa of histidine and allowing it to neutralize the acidification. The endosome compensates with additional acidification, but the excess water uptake in the process swells the endosome to bursting, releasing its contents and allowing escape. This process driven by histidine or other molecules[36–38] with similar pKa is known as the "proton-sponge effect." Besides histidine, other strategies exist to take advantage of the acidification, for example acid-labile polymers that can release their cargo during endosomal escape[39]. The cationic block can be further refined to

address challenges that arise after the nucleic acid is delivered. Of special importance are toxicity and endosomal escape. The amphiphilic bilayer of cell membranes is anionic on the outside, and polycations can condense on the cell membrane and disrupt the bilayer. While this can be advantageous for delivering nucleic acids into a cell, it can also promote unwanted apoptosis and other toxic effects[32,40,41]. Toxicity concerns played a major role in the overall movement from PEI to polypeptide cations, because peptides are readily metabolized *in vivo*[31], but otherwise it is not always obvious what may or may not induce toxic effects. Designed well, polycations can induce effective nucleic acid delivery while avoiding toxicity. The most straightforward is oligoarginine, a strong polyelectrolyte peptide with low toxicity, although it has been observed to induce actin rearrangement to unknown effect[40,42]. Also, while oligoarginine successfully traffics nucleic acids into cells, its major drawback is poor endosomal escape. Thus, the usual approaches to balance cell penetration and endosomal escape lead to oligoarginine-oligohistidine designs that can exhibit proton-sponge effects. Using this design, labs have demonstrated transfection of genetic DNA[43,44] and small interfering RNA (siRNA)[34]. Chu et al. further found that that gene silencing from siRNA transfection was more effective with higher histidine/arginine ratios, emphasizing the importance of endosomal escape to effective transfection. Other cell-penetrating peptides include HIV-derived Tat peptide[40,45], branched oligoethylenimine[46], and poly(diethylamino aspartamide)[36,37]. Polypeptides provide an approach to transfection that combines the cell-penetrating capacity of surface oligocationic peptides and core polyelectrolyte complexation, creating positively-charged complexes with high transfection rates. Read developed polylysine/DNA polyplexes with oligohistidine, showing that the histidine-enriched polyplexes achieved near-quantitative transfection[33]. Kim et al. demonstrated siRNA transfection by making a PEC with polyarginine-PEG, before mixing with a cationic liposome for delivery[47]. Kuo et al. demonstrated that PEG-polylysine/microRNA complexes formed micelles that could knock down

atherosclerosis-promoting gene expression, without use of histidine[48].

1.2.4 Design Principles of Polyelectrolyte Complex Micelles Versus Amphiphilic Micelles

As researchers of polyelectrolyte self-assembly have attempted to understand how the polymer structure affects the dynamics of assembly, there has been sustained interest in developing rational design principles for PEC micelles. One starting point for rational PEC design is to look at the principles guiding amphiphilic design, as both involve phase separation. The elegance of the packing parameter[2] as a metric for micelle shape also drives the search for a similarly elegant PEC design principle. However, it has been reported[49–53] that while the entropic forces driving phase separation of the core in PEC micelle assembly resemble the hydrophobic force driving phase separation of amphiphile micelles, the systems have a number of key differences. While block size in the copolymer, and the structure of the nucleic acid, do affect size and shape, the structure-assembly relationship of core composition seems to be more complex than in the amphiphile case. The most important influence of PEC micelle shape is whether the nucleic acid is single- or double-stranded, with single-stranded nucleic acid forming spheroid micelles and double-stranded nucleic acid forming thin worms or failing to assemble. Attempts by the Kataoka group to resolve this shape dependence proposed that the rigidity of double-stranded nucleic acid[54,55] plays a key role in frustrating potential micelle assembly, finding that PEG-polylysine PECs would form micelles only when associated with single-stranded RNA[52]. Subsequent work in the Tirrell group showed that double-stranded RNA that was partially methoxylated to reduce the backbone charge to parity with single-stranded RNA was capable of forming spheroidal micelles, suggesting that the shape of the micelle appears to driven by core polymer charge density rather than RNA strand rigidity[49,50], with higher charge density corresponding to formation of wormlike and lamellar vesicles. Furthermore,

they showed that the shape of the micelles correlated to the nature of the phase separation in the core, with double-stranded RNA forming solid precipitates in the core when mixed with polylysine, and single-stranded or charge-reduced double-stranded RNA forming liquid coacervate cores. Theoretical work has shown that the salt concentration of a PEC micelle solution can also influence the shape of the micelles, with higher salt concentrations promoting wormlike micelles or lamellae[51]. Given what we know of assembly, the packing parameter seems insufficient to describe the shape that arises from PEC assembly, necessitating characterization of PEC micelles, but there are nonetheless some design principles that we can employ in our design of RNA-encapsulating micelles.

1.3 The Challenge of Atherosclerosis

We are interested in engineering a delivery platform capable of targeting and treating diseases using RNA interference. Our primary focus, atherosclerosis, is a silent killer, usually developing over many years before precipitating acute and often deadly cardiovascular events like heart attack and stroke. Methods to prevent or reverse the development of atherosclerosis are therefore of great interest.

1.3.1 Biology of Atherosclerotic Plaque Development

Atherosclerosis is complex, chronic disease identifiable by the characteristic formation of fatty plaques in arterial endothelial tissue. Initial inflammatory events driven by disruption of the shear flow of the blood[56] can disrupt cholesterol efflux[57] and induce monocyte and neutrophil recruitment[58] as the immune response attempts to resolve the disruption. Monocytes absorb fatty deposits in the endothelial tissue, but are ill-equipped to remove them, instead taking on a foamy appearance as they undergo apoptosis[59]. These "foam cells" accumulate and further contribute to inflammation, creating

a positive feedback loop that leads to the slow accumulation of apoptotic and necrotic cells within the endothelium[60]. As the plaque further develops, platelet recruitment to the site of the necrotic core creates a fibrous cap over the plaque[61]. Eventually, the fibrous cap can thin and rupture, causing further cardiovascular events like heart attack and stroke[62]. Plaques are most prevalent at the aortic arch and branching arteries near the heart, where the local blood pressure tends to produce turbulent flow. The relative absence of plaques at sites of undisturbed laminar flow suggest that PPAP2b inactivation causes the inflammatory conditions needed for atherosclerosis to develop, by way of Kruppel-like Factor 2 (KLF2) inactivation[63]. KLF2 expression in this pathway is regulated by microRNA-92a (miR-92a), and knockdown of miR-92a expression at the plaque site has been shown to rescue KLF2 expression, reduce foam cell-mediated inflammation and restore healthy arterial function[64–66].

1.3.2 Engineering Normal Arterial Function

The key to preventing or reversing plaque progression is to stop the vicious cycle of foam cell formation and monocyte recruitment. Earlier treatment focused on preventing the initial fatty deposits from allowing foam cell formation, using drugs like statins that can induce cholesterol efflux. Delivering an RNA inhibitor of miR-92a is a promising possibility, but it must be protected from degradation or immune response *en route* to the plaque site. Furthermore, the flow dynamics of the aorta demand an active targeting approach. PEG-polylysine (PEG-PLK) block copolymers can deliver on that promise by assembling with the miR-92a inhibitor to form PEC micelles, which can be injected as possible treatment. Targeting of the arterial inflammation is a possible approach, and for prevention of early plaque prevention, elevated VCAM1 expression is a promising target[67–69]. The peptide sequence VHPKQHR has been shown to bind VCAM-1[70], and earlier work by Yun Fang in collaboration with the Tirrell group has shown that VHPKQHR-PEG-PLK PECs can successfully target atherosclerotic plaques and deliver miR-92a inhibitor RNA[48]. My work will demonstrate the

versatility of the block copolymer synthesis, some of the range of assembly dynamics, and finally, with the collaboration of the Fang group, show the effectiveness of VHPKQHR-PEG-PLK for delivery of miR-92a inhibitor to plaque sites *in vivo*.

Chapter Bibliography

1. Blanazs, A., Armes, S. P. & Ryan, A. J. Self-Assembled Block Copolymer Aggregates: From Micelles to Vesicles and their Biological Applications. *Macromol. Rapid Commun.* **30**, 267–277 (2009).
2. Israelachvili, J. N. *Intermolecular and surface forces*. (Academic Press, 2011).
3. Maibaum, L., Dinner, A. R. & Chandler, D. Micelle Formation and the Hydrophobic Effect. *J. Phys. Chem. B* **108**, 6778–6781 (2004).
4. Israelachvili, J. N., Mitchell, D. J. & Ninham, B. W. Theory of self-assembly of lipid bilayers and vesicles. *BBA - Biomembr.* **470**, 185–201 (1977).
5. Nagarajan, R. Molecular packing parameter and surfactant self-assembly: The neglected role of the surfactant tail. *Langmuir* **18**, 31–38 (2002).
6. Harrington, K. J. *et al.* Effective Targeting of Solid Tumors in Patients With Locally Advanced Cancers by Radiolabeled Pegylated Liposomes. *Clin. Cancer Res.* **6**, 2528–37 (2000).
7. Viglianti, B. L. *et al.* Chemodosimetry of in vivo tumor liposomal drug concentration using MRI. *Magn. Reson. Med.* **56**, 1011–1018 (2006).
8. Chung, E. J. *et al.* Monocyte-Targeting Supramolecular Micellar Assemblies: A Molecular Diagnostic Tool for Atherosclerosis. *Adv. Healthc. Mater.* **4**, 367–76 (2015).
9. Yoo, S. P. *et al.* Gadolinium-Functionalized Peptide Amphiphile Micelles for Multimodal Imaging of Atherosclerotic Lesions. *ACS omega* **1**, 996–1003 (2016).
10. Kutikov, A. B. & Song, J. Biodegradable PEG-Based Amphiphilic Block Copolymers for Tissue Engineering Applications. *ACS Biomater. Sci. Eng.* **1**, 463–480 (2015).
11. Cho, H., Lai, T. C. & Kwon, G. S. Poly(ethylene glycol)-block-poly(ε-caprolactone) micelles

for combination drug delivery: Evaluation of paclitaxel, cyclopamine and gossypol in intraperitoneal xenograft models of ovarian cancer. *J. Control. Release* **166**, 1–9 (2013).

12. Smart, T. *et al.* Block copolymer nanostructures. *Nano Today* **3**, 38–46 (2008).
13. Monteiro, N., Martins, A., Reis, R. L. & Neves, N. M. Nanoparticle-based bioactive agent release systems for bone and cartilage tissue engineering. *Regen. Ther.* **1**, 109–118 (2015).
14. Cui, H., Webber, M. J. & Stupp, S. I. Self-assembly of peptide amphiphiles: from molecules to nanostructures to biomaterials. *Biopolymers* **94**, 1–18 (2010).
15. Matsumura, Y. & Maeda, H. A New Concept for Macromolecular Therapeutics in Cancer Chemotherapy: Mechanism of Tumoritropic Accumulation of Proteins and the Antitumor Agent Smancs. *Cancer Res.* **46**, 6387–6392 (1986).
16. Maeda, H. Macromolecular therapeutics in cancer treatment: The EPR effect and beyond. *J. Control. Release* **164**, 138–144 (2012).
17. Nichols, J. W. & Bae, Y. H. EPR: Evidence and fallacy. *J. Control. Release* **190**, 451–464 (2014).
18. Danhier, F. To exploit the tumor microenvironment: Since the EPR effect fails in the clinic, what is the future of nanomedicine? *J. Control. Release* **244**, 108–121 (2016).
19. Accardo, A., Tesauro, D., Mangiapia, G., Pedone, C. & Morelli, G. Nanostructures by self-assembling peptide amphiphile as potential selective drug carriers. *Biopolymers* **88**, 115–121 (2007).
20. Javali, N. M., Raj, A., Saraf, P., Li, X. & Jasti, B. Fatty acid-RGD peptide amphiphile micelles as potential paclitaxel delivery carriers to αvβ3integrin overexpressing tumors. *Pharm. Res.* **29**, 3347–3361 (2012).
21. Chung, E. J. *et al.* Fibrin-binding, peptide amphiphile micelles for targeting glioblastoma. *Biomaterials* **35**, 1249–56 (2014).
22. Black, M. *et al.* Self-assembled peptide amphiphile micelles containing a cytotoxic T-cell

epitope promote a protective immune response in vivo. *Adv. Mater.* **24**, 3845–3849 (2012).

23. Ghasparian, A. *et al.* Engineered synthetic virus-like particles and their use in vaccine delivery. *ChemBioChem* **12**, 100–109 (2011).

24. Trent, A. *et al.* Peptide Amphiphile Micelles Self-Adjuvant Group A Streptococcal Vaccination. *AAPS J.* **17**, 380–388 (2015).

25. Moon, J. J. *et al.* Enhancing humoral responses to a malaria antigen with nanoparticle vaccines that expand Tfh cells and promote germinal center induction. *Proc. Natl. Acad. Sci.* **109**, 1080–1085 (2012).

26. Poon, C. *et al.* Protein Mimetic and Anticancer Properties of Monocyte- Targeting Peptide Amphiphile Micelles. *ACS Biomater. Sci. Eng.* **91**, 165–171 (2015).

27. Mlinar, L. B., Chung, E. J., Wonder, E. A. & Tirrell, M. Active targeting of early and mid-stage atherosclerotic plaques using self-assembled peptide amphiphile micelles. *Biomaterials* **35**, 8678–8686 (2014).

28. Boato, F. *et al.* Synthetic virus-like particles from self-assembling coiled-coil lipopeptides and their use in antigen display to the immune system. *Angew. Chemie - Int. Ed.* **46**, 9015–9018 (2007).

29. Xiao, Y. *et al.* Multifunctional unimolecular micelles for cancer-targeted drug delivery and positron emission tomography imaging. *Biomaterials* **33**, 3071–82 (2012).

30. Peters, D. *et al.* Targeting atherosclerosis by using modular, multifunctional micelles. *Proc. Natl. Acad. Sci.* **106**, 9815–9819 (2009).

31. Gaucher, G. *et al.* Block copolymer micelles: preparation, characterization and application in drug delivery. *J. Control. Release* **109**, 169–188 (2005).

32. Islam, M. A. *et al.* Major degradable polycations as carriers for DNA and siRNA. *J. Control. Release* **193**, 74–89 (2014).

33. Read, M. L. *et al.* A versatile reducible polycation-based system for efficient delivery of a broad range of nucleic acids. *Nucleic Acids Res.* **33**, 1–16 (2005).

34. Chu, D. *et al.* Rational modification of oligoarginine for highly efficient siRNA delivery: Structure-activity relationship and mechanism of intracellular trafficking of siRNA. *Nanomedicine Nanotechnology, Biol. Med.* **11**, 435–446 (2015).

35. Mann, A. *et al.* Linear short histidine and cysteine modified arginine peptides constitute a potential class of DNA delivery agents. *Mol. Pharm.* **11**, 683–696 (2014).

36. Uchida, S. *et al.* In Vivo Messenger RNA Introduction into the Central Nervous System Using Polyplex Nanomicelle. *PLoS One* **8**, (2013).

37. Uchida, H. *et al.* Modulated protonation of side chain aminoethylene repeats in N-substituted polyaspartamides promotes mRNA transfection. *J. Am. Chem. Soc.* **136**, 12396–12405 (2014).

38. Zhou, J. *et al.* PH-Sensitive Nanomicelles for High-Efficiency siRNA Delivery in Vitro and in Vivo: An Insight into the Design of Polycations with Robust Cytosolic Release. *Nano Lett.* **16**, 6916–6923 (2016).

39. Peeler, D. J., Sellers, D. L. & Pun, S. H. PH-Sensitive Polymers as Dynamic Mediators of Barriers to Nucleic Acid Delivery. *Bioconjug. Chem.* **30**, 350–365 (2019).

40. Verdurmen, W. P. R. & Brock, R. Biological responses towards cationic peptides and drug carriers. *Trends Pharmacol. Sci.* **32**, 116–124 (2011).

41. Chen, J., Wang, K., Wu, J., Tian, H. & Chen, X. Polycations for Gene Delivery: Dilemmas and Solutions. *Bioconjug. Chem.* **30**, 338–349 (2018).

42. Nakase, I. *et al.* Interaction of arginine-rich peptides with membrane-associated proteoglycans is crucial for induction of actin organization and macropinocytosis. *Biochemistry* **46**, 492–501 (2007).

43. Vázquez, E., Ferrer-Miralles, N. & Villaverde, A. Peptide-assisted traffic engineering for

nonviral gene therapy. *Drug Discov. Today* **13**, 1067–1074 (2008).

44. Unzueta, U. *et al.* Sheltering DNA in self-organizing, protein-only nano-shells as artificial viruses for gene delivery. *Nanomedicine Nanotechnology, Biol. Med.* **10**, 535–541 (2014).

45. Kanazawa, T., Akiyama, F., Kakizaki, S., Takashima, Y. & Seta, Y. Delivery of siRNA to the brain using a combination of nose-to-brain delivery and cell-penetrating peptide-modified nano-micelles. *Biomaterials* **34**, 9220–9226 (2013).

46. Klein, P. M. & Wagner, E. Bioreducible Polycations as Shuttles for Therapeutic Nucleic Acid and Protein Transfection. *Antioxid. Redox Signal.* **21**, 804–817 (2014).

47. Kim, H. K., Davaa, E., Myung, C. S. & Park, J. S. Enhanced siRNA delivery using cationic liposomes with new polyarginine-conjugated PEG-lipid. *Int. J. Pharm.* **392**, 141–147 (2010).

48. Kuo, C. H. *et al.* Inhibition of atherosclerosis-promoting microRNAs via targeted polyelectrolyte complex micelles. *J. Mater. Chem. B* **2**, 8142–8153 (2014).

49. Lueckheide, M., Vieregg, J. R., Bologna, A. J., Leon, L. & Tirrell, M. V. Structure−Property Relationships of Oligonucleotide Polyelectrolyte Complex Micelles. *Nano Lett.* **18**, 7111–7117 (2018).

50. Vieregg, J. R. *et al.* Oligonucleotide−Peptide Complexes: Phase Control by Hybridization. *J. Am. Chem. Soc.* **140**, 1632–1638 (2018).

51. Rumyantsev, A. M., Zhulina, E. B. & Borisov, O. V. Scaling Theory of Complex Coacervate Core Micelles. *ACS Macro Lett.* **7**, 811–816 (2018).

52. Hayashi, K. *et al.* Influence of RNA Strand Rigidity on Polyion Complex Formation with Block Catiomers. *Macromol. Rapid Commun.* **37**, 486–493 (2016).

53. Kim, Y. G., Park, H. J., Kim, K. K., Lowenhaupt, K. & Rich, A. A peptide with alternating lysines can act as a highly specific Z-DNA binding domain. *Nucleic Acids Res.* **34**, 4937–4942 (2006).

54. Abels, J. A., Moreno-Herrero, F., Van Der Heijden, T., Dekker, C. & Dekker, N. H. Single-molecule measurements of the persistence length of double-stranded RNA. *Biophys. J.* **88**, 2737–2744 (2005).

55. Hyeon, C., Dima, R. I. & Thirumalai, D. Size, shape, and flexibility of RNA structures. *J. Chem. Phys.* **125**, 194905 (2006).

56. Davies, P. F., Civelek, M., Fang, Y. & Fleming, I. The atherosusceptible endothelium: Endothelial phenotypes in complex haemodynamic shear stress regions in vivo. *Cardiovasc. Res.* **99**, 315–327 (2013).

57. Westerterp, M. *et al.* ATP-binding cassette transporters, atherosclerosis, and inflammation. *Circulation Research* **114**, 157–170 (2014).

58. Fang, Y., Shi, C., Manduchi, E., Civelek, M. & Davies, P. F. MicroRNA-10a regulation of proinflammatory phenotype in athero-susceptible endothelium in vivo and in vitro. *Proc. Natl. Acad. Sci. U. S. A.* **107**, 13450–13455 (2010).

59. Moore, K. J. & Tabas, I. Macrophages in the pathogenesis of atherosclerosis. *Cell* **145**, 341–355 (2011).

60. Swirski, F. K. *et al.* Monocyte accumulation in mouse atherogenesis is progressive and proportional to extent of disease. *Proc. Natl. Acad. Sci. U. S. A.* **103**, 10340–10345 (2006).

61. Siess, W. *et al.* Lysophosphatidic acid mediates the rapid activation of platelets and endothelial cells by mildly oxidized low density lipoprotein and accumulates in human atherosclerotic lesions. *Proc. Natl. Acad. Sci. U. S. A.* **96**, 6931–6936 (1999).

62. Finn, A. V., Nakano, M., Narula, J., Kolodgie, F. D. & Virmani, R. Concept of vulnerable/unstable plaque. *Arterioscler. Thromb. Vasc. Biol.* **30**, 1282–1292 (2010).

63. Wu, C. *et al.* Mechanosensitive PPAP2B Regulates Endothelial Responses to Atherorelevant Hemodynamic Forces. *Circ. Res.* **117**, 41–53 (2015).

64. Fang, Y. & Davies, P. F. Site-specific microRNA-92a regulation of Krüppel-like factors 4 and 2 in atherosusceptible endothelium. *Arterioscler. Thromb. Vasc. Biol.* **32**, 979–987 (2012).

65. Wu, W. *et al.* Flow-dependent regulation of krüppel-like factor 2 is mediated by MicroRNA-92a. *Circulation* **124**, 633–641 (2011).

66. De Winther, M. P. J. & Lutgens, E. MiR-92a: At the heart of lipid-driven endothelial dysfunction. *Circulation Research* **114**, 399–401 (2014).

67. Cybulsky, M. I. *et al.* A major role for VCAM-1, but not ICAM-1, in early atherosclerosis. *J. Clin. Invest.* **107**, 1255–1262 (2001).

68. Nakashima, Y., Raines, E. W., Plump, A. S., Breslow, J. L. & Ross, R. Upregulation of VCAM-1 and ICAM-1 at atherosclerosis-prone sites on the endothelium in the apoE-deficient mouse. *Arterioscler. Thromb. Vasc. Biol.* **18**, 842–851 (1998).

69. Ley, K. & Huo, Y. VCAM-1 is critical in atherosclerosis. *J. Clin. Invest.* **107**, 1209–1210 (2001).

70. Nahrendorf, M. *et al.* Noninvasive vascular cell adhesion molecule-1 imaging identifies inflammatory activation of cells in atherosclerosis. *Circulation* **114**, 1504–1511 (2006).

Chapter 2

PEG-polylysine coacervate micelle synthesis and methods of characterization

Chapter Abstract

An accurate understanding of the dynamics of micelle assembly requires robust particle characterization methods to determine size and shape characteristics. This chapter examines the general methods by which I synthesized the polymers and micelles, as well as the light scattering methods by which I characterized polyelectrolyte micelles. A basic theory of small-angle X-ray scattering (SAS) and dynamic light scattering (DLS) are given, followed by general block copolymer and PEC micelle synthesis methods. Then micelle characterization is explained in depth, with focus on the process of interpreting form factors to obtain shape and size of the PEC core and the behavior of the PEG layer from light scattering methods.

2.1 Introduction

For the scope of this chapter I will limit the theory of SAXS to those parts relevant to my data and the fitting process found to best describe the behavior of my own samples. Here, SAXS scattering model interpretation is most simply described in terms of power laws, so form factors are typically evaluated as log-log plots of the scattering intensity $I(q)$ against the scattering vector q,

$$q = \frac{4\pi}{\lambda}\sin(\theta)$$

where 2θ is the scattering angle, and λ the wavelength of the X-ray beam, here approx. 0.9 Å. In dilute solutions, the form factor of the particles themselves dictates the intensity, measuring the degree of contrast at any given length scale. At low q, scattering intensity is constant until q approaches length scales present in the sample, as described by Guinier's law[1]:

$$\ln I(q) = \ln I_0 - (\frac{{R_g}^2}{3})q^2$$

At high q, the examined length scales are so short that the only source of contrast for scattering is the interface between solvent and sample. For a smooth interface, Porod's law applies:

$$I(q) \propto q^{-4}$$

In the case of a smooth sphere, we can see a smooth transition from the Guinier region to the Porod region, at approximately $q = 1/R_g$ (Figure 2.1a). If the sample is monodisperse, one also observes oscillations in the Porod region which arise from Bragg diffraction-like behavior of the diameter of the sphere. We can see this by applying Bragg's law to q to yield

$$q = \frac{n\pi}{R_g}, n = 1,2, \ldots$$

The Schulz sphere model introduces polydispersity on a Schulz distribution as a parameter, which resembles a Gaussian distribution at low polydispersity. Higher polydispersity quickly suppresses these higher-order oscillations, yielding a smooth slope in the Porod region which still varies with q^{-4} (Figure 2.1b,c). If the sample population has anisotropic shape, then the shape information manifests in the intermediate region of the form factor between the Guinier region and the Porod region. Most relevant to the scope of this thesis are rigid rods, flexible or wormlike chains, and fractal aggregates. Figure 2.2 shows the form factors of polydisperse spheres, rigid rods, and wormlike chains[1–4]. The single degree of anisotropy present in the rigid rods yields an intermediate region characterized by a

slope of -1, arising from the elongation in one dimension, which extends from the length scale of the rod length to the length scale of its radius. The flexible chain case, characterized by a relatively flexible length that is punctuated by rigid Kuhn segments, is more complex because any or all of the length,

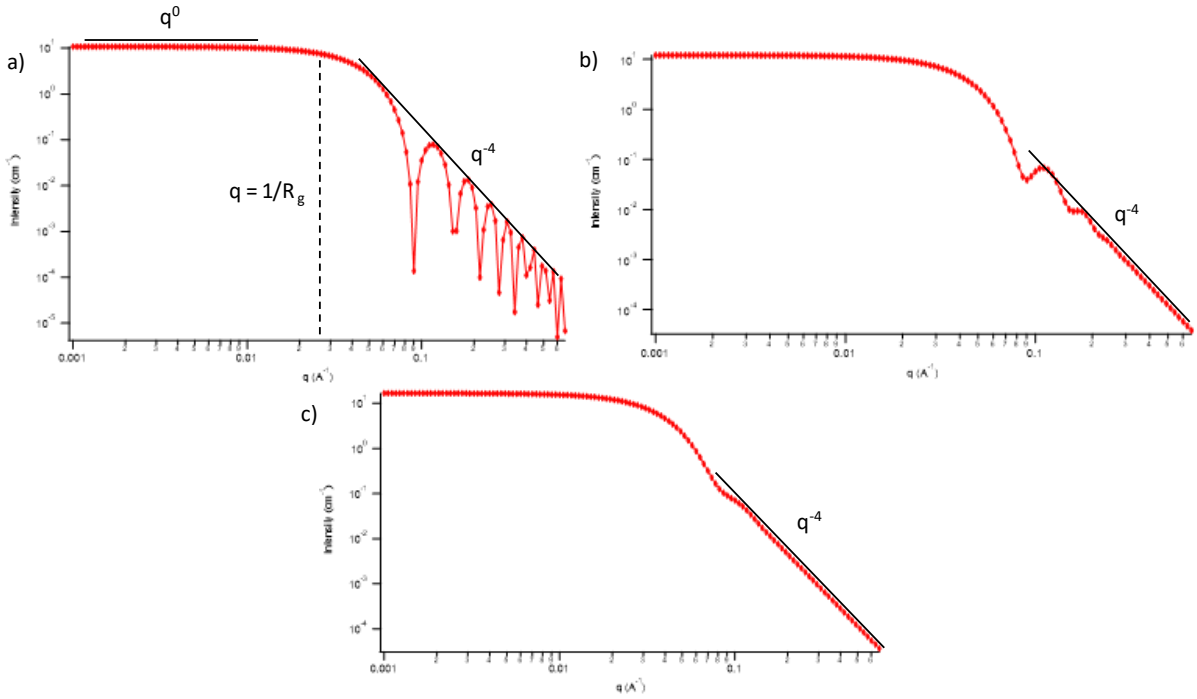

Figure 2.1. Form factors of hypothetical spherical populations, r = 5 nm using a log-log plot of intensity I versus scattering vector q = $\frac{4\pi}{\lambda}\sin\theta$. Spheres produce a form factor characterized by a flat Guinier region, yielding to curvature at q = 1/r, and Porod region slope I ~ q^{-4}. Form factors shown are of model spherical populations that are a) monodisperse, b) PDI = 0.1, and c) PDI = 0.2. Note that higher-order oscillations are present in monodisperse populations, which disappear quickly at relatively low polydispersity, independently of the shape and size characteristics of the form factor. Form factors taken using Irena SAS macros.

persistence length, or radius can manifest, if they are sufficiently distinct. The power law of the form factor from the overall length to the persistence length will fall between q^{-2} for highly flexible chains and q^{-1} for chains where $l \sim l_p$, approximating rigid-rod behavior. However, even in the highly flexible chain case, the q^{-1} behavior of the Kuhn segments can be present, separate from the chain behavior, in a sufficiently long chain (Figure 2.2d).

Fractals are characterized by an aggregation of smaller building block segments into a larger

structure. SAXS scattering of fractal structures captures shape and size information about both the overall fractal structure and the underlying building blocks. In the case of mass fractals, the structure of the aggregate is captured by the fractal dimension D, generally $0 < D < 3$, describing how many dimensions of correlation exist in the structure. At $D = 3$, the correlation extends in every direction, i.e. the fractal structure resembles a 3D object like a sphere. Lower dimensions similarly correspond to a lower-dimensional fractal structure. In SAXS the intensity of scattering from a mass fractal decays

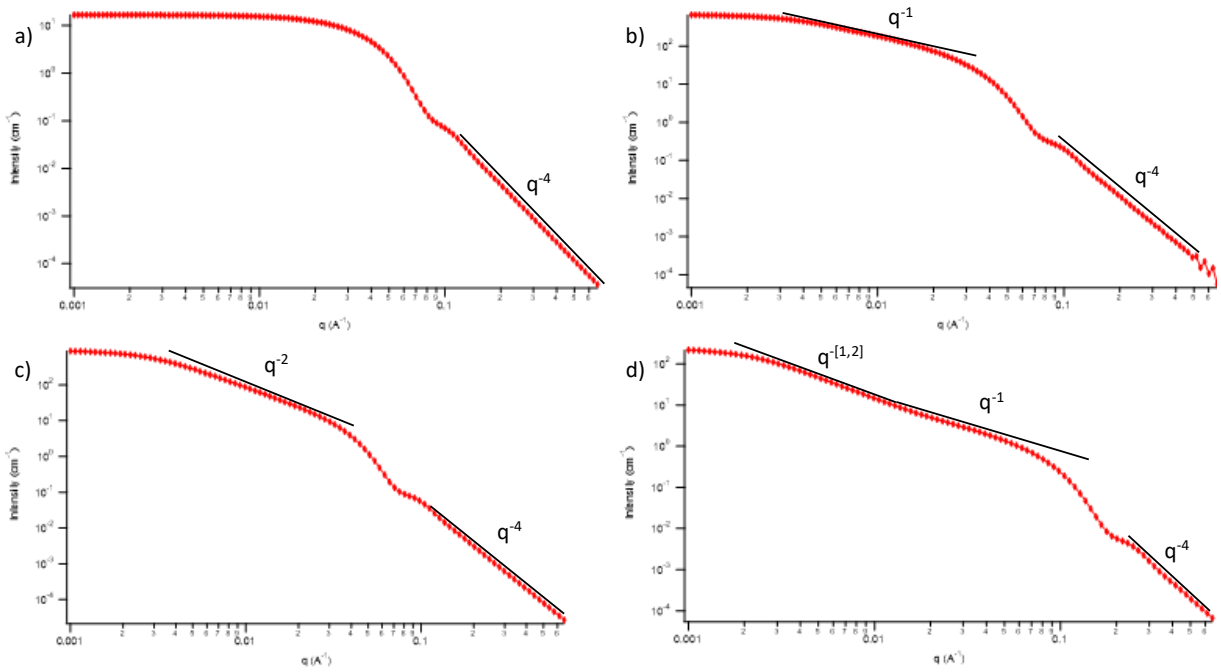

Figure 2.2. Log-log plot of form factors of model a) spheres (r = 5 nm), b) rigid cylinders (l = 100 nm, r = 5 nm), c) flexible chains (l = 500 nm, persistence length l_p = 10 nm, r = 5 nm), with polydisperse radius. While a sphere transitions directly from the Guinier region to the Porod region, rigid cylinders will produce a -1 slope from $q = 1/l$ to $q = 1/r$, at which point the form factor transitions to -4 slope in the Porod region at $q = 1/r$ as in the spherical case. The flexible chain case transitions to -2 slope at $q = 1/l$. d) Flexible chains, l = 800 nm, l_p = 10 nm, r = 2 nm, illustrating the transitions to a slope between -2 and -1 at $q = 1/l$, then -1 at $q = 1/l_p$, and finally to -4 at $q = 1/r$, as expected for a relatively flexible chain composed of inflexible links.

as $I(q) \sim q^{-D}$. The scattering decay transitions to the Porod region at the size scale of the building blocks. Figure 2.3 illustrates these properties of fractal form factors, using a model of spherical

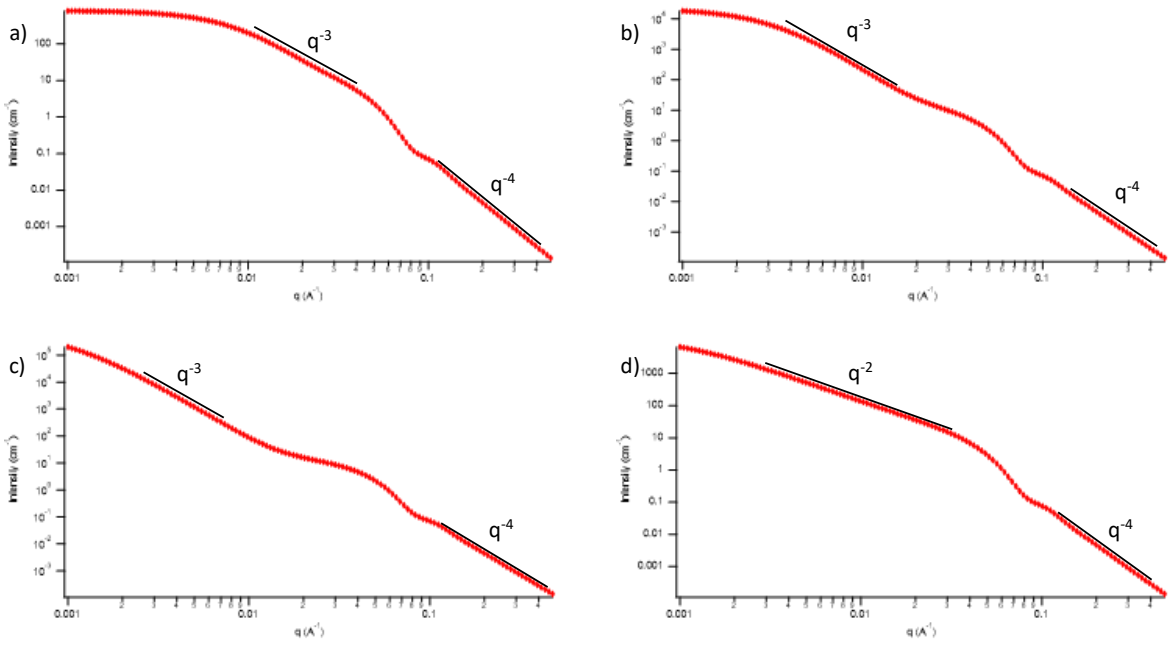

Figure 2.3. Log-log plot of fractal sphere form factors, with block sphere radius 5 nm, p = 0.2, with correlation length, i.e. size of block clusters a) 10 nm (small clusters), b) 30 nm, c) 100 nm (large aggregates of 5-nm radius spheres). Unlike the flexible chain case before, the fractal case resolves to a –D slope in the intermediate region, where 0 < D < 3 is the mass fractal dimension of the aggregates, transitioning from wormlike chains to beads on strings to mass fractal spheres. In these models D = 3, corresponding to mass fractals in the approximate shape of spheres. The radius of the spheres within the aggregate clearly show in the form factor against the aggregate itself. Mind the difference in intensity scales. d) Form factor of a mass fractal sphere model, r = 5 nm, correlation length 100 nm, D = 2, corresponding to a disc. Note the similarity to the form factor of flexible cylinders in Figure 2.

building blocks, with varying degrees of aggregation.

Dynamic light scattering, or DLS, is commonly employed to complement SAXS methods, especially in cases where scattering length density is too near that of the solvent to produce strong scattering. DLS measures diffusion of particles in a solution, and for spherical particles the Stokes-Einstein equation relates diffusion and size, making DLS a useful method for determining the size of particles in solution:

$$R_h = \frac{kT}{6\pi\eta D}$$

where η is the solvent viscosity, and D the diffusion coefficient. R_h is defined as the radius of the smooth sphere that has diffusion coefficient D and is known as the hydrodynamic radius. DLS determines the diffusion coefficient via statistical methods. The statistical algorithms are generally handled within the software for the detector and are briefly summarized here. The diffusion coefficient is found by firing a laser at a dilute solution of interest and measuring the scattering intensity at a specified angle. The intensity is recorded per pixel on the detector as a function of time and will generally have fluctuations as particles begin or stop scattering at random points. For each time t, the software calculates the correlations of each measured intensity at that time and a specified later time $t + \tau$, to obtain a plot of the correlation, $G(\tau)$, vs. τ, called a correlation function. Measurements are typically a few seconds long, as $\tau = 1\mu s$ is typically enough delay to have baseline correlation, and for random motion the correlation function behaves as an exponential:

$$G(\tau) = 1 + A\exp(-2\Gamma\tau)$$

with

$$\Gamma = Dq^2$$

where q is the scattering vector

$$q = \frac{4\pi}{\lambda}\sin\left(\frac{\theta}{2}\right)$$

and D is the diffusion coefficient from above. Note that the definition of θ is the angle between the laser and the detector here, rather than the reflection plane. For a monodisperse population of spheres, finding R_h is a simple matter of fitting the exponential for Γ and solving using the Stokes-Einstein equation. This method is known as the method of cumulants[5]. For solutions with multiple populations, or a polydisperse distribution,

$$G(\tau) = 1 + \int A(\Gamma)\exp(-\Gamma\tau)\,d\Gamma$$

it is tempting to invert to solve for the Γ of the populations, and their respective *D*. However, solving the inverse function is an ill-posed problem and one must take care that any results derived from solving for Γ in this manner have a reasonable physical basis. A generally reasonable assumption is that the number of polydisperse populations is small and thus the correlation function will be smooth. This fitting technique is known as regularization, and multiple algorithms have been developed to carry out fitting the inverse Laplace transform carefully. Our work utilizes the CONTIN algorithm to obtain a regularized fit of our DLS data[6].

2.2 Materials and synthetic methods

2.2.1 Materials

Fmoc-protected amino acids and synthesis-grade solvents were purchased from Gyros Protein Technologies. Fmoc-PEG(2000)-COOH was purchased from JenKem. TentaGel R RAM Rink Amide (0.19mmol eq/g loading) was purchased from Rapp Polymere. HATU, Piperidine (>98%) and N-Methylmorpholine (NMM) were purchased from Millipore-Aldrich. Methoxy-poly(ethylene glycol)-b-poly(L-lysine hydrochloride) (PEG-PLK) was purchased from Alamanda Polymers with the following weights: PEG(5000)-b-PLK10 (5k10), 5k30, 5k50, 10k10, 10k30, 10k50, 10k100. dhRNA, dsRNA, dhDNA, and dsDNA were purchased from IDT as single strands. Hairpin strands were thermally annealed with a starting temperature 20°C above the melting point at 0.5°C/hr to yield double-hairpin nucleic acids. Complementary single strands were mixed and then thermally annealed via the same procedure to yield double-stranded nucleic acids.

2.2.2 Synthesis of VHPKQHR-PEG(2000)-poly(L-lysine)

Polymers were synthesized using solid-phase peptide synthesis on a PS3 synthesizer (Gyros), using DMF as solvent, 400mM N-methylmorpholine as base for activation, HATU as activator, and 20% piperidine in DMF for Fmoc deprotection. Synthesis vessel was prepared using 0.25 mmol equivalent of TentaGel Rink amide resin, which was swelled in DMF for 30 min prior to addition of the first amino acid. Prepared vials of 1mmol Fmoc amino acid or 2kDa PEG plus 0.95 mmol HATU were arranged for machine synthesis in reverse (C-terminus to N-terminus) sequence, starting with the lysine for the polylysine block. Each step of synthesis was carried out thus: 2x 10min deprotection, wash, addition and mixing of activated amino acid, wash. Mixing time of amino acids generally increased with increasing polymer length: 20-40 min for first and last lysine, 8h for Fmoc-PEG-COOH, and 1.5h for each surface peptide amino acid. Polymer was cleaved from resin using 95% v/v trifluoroacetic acid for 2h, then was collected with 20 ml methylene chloride, which was evaporated to approximately 5 ml. Polymer was precipitated with 4 parts -80°C diethyl ether. Crude precipitate was collected, dried, redissolved in water, and lyophilized. Purification was carried out using reverse-phase HPLC, using a C8 column and water/acetonitrile eluent. Pure product was extracted at 10% v/v acetonitrile in water, 0.1% formic acid. Organic portion was evaporated, and remaining aqueous solution was lyophilized to yield 60-80 mg of VCAM-2k30 as a white fluffy powder.

2.2.3 Preparation of polyelectrolyte complex micelles

For mixing methods, a 65 μM solution of nucleic acid was prepared in water or 1x PBS. Peptide-PEG-polylysine (5 mg/ml) was added to a 1:1 charge ratio of polylysine and nucleic acid. Charge ratio was determined by maximal dynamic light scattering signal. Solution was vortex-mixed for 30s, and allowed to sit for 10 min before measurement. For dilution methods, a 260 μM solution of nucleic acid in water or PBS was prepared as in the mixing method. After letting sit, water or PBS

was added to a final nucleic acid concentration of 65 μM, vortexed briefly, and allowed to sit 10 min. For dialysis methods, a 130 μM solution of small hairpin RNA in 1M aqueous NaCl was prepared as in the mixing method, except that after vortexing the solution was placed in a 500 μl dialysis cartridge and dialyzed into water or PBS. After 24h, the water or buffer was exchanged for fresh water or buffer, and the dialysis continued another 24h before measurement.

2.3 Micelle characterization methods

2.3.1 Characterization of Micelle Assembly, Shape, and Size by Small-angle X-ray scattering (SAXS)

This section describes a practical approach to structure determination using SAXS, employing the Advanced Photon Source Beamline 12-ID-B at Argonne National Laboratory. Samples were measured using a flow-cell apparatus to measure scattering intensity of a 150-μl sample in 1% glycerol or 1% glycerol in 1x PBS under continuous laminar flow conditions. Thirty snapshots are taken over 1 minute, analyzed for degradation from the beam, and the undegraded snapshots (typically all of them) are averaged and background solvent subtracted to yield form factors for the particles in Igor, which are then fit to known models using the Irena macros for shape and structure determination[3]. The behavior of the Guinier and intermediate region slopes provides a rich set of structural information about the size and shape of the polymer complexes, and commonly the correct model is identifiable by sight. Having identified a model, the most important parameter to obtain is the radius of the micelle. In the case of the Schulz sphere model, there are only three parameters (scale, radius, polydispersity) so the fitting is straightforward. In the PEC micelles, the most common deviation from the model arises from structural complexity at the scale of the polymers themselves. Figure 2.4a illustrates a typical spherical PEC micelle, assembled from a double-hairpin DNA (dhDNA) mixed

with PEG5k-PLK10 neutral-cationic block copolymer. The resulting form factor is readily modeled as a polydisperse population of spheres from q = 0.06. The data deviates from the model at q ~ 0.075 A^{-1}, to decay as q^{-2}, often seen for wormlike chains, instead of the q^{-4} expected of the surface of a solid sphere. Since the deviation arises in the high-q region, it is arising from behavior within the core structure and must result from the polyelectrolyte complexes themselves. Therefore, the q^{-2} power law indicates that the polymer complexes themselves are acting as Gaussian neutral polymers, which means their polyionic charges must be neutralizing in the core, as expected of PECs mixed with

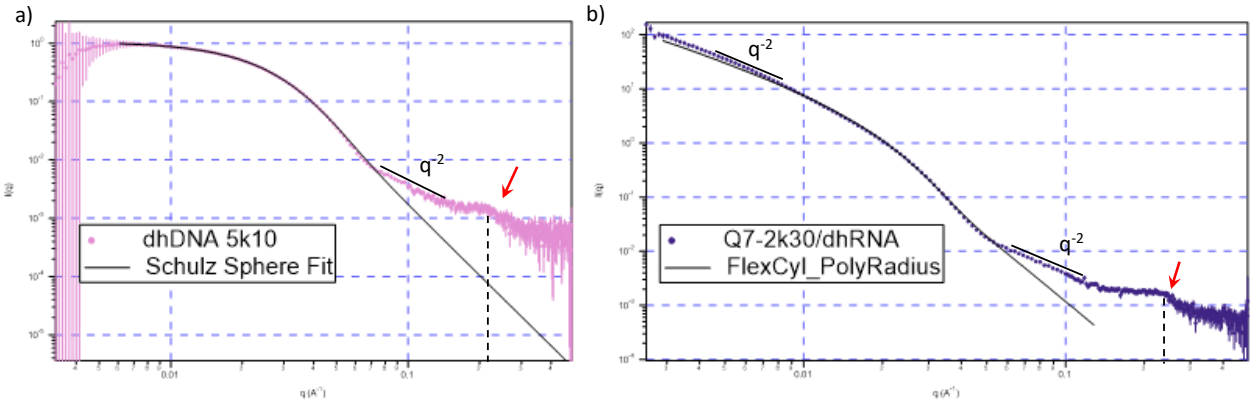

Figure 2.4. a) A sample of nucleic acid/polylysine PEC micelles. In the case of dhDNA and PEG5k-PLK10, the Schulz sphere fit in the low q region indicates that the micelles are spherical and polydisperse, with a core radius of 4.5 nm. The model was fit for 0.006 A^{-1} < q < 0.07 A^{-1}, before fixing the parameters and extending the model to high q to emphasize the difference between the sample and polydisperse ideal spheres. The -2 slope at high q agrees with an internal structural model of Gaussian neutral polymers, which also indicates that the polymer complexes are of overall neutralized charge. The Gaussian neutral polymer-like structure is a common feature of liquid PECs. The peak at q = 0.21 A^{-1} (red arrow) corresponds to a length scale of 3 nm, which is consistent the interhelix spacing resulting from parallel packing of DNA helices (cite Michael and toroid paper). The peak results from parallel packing of the double-stranded portion of the dhDNA, which is short enough to pack with PLK10 in the core (Also cite Michael). b) An example of wormlike nucleic acid/PEG-PLK micelles. QQQQQQQ-2k30 mixed with miR inhibitor (a dhRNA) fits to a flexible cylinder reasonably well, with a 7.3 nm radius and 23 nm Kuhn length. The calculated length is in excess of 1μm, indicating very long micelles. The -2 slope at low q is characteristic of wormlike chains. The fit underestimates the intensity at low q, indicating some degree of aggregation present. Note the -2 slope at high q is also present here, indicating the core behaves like Gaussian neutral polymers as in the spherical case and is likely liquid. Note the broad peak at q = 0.22 A^{-1} (red arrow) indicating that the PEC core exhibits interhelix packing of the RNA in the core of the wormlike micelles.

equimolar charge[7]. In addition, a peak can be observed at q = 0.21 A^{-1}, corresponding to a length scale of 3 nm. Previous work has found this peak to be the interhelix distance of packed DNA in the core of these micelles[8,9]. Interestingly, the double-hairpin nucleic acids are observed to pack within the core of the PLK10-core micelles, while the dsDNA is found to avoid packing within micelles using the same block copolymer, in accordance with previous study[8].

The process for modeling a wormlike micelle is similar. The wormlike model FlexCylinder_PolyRadius adds additional parameters of length and Kuhn length. Usually the optimal approach is to model the radius first, which captures the slope change in the intermediate region, then to fit the Kuhn length and overall length together. For very long worms, the slope of the Guinier region might only approximately fit, in which case re-fitting with the above parameters can help tighten the model. Figure 2.4b shows an oligoglutamine(Q7)-PEG2k-PLK30/dhRNA micelle, which to a first approximation is a wormlike micelle, with 7.3 nm radius and 23 nm Kuhn length. We observe that the model underestimates the low-q intensity of the data, but that the data (but not the model!) follows a clear q^{-2} power law, even when the length parameter is allowed to exceed 1μm. Longer lengths would not make physical sense, given other measurements of this micelle sample, but assuming the model is correct means a possible small population of self-attracted or aggregated "sticky" micelles is present, which would increase the power law. The similar scale of the width of the micelles to the Kuhn length suggests that the worm can be thought of having rigid freely jointed segments that are nearly spheroid.

Fractal micelles require more parameters to model, as the model must account for the building blocks, the aggregate, and the fractal dimension. Figure 2.5 shows an oligolysine (K7)- PEG2k-PLK30, which forms a mass fractal structure. The radius of the building blocks is usually the best place to start modeling, and attempting to model the intermediate region here using Schulz spheres yields 2.4 nm as an approximate starting radius. Fixing the radius at 2.4 nm, we next free the fractal dimension and correlation length parameters, which yields a dimension of 2.97 and a length over 100 nm. Finally, we

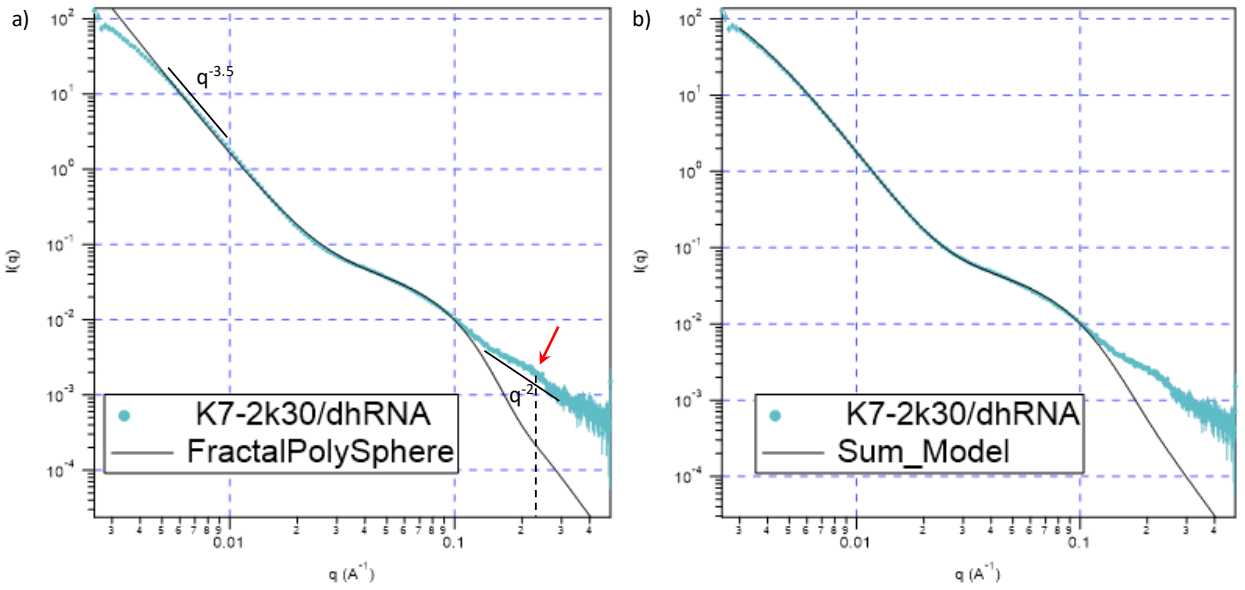

Figure 2.5. Aggregated nucleic acid/PEG-PLK micelles, modeled here as mass fractals. a) KKKKKKK-2k30/miR inhibitor fits a fractal polydisperse sphere model, as a mass fractal with a 2 nm sphere radius and aggregate size > 400 nm. Again we can observe the -2 slope at high q indicating Gaussian chain structure in a liquid core, and the broad peak at q = 0.22 A^{-1} (red arrow) indicating that the PEC core exhibits some interhelix packing of the RNA in the core. The low q behavior is not as well modeled, because the model assumes an infinitely large aggregate. At sufficiently large length scale, the scattering behavior becomes indistinguishable from that of smooth masses, and scatters with a lower power law. b) 10:1 volume fraction of Schulz spheres:fractal spheres. Sum model corrects fractal sphere radius to 1.6 nm, indicating that droplets in the core are very small and prone to aggregation. Aggregates found to have approx. 38 nm correlation length.

free the parameters and let the fit optimize, which yielded Figure 5a. The calculated sphere radius is 2 nm, and the aggregates are calculated to be slightly over 40 nm, with a fractal dimension of 2.99. The model overshoots the intensity at low q, and has a $q^{-3.5}$ power law. The power law is interesting, given the fractal dimension, but the low q behavior is best explained by the finite size of the aggregates. The model assumes an infinitely large fractal, but smaller fractals will behave like similarly shaped smooth masses at low q. The K7-2k30 data can be fit to assume a subset of nonaggregated particles. The sum model in Irena combines two models by combining their respective parameters. With so many parameters, care must be taken not to overfit. In this case, I assumed that the aggregates were composed of spherical subunits along with free spheres of approximately the same size as the fractal

subunits, and began with the fractal parameters fixed to the values that yielded Figure 2.5a. Fixing the spherical components of the model to equal the building blocks in the fractal component, and fitting for relative scale, the model yielded an improved fit, which was allowed to adjust the radius and correlation parameters to yield Figure 2.5b. The calculated radius of the spheres was found to be 1.6 nm, with about 10% of the scattering intensity coming from the aggregates, which themselves had a correlation length of 38 nm in this sample. The 1.6 nm spheres are approximately 0.9 nm wider than the width of dsRNA, likely individual RNA complexes. Taken together, the data suggest that these complexes are aggregating in such a way that the complexes are remaining separated, for the most part, but with some aggregation present.

2.3.2 Characterization of micelle size and aggregation by dynamic light scattering (DLS)

Dynamic light scattering complements SAXS by providing information about the diffusion of the micelles, which in turn provides information about the overall size of the micelles. Because SAXS measurement mainly captures the characteristics of the core, DLS can be used to complement SAXS, providing information about the neutral corona. One must take care interpreting results, especially in nonspherical cases because the calculated diffusion rate itself assumes that the population causing the scattering is generally spherical. If we know the shape of the particles *a priori*, we can interpret the hydrodynamic radius properly by, for example, calculating a radius of gyration R_g and comparing to the R_g of the core found in SAXS to determine the thickness of the PEG layer. Figure 2.6 shows the autocorrelation curve and size distribution calculated by the CONTIN algorithm of K7-2k30 and Q7-2k30 dhRNA micelles. By fitting the autocorrelations to an exponential curve, we get a hydrodynamic radius of 40 nm for the K7 case and 47 nm for the Q7 case. Because of the SAXS measurements shown earlier, we know that these radii do not correspond to real spherical particles in our population.

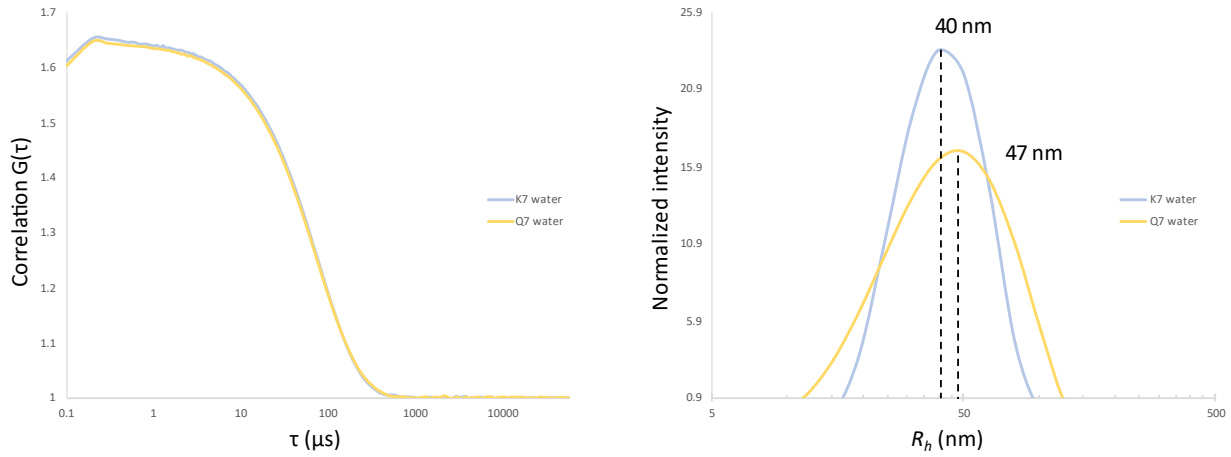

Figure 2.6 a) autocorrelation and b) calculated size distribution of K7-2k30 and Q7-2k30 dhRNA micelles. Taken with the SAXS data above, the K7 aggregates have a core radius of 30-36 nm, which leaves 4-10 nm as the thickness of the PEG layer, suggesting a crew-cut micelle. In the Q7 wormlike micelle case, we can find the length of the worms using known parameters for flexible chains to identify worms to have a length of 1.3 μm.

However, we do know the structures of the polymer complexes: the K7 is a mass fractal with $d = 2.99$, while the Q7 is wormlike. In a mass fractal with $d = 3$, the hydrodynamic radius is predicted to be approximately the same as the correlation length, or slightly smaller, about 36 nm in the K7 case[10]. This suggests that the PEG corona of the aggregates is approximately 4 nm thick, and that the resulting micelles are crew-cut. This is in agreement with the properties of PEG[11]. Assuming the aggregates to be approximately spherical, and the PEG of internal building block spheres to be of near-identical thickness, the size of the aggregates suggests an approximate aggregation number of 200 RNA molecules. As for the Q7 case, $R_g/R_h = 8/(3\sqrt{\pi})$ and $R_g = b\sqrt{N/6}$ for a wormlike chain[12]. Given $R_h = 47$ nm, we find $R_g = 70.7$ nm, and given $b = 23$ nm from SAXS above, we get $N = 57$, or a contour length of 1.3 μm, which agrees with the approximation found in SAXS. The thickness of the PEG layer mainly affects the radius of the worms, which has minimal effect on these calculations. Thus, taken together, the SAXS and DLS measurements are complementary, and provide a more complete picture of the assembly dynamics than when considered separately.

Chapter Bibliography

1. Guinier, A., Fournet, G. & Walker, C. B. *Small-Angle Scattering of X-Rays*. (John Wiley & Sons, Ltd, 1955).

2. Pedersen, J. S. Structure factors effects in small-angle scattering from block copolymer micelles and star polymers. *J. Chem. Phys.* **114**, 2839–2846 (2001).

3. Ilavsky, J. & Jemian, P. R. Irena: Tool suite for modeling and analysis of small-angle scattering. *J. Appl. Crystallogr.* **42**, 347–353 (2009).

4. Kline, S. R. Reduction and analysis of SANS and USANS data using IGOR Pro. *J. Appl. Crystallogr.* **39**, 895–900 (2006).

5. Koppel, D. E. Analysis of macromolecular polydispersity in intensity correlation spectroscopy: The method of cumulants. *J. Chem. Phys.* **57**, 4814–4820 (1972).

6. Provencher, S. W. A Constrained Regularization Method for Inverting Data Represented by Linear Algebraic or Integral Equations. *Comput. Phys. Commun.* 213–227 (1982).

7. Spruijt, E. *et al.* Structure and dynamics of polyelectrolyte complex coacervates studied by scattering of neutrons, X-rays, and light. *Macromolecules* **46**, 4596–4605 (2013).

8. Lueckheide, M., Vieregg, J. R., Bologna, A. J., Leon, L. & Tirrell, M. V. Structure−Property Relationships of Oligonucleotide Polyelectrolyte Complex Micelles. *Nano Lett.* **18**, 7111–7117 (2018).

9. Maniatis, T., Venable, J. H. & Lerman, L. S. The structure of ψ DNA. *J. Mol. Biol.* **84**, 37–64 (1974).

10. Saarloos, W. Van. On the Hydrodynamic Radius of Fractal Aggregates. *Phys. A Stat. Mech. its Appl.* **147**, 280–296 (1987).

11. Zhengyu, M. *et al.* Tcr triggering by pMHC ligands tethered on surfaces via poly(ethylene glycol) depends on polymer length. *PLoS One* **9**, 112292 (2014).

12. Haydukivska, K., Blavatska, V. & Paturej, J. Universal size ratios of Gaussian polymers with complex architecture: radius of gyration vs hydrodynamic radius. **10**, 14127 (2020).

Chapter 3

Structural Properties of PEG-polylysine coacervate micelles

Chapter Abstract

Mixing of PEG-PLK and RNA forms micelles that protect the RNA in the core and permit functionality at the surface. To evaluate the best applications and design principles for our micelles, it is important to understand the shape and size of the particles we are making. Analysis of micelles mixed under a variety of conditions shows how the composition of the nucleic acid and block copolymer, as well as the salt concentration, can affect micelle assembly. In this chapter I employ light scattering methods such as DLS and SAXS to elucidate the structure these micelles. I furthermore compare assembly of different polymers and nucleic acids, the effects of salinity on assembly, and the effects of different methods of preparation. I demonstrate the properties of double-hairpin RNA-core micelle assembly under various conditions, extending previous work showing the properties of single-stranded and double-stranded RNA-core micelle assembly to a biological RNA that is a hybrid of single- and double-stranded components. My work definitively shows the tendency of PLK/RNA complex-coacervate-core micelles to form wormlike structures in saline solution, and that the wormlike shape is the equilibrium shape of the micelles.

3.1 Introduction

This chapter aims to discuss the properties of micelle formation conditions, as driven by

coacervation or precipitation of polyions. When polymers of opposite charges are mixed in aqueous solution, phase separation can occur, creating a polymer-rich phase and polymer-poor phase in a phenomenon known as coacervation[1]. Coacervation of polyions occurs because of a favorable increase of entropy upon release of small associated counterions when mixing[2–4]. Voorn and Overbeek developed the first theory of the behavior of coacervates as controlled by both the electrostatic interactions of the polyions and the entropic gain of mixing the polyions. The theory is limited, as it assumes no solvent interactions, ideal molecules with no volume nor chain constraints, and a critical mass and charge density of the polyions[5]. The theory also failed to describe coacervation behavior at low salt concentrations, for example if the polyions were mixed in pure water, as unfavorable when experiments had shown otherwise. To address the lower salt discrepancy, Veis and Aranyi developed a model that included the solvent interactions, and found that the entropic contribution was larger than originally posited[6]. Since then, multiple models have been developed to address the effects of the ion pairing and polymer structure, even going so far as to ascribe the complexation entirely to entropic gain without significant electrostatic contribution[3,7,8]. Nucleic acids have been reported to exhibit coacervation behavior consistent with their structure as polyanions, although dsDNA forms solids preferentially[8–11]. Mascotti and Lohman showed that the degree of DNA complexation to oligolysine depended upon both the length of the oligolysine and the concentration of monovalent salt. Complexation occurs less extensively at higher salt concentration, while longer lengths of oligolysine would increase complexation. Dissociation occurred at 1M salt in all cases, and the extent of complexation was found to be predictable by Poisson-Boltzmann models[12].

When one of the polyions is covalently attached to a neutral hydrophilic polymer, then when the polyions are mixed, the neutral polymer can solubilize the complex to form micelles with the complex in the core and the neutral polymer forming a shell, stabilizing the complex in aqueous

solution. Because micelles only form when the chemical potential of a number of aggregated monomers exceeds the potential of the monomers when separate, the aggregation must be favored upon mixing of the polyions[13,14]. It stands to reason that the favorable mixing conditions of the complex in the core drives the micellization. Many of the principles of complex coacervate formation appear to carry over to complex coacervate micelles readily. Kim et al. show that in the case of poly(ethylene glycol)-*b*-polylysine (PEG-PLK) complexed with plasmid DNA, the micelles form due to a large increase in entropy, which they attribute to the release of small counterions[15]. In other words, the neutral block does not affect the polyion block's ability to form complexes. Whether the neutral block has any or no influence on core behavior, however, is an open question.

We chose the complex coacervate micelle approach because RNA delivery is a therapeutic approach with high potential but many challenges related to the stability and activity of RNA within biological systems[16]. To deliver RNA is to fight against an evolutionary history nearly as old as life itself. RNA is an unstable molecule and easily degraded by nuclease enzymes. It is large, polar, and anionic, all of which block its entry into cells. Many viral nucleic loads are RNA based, prompting immune responses to foreign RNA. Therefore, a delivery system that can keep the RNA molecule stable while also protecting it from nuclease enzymes is necessary for a successful RNA therapy. Furthermore, that delivery system must provide the RNA some ability to enter the cell, whether by penetration or by endosomal escape[17–20]. The polyelectrolyte complex strategy has been employed successfully to encapsulate and deliver DNA, and Ponnuswamy has shown that the complexes are capable of protecting the DNA from degradation and aiding endosomal escape[15,21,22]. Our group began to study PEG-b-polylysine coacervate micelles because the system offers a solution to the RNA delivery challenges: the polylysine stabilizes the RNA; it double-shields the RNA from nuclease, both by removing the RNA from the aqueous phase and by surrounding the complex with an inert PEG layer; the PEG layer also prevents unfavorable immune reactions; and the outer peptide

targets the micelle to the target tissue specifically for cell uptake[23]. The delivery system raises its own set of questions and challenges: Does the micelle go where we intend it to? How much RNA do we deliver to the target? How much is trapped in the liver, kidneys, and spleen? What effect does the shape or size of the micelle have on these dynamics?[24–26] While many of these questions have been answered for the dynamics of longer nucleic acids, they remain open in the case of oligonucleotides[21,27–29]. Research of RNA delivery, especially, has shown inconsistent results[30–32]. Furthermore, the study of the structure-assembly dynamics of double-hairpin RNA (dhRNA) in a complex coacervate core micelle is novel. Our group's original preparation of VHPKQHR-PEG-PLK micelles for *in vitro* study[33] showed the conformation of the VHPKQHR (VCAM1-targeting) peptide and the charge of the micelles, but its shape had not been studied. Interestingly, PBS preparations failed to yield consistent micelle formation by dynamic light scattering, so I began to study the conditions that drive micelle assembly using other scattering methods. By preparing micelles using different structures of RNA or DNA, sizes of PEG-PLK copolymers, control of assembly in water or saline conditions, and different peptides presenting on the surface of the micelle assembly analogous to the VCAM-1 targeting sequence, we have sought a better understanding of the dynamics of PEC micelle self-assembly. To examine the structure-assembly relationship of our PEC micelles, we use a variety of light scattering techniques. Dynamic light scattering (DLS) is a statistical light-scattering method that can count and correlate the scattering of particles in solution, which can be reconstructed into information about the diffusion rates of those particles, and therefore the hydrodynamic radius of the particles. It is best suited for spheroidal particles of a relatively narrow size distribution. For anisotropic particles, small-angle X-ray scattering (SAXS) is more powerful, as it is capable of elucidating shape along with size information. Finally, transmission electron microscopy can allow direct visualization of micelles in solution and complements the statistical scattering methods well, if the micelles provide sufficient contrast.

3.2 Materials and Methods

3.2.1 Materials

Fmoc-protected amino acids and synthesis-grade solvents were purchased from Gyros Protein Technologies. Fmoc-PEG(2000)-COOH was purchased from JenKem. TentaGel R RAM Rink Amide (0.19mmol eq/g loading) was purchased from Rapp Polymere. Trifluoroacetic acid (TFA), triisopropylsilane (TIS), HATU, Piperidine (>98%) and N-Methylmorpholine (NMM) were purchased from Millipore-Aldrich. 2000 MWCO and 3500 MWCO dialysis cartridges were obtained from Thermo Fisher. PEG-b-PLK 5k10, 5k30, 5k50, 10k10, 10k30, 10k50, 10k100 were purchased from Alamanda Polymers. dhRNA, dsRNA, dhDNA, and dsDNA were purchased from IDT as single strands. Hairpin strands were thermally annealed with a starting temperature 20°C above the melting point at 0.5°C/hr to yield double-hairpin nucleic acids. Complementary single strands were mixed and then thermally annealed via the same procedure to yield double-stranded nucleic acids. Polymers were synthesized using solid-phase peptide synthesis, with DMF as solvent, 0.4M NMM in DMF as base, HATU as activator, and 20% piperidine in DMF as deprotecting agent. For each step a vial containing 4 equivalents of Fmoc amino acid and 3.9 equivalents of HATU was prepared. Rink Amide and Fmoc-lysine were used on a PS3 synthesizer (Gyros) to synthesize a desired length of polylysine (12, 15, or 30), with 20 mins reaction time per amino acid. 2 equivalents Fmoc-PEG with 1.9 equivalents HATU was then added by SPPS and allowed to react for 8h. Finally the appropriate peptide sequence was synthesized, 1h per amino acid: KKKKKKK (K7), QQQQQQQ (Q7), KKQQQQQ (K2Q5), QQQKQQK (mimic), VHPKQHR (VCAM). After each addition step was a 2 x 10 min deprotection. Each step was followed with a DMF rinse to remove any unreacted agents. Beads were collected, rinsed with methanol to deswell, and dried before cleavage. Cleavage was carried out using 96% TFA, 3%

water, 1%TIS, with gentle shaking for 2h. Samples were collected using DCM, allowed to evaporate to 5 mL, at which point product was collected by precipitation with 20 mL -80°C diethyl ether. Sample was dried completely, redissolved in MilliQ 18MΩ water, and dialyzed 1 day at 3500 MWCO to remove any impurities. After dialysis, the sample was lyophilized to yield a fluffy white powder, which was stored at -20°C for stock use.

3.2.2 Synthesis of polyelectrolyte complex micelles

For mixing methods, a 65 μM solution of nucleic acid was prepared in water or 1x PBS. Peptide-PEG-polylysine (5 mg/ml) was added to a 1:1 charge ratio of polylysine and nucleic acid. Charge ratio was determined by maximal dynamic light scattering signal. Solution was vortex-mixed for 30s, and allowed to sit for 10 min before measurement. For dilution methods, a 260 μM solution of nucleic acid in water or PBS was prepared as in the mixing method. After letting sit, water or PBS was added to a final nucleic acid concentration of 65 μM, vortexed briefly, and allowed to sit 10 min. For dialysis methods, a 130 μ M solution of small hairpin RNA in 1M aqueous NaCl was prepared as in the mixing method, except that after vortexing the solution was placed in a 500 μl dialysis cartridge and dialyzed into water or PBS. After 24h, the water or buffer was exchanged for fresh water or buffer, and the dialysis continued another 24h before measurement.

3.2.3 Light and Scattering Characterization Methods

Dynamic light scattering (DLS) was carried out using 50 μl samples in a Mobius-zeta dynamic scattering apparatus. Samples were measured for five seconds five times and averaged. Regularization fits were carried out by CONTIN Laplace-inversion algorithm[34]. Small-angle X-ray scattering (SAXS) was carried out at Argonne Advanced Photon Source, Beamline 12-ID-B. SAXS samples were measured using a flow cell apparatus to obtain 30 structure factors which were averaged. Models were calculated using either Irena or SANS analysis packages[35,36]. Images of micelles were obtained

using a FEI Talos 200kV cryogenic transmission electron microscope (Cryo-TEM).

3.3 Results

3.3.1 Micelle Assembly Behavior Based on Nucleic Acid Composition

SAXS data signal was greater in both DNA series compared to RNA. SAXS form factors of PEG5k-PLK30 (5k30) block copolymers assembled with variable nucleic acids illustrate many of the trends of nucleic acid composition (Figure 3.1) DNA assemblies had larger radius compared to RNA. dsDNA and dsRNA assembled into wormlike micelles as evidenced by the low-q region of the SAXS form factors, while dhDNA and dhRNA mainly assembled into spheroid micelles. The double-stranded nucleic acid PEC structures also showed high-q behavior of a q^{-1} power law, suggesting that their cores are behaving like rigid cylinders, while the double-hairpin DNA showed q^{-2} at high q, suggesting a liquid-core Gaussian chain behavior in the core. There was little correlation between backbone sugar and shape. There was not a clear size correlation resulting from the secondary structure of the nucleic acid. However, the dsDNA showed more wormlike character compared to the dsRNA, while the dhDNA showed more spherical character compared to the dhRNA. Similarly, the dependence of micelle shape on DNA structure can be seen with other PEG-PLK copolymers. Figure 3.2 shows form factors of micelles constructed with PEG5k-PLK10 (5k10), along with calculated fits from the Irena macro. dsDNA-core micelles appear to be best modelled as cylinders with polydisperse radius, while dhDNA-core micelles are best modelled with the Schulz Spheres fit. Note this is the same as the 5k30 case above. While the dsDNA5k10 micelles are showing nearly rigid-rod behavior in SAXS, the Irena fit shows that the low-q power law is between 0 and 1, indicating a structure that is more rodlike than spheroid but somewhere in between the two. The dsDNA appears to prefer assembling into somewhat anisotropic micelles while the dhDNA assembles into spherical micelles. The calculated radius is nearly

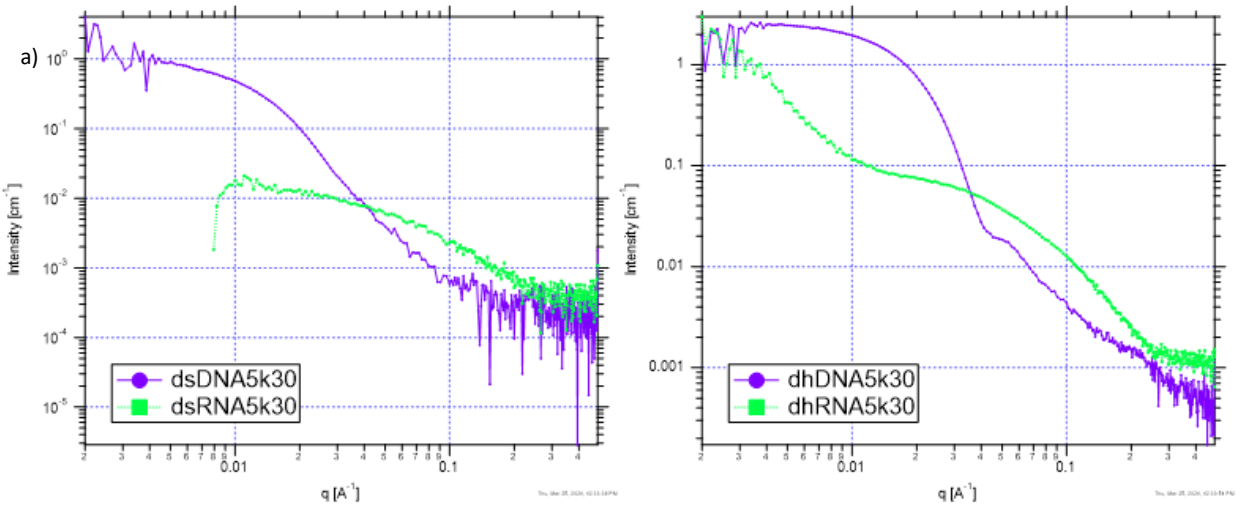

b)

	slope	R_g (nm)
dsDNA	-0.9	13.1
dsRNA	*	3.41
dhDNA	-0.4	9.74
dhRNA	0	2.71

c)

	fit	Radius (nm)
dsDNA	cyl	7.8
dsRNA	cyl	1*
dhDNA	sch	9.5
dhRNA	*	0.5*

Figure 3.1. a) SAXS graphs of dsNA- and dhNA-core 5k30 assembled micelles. DNA (purple) yields larger structures compared to RNA (green), and the double-stranded cases (left) and dhRNA (right) exhibit rigid-rod behavior in the core while the dhDNA (right) exhibits Gaussian chain behavior. Note the slight peak at q = 0.21 in the dhDNA form factor, indicating packing of the DNA in the core. b) table of Guinier fits. A slope between 0 and -1 in the DNA 5k30 samples suggests a predominantly spheroid assembly, with the dhDNA-core micelles exhibiting a more spheroid character than the dsDNA-core micelles. While the form factor of the dsRNA 5k30 samples indicates the presence of a ~3nm-radius structure in the ensemble, the lower signal makes shape determination difficult, with a likely predominance of unassembled RNA. c) table of Irena fits to the form factors. The dsDNA 5k30 fits to cylinder-polyradius fit, with a radius of 7.8 nm, while dhDNA fits to a Schulz spheres fit, with a radius of 9.5 nm. Cyl = Cyl_PolyRadius fit, sch = SchulzSpheres fit. The more spheroidal form factor of the dhDNA 5k30 can be explained by the partially single-stranded structure of the dhDNA. The RNAs do not fit as cleanly and yield physically questionable parameters, and while the dhRNA-core structure seems to follow a 3-dimensional fractal curve with a 1 nm block radius (individual PECs), the fit is poor and suggests a 1-meter correlation length, which is clearly nonphysical.

identical in both cases, further demonstrating that micelle size is not correlated to the structure of the DNA. The cores of both micelle populations exhibit Gaussian chain behavior, and the dhDNA5k10 micelles shows a DNA helical packing peak at q = 0.2. While the 5k10 and 5k30 polymers show clear trends from the dsDNA to dhDNA, other polymers complicate this trend. Similar measurements of

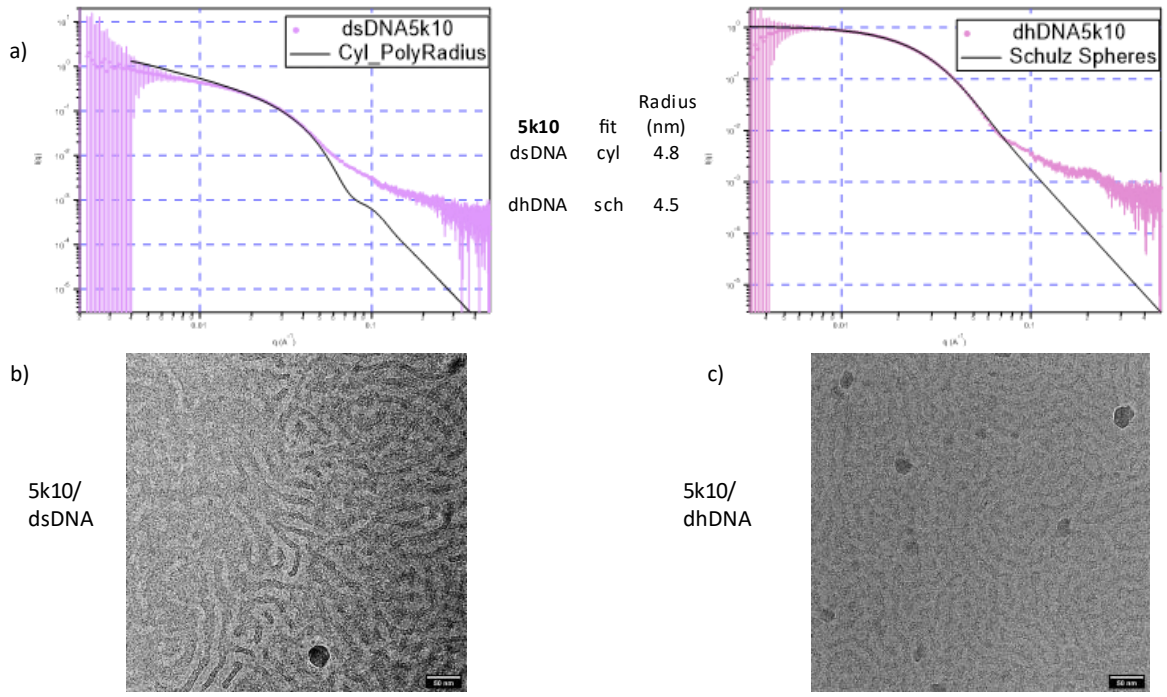

Figure 3.2. a) SAXS form factors of dsDNA 5k10 and dhDNA 5k10 micelles, with fits and calculated radii shown. Both samples have similar radius, but dsDNA has some wormlike character, while dhDNA is more spheroidal. Note that the radii are smaller than in the 5k30 cases. b) TEM image of dsDNA 5k10. The image shows a network of wormlike structures which corresponds in width to the radius found in SAXS. c) TEM of dhDNA 5k10, illustrating my choice to focus primarily on SAXS for structure analysis. The dhDNA shows some structures, but it is unclear whether they are micelles or ethane out of the focal plane. Furthermore, it is possible to see poorly contrasted wormlike structure similar to the dsDNA case, which agrees with the radius found by SAXS and may be micelles, but may also be a side-effect of an overconcentrated sample. Other samples yield similar images (not shown), and the literature corroborates my own observations[van der Kooij Langmuir 2012], so I have relied on the SAXS form factors for my analysis.

dsDNA or dhDNA-core micelles assembled from PEG5k-PLK50 (5k50), PEG10k-PLK30 (10k30), and PEG10k-PLK50 (10k50) reveal wormlike assembly regardless of DNA structure, suggesting that the assembly of dhDNA is more complicated and may show some dependence on the structure of the copolymer (Figure 3.3). The 5kPEG dhDNA-core micelles also show a peak at q = 0.2 $Å^{-1}$, which corresponds to the packing width of double-stranded DNA, although the peak is somewhat broad and the data is noisier at high q. This peak indicates that the dhDNA is capable of some degree of DNA

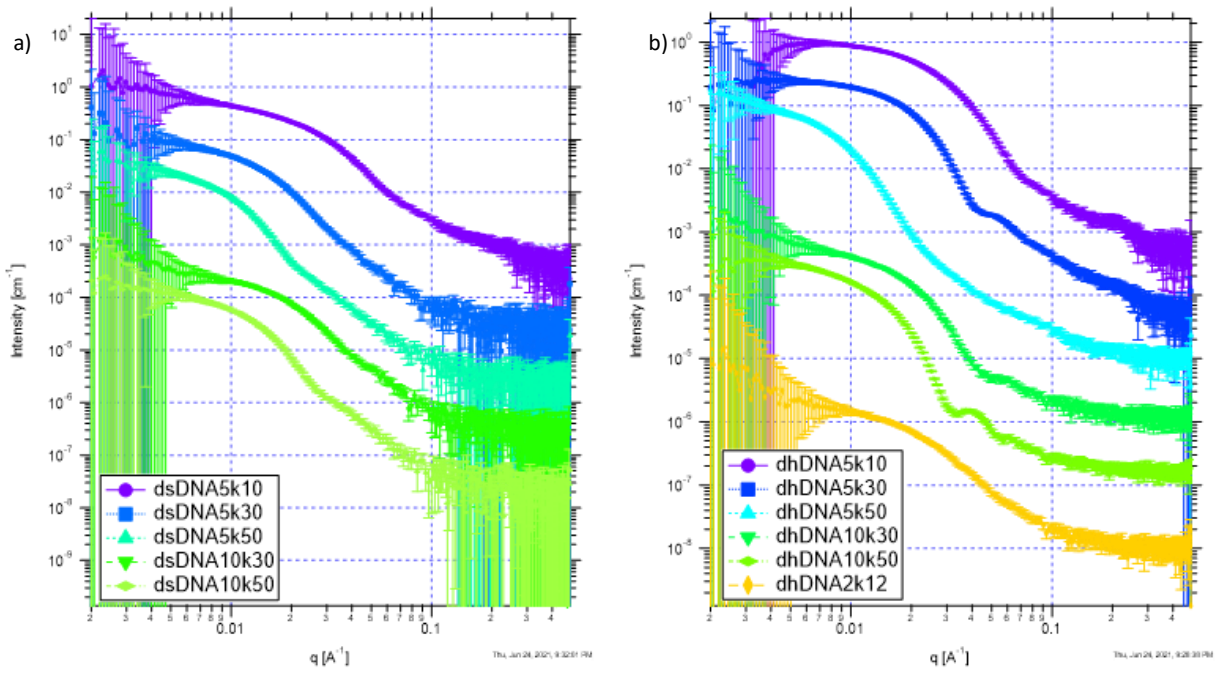

Figure 3.3 SAXS of PEC micelles by nucleic acid in the core. a) dsDNA assembles consistently into rodlike structures. The SAXS curves consistently show negative slope at low q, indicative of rodlike assembly, while at q ~ 0.03-0.1 Å^{-1}, the power law resolves to q^{-3}, indicating a mass fractal structure at the 5-30 nm length scale, before resolving to q^{-1} at high q. The behavior of the form factor strongly suggests a trend cores shaped like rods over 100 nm long, with 10-15 nm radius, and fractal structure within the core suggests that the core itself is composed of rigid PEC precipitates that have gaps within. The dsDNA 5k10, notably, has a liquid core and no fractal behavior. b) dhDNA assembles into wormlike (5k50, 10k30, 10k50) or spherical (5k10, 5k30) micelles. The dependence of dhDNA-core micelle shape on polymer size suggests that the dhDNA is near a critical threshold of spherical vs rodlike assembly. It is not immediately clear why the 10k50 case is more spheroidal compared to 10k30 while 5k50 is more rodlike compared to 5k10 and 5k30, but the trend towards more wormlike character with the dsDNA is clear. The micelles have a liquid core, but the 5kPEG micelles, with a power law of q^{-2}, have a flexible core, while the 10k micelles, with $q^{-5/3}$ power law, have a semi-rigid core composed of self-repelling complexes.

packing in the core of the micelles. Additionally, there is a clear contrast in the core behavior of the micelles as indicated by their slope at high-q. The dsDNA samples have a transition from q^{-1} to q^{-3} at some point between q = 0.02 Å^{-1} and q = 0.04 Å^{-1}, indicating a transition to mass fractals at the length scale of the diameter of the rods. The power law transitions again at q = 0.1 Å^{-1}, or about 5 nm, to q^{-1}, indicating rodlike structure at this scale. The behavior is indicative of rigid polymer complexes, which

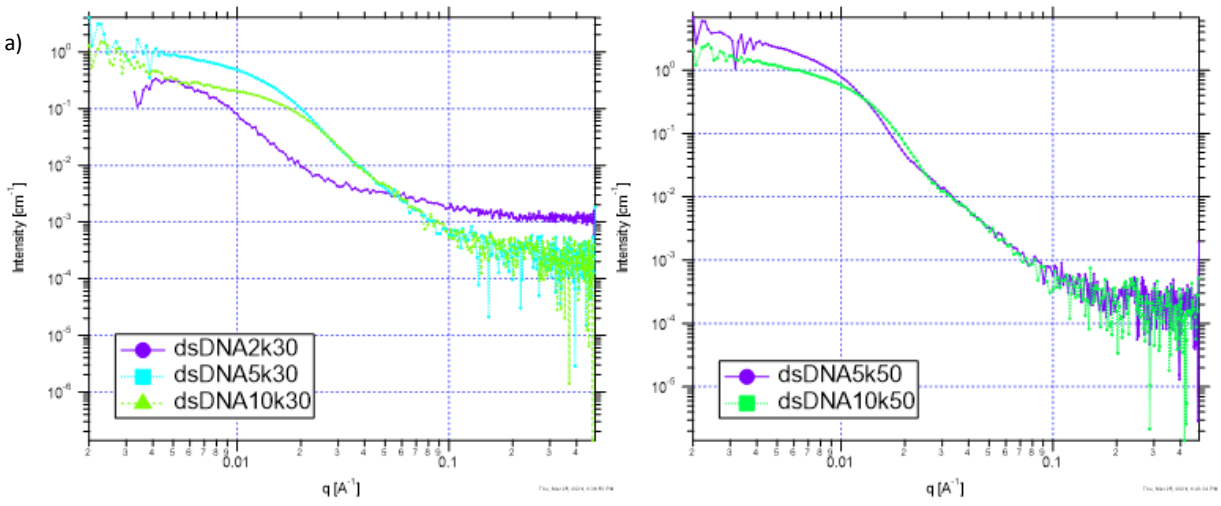

b)

dsDNA-K30 2kPEG	slope	Rg	dsDNA-K50 2kPEG	slope	Rg
5k	-0.9	13.1	5k	-1	19.8
10k	-0.7	9.97	10k	-0.9	15.1

c)

dsDNA-K30 2kPEG	fit *	Radius (nm) *	dsDNA-K50 2kPEG	fit	Radius (nm)
5k	cyl	4.8	5k	cyl	6.6
10k	cyl	3.5	10k	cyl	7.7

Figure 3.4. a) SAXS of variable PEG length of K30 (left) and K50(right) dsDNA micelles. b) tables of Guinier-Porod and c) model form factor fits of dsDNA K30 and K50 samples with variable PEG length. The PEG length has minimal effect on the size and shape of the resulting micelles.

strongly suggests that these are precipitate-core micelles. The dhDNA micelles transition to q^{-2}, indicating that the cores are composed of flexible neutral chains and are likely liquid.

3.3.2 Micelle Assembly Behavior Based on Block Copolymer Size

From SAXS of the dsDNA-core micelles (Figure 3.4), an increase in PEG length from 2kDa to 10kDa showed a slight decrease in radius in the PLK30 series, but a small increase in the PLK50 series. The dhDNA also showed minimal size dependence on the PEG block length. There was also little correlation between PEG length and resulting shape of assembly in the dsDNA-core micelles. In contrast to the PEG, the length of the PLK block showed clear correlation in the dsDNA-core micelles (Figure 3.5). In nearly every case, an increase of polylysine length resulted in a larger micelle radius. In the dsDNA case, the micelles were wormlike independent of the length of the PLK block. In the dhDNA-core 5kPEG micelles, longer polylysine also correlated with longer size. Furthermore, a longer

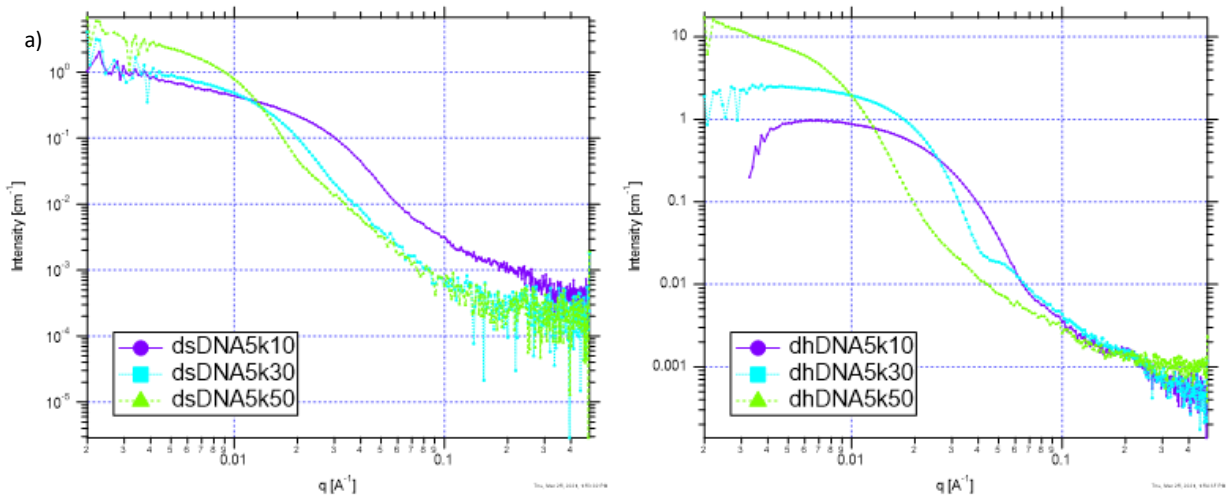

b)

dsDNA-PEG5k	slope	Rg	dhDNA-PEG5k	slope	Rg
PLK10	-0.8	7.46	PLK10	0	6.87
K30	-0.9	13.1	K30	0	9.74
K50	-1	19.8	K50	-1	22.6

c)

dsDNA-PEG5k	fit	Radius(nm)	dhDNA-PEG5k	fit	Radius(nm)
PLK10	cyl	3.9	PLK10	sch	4.5
K30	cyl	8.2	K30	Sch	9.5
K50	cyl	12.2	K50	cyl	15.8

Figure 3.5. a) SAXS of variable polylysine length of PEG5k micelles made with dsDNA (left) and dhDNA (right). b) tables of Guinier-Porod and c) form factor fits of dsDNA and dhDNA 5kPEG with variable polylysine length, showing that micelle size increases with polylysine length. This trend holds for both shapes of DNA in the core. Interestingly, the dhDNA 5k micelles seem to be spherical at lower polylysine length, while the dsDNA 5k micelles are wormlike at all the measured polylysine lengths.

PLK block correlated with more wormlike assembly in dhDNA-core micelles. 5k10 and 5k30 dhDNA-core micelles were smaller and had form factors that correspond to spherical assembly. 5k50 micelles were larger and assembled into worms. The 10kPEG micelles complicate the shape trend as noted above, but agree with the size trend.

3.3.3 Effect of Salt Concentration on Micelle Assembly Behavior

When micelles are prepared in water with simple mixing, SAXS shows spherical micelle formation in most cases. Micelles prepared in PBS yield wormlike micelles. Figure 3.6a and 3.6b show these trends for micelles prepared with a PEG10k block copolymer and dhDNA. Generally, longer PLK blocks yield larger micelles, as seen above. Both the elongation and size behaviors are clearly shown in the PLK50 and PLK100 cases, as well as the PLK30 PBS case (Figure 3.6c). These trends also hold

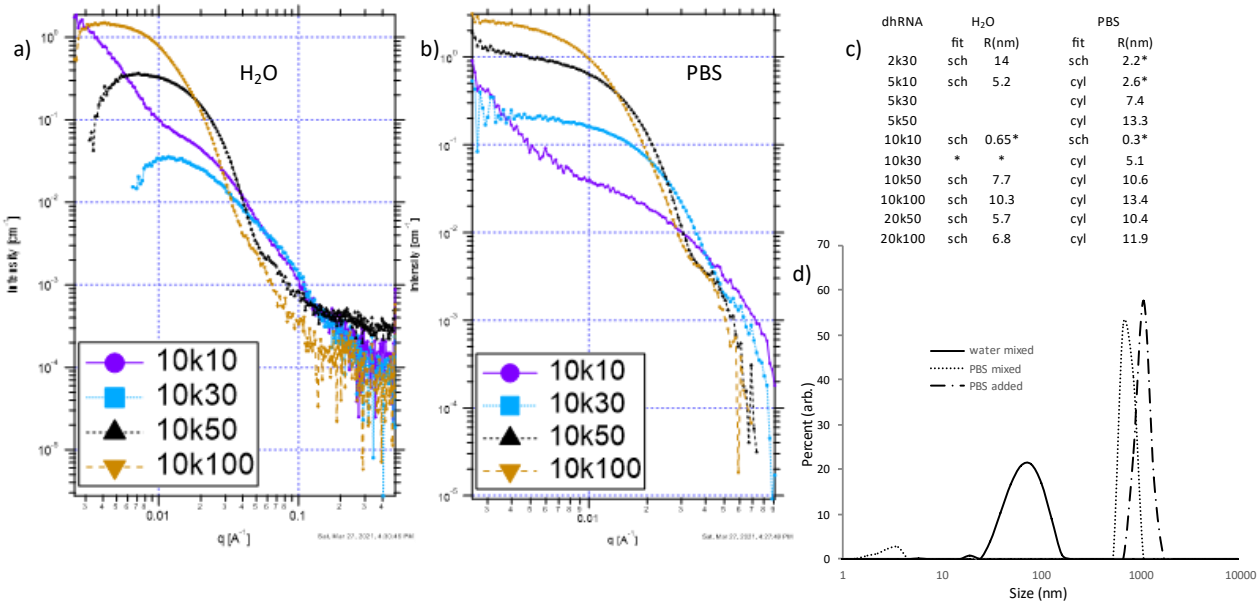

dhRNA	H_2O		PBS	
	fit	R(nm)	fit	R(nm)
2k30	sch	14	sch	2.2*
5k10	sch	5.2	cyl	2.6*
5k30			cyl	7.4
5k50			cyl	13.3
10k10	sch	0.65*	sch	0.3*
10k30	*	*	cyl	5.1
10k50	sch	7.7	cyl	10.6
10k100	sch	10.3	cyl	13.4
20k50	sch	5.7	cyl	10.4
20k100	sch	6.8	cyl	11.9

Figure 3.6. a) SAXS of dhRNA 10kPEG prepared in water. The form factors indicate spheroidal character in the ensembles, with increasing size as polylysine length increases. While the behavior of 10k10 micelles is not clear due to the presence of a Porod-like region at low q, the larger block copolymer preparations show clear spherical form factors. b) SAXS of dhRNA 10kPEG prepared in 1x PBS. Preparation in PBS results consistently in wormlike micelles. Micelles with larger polylysine blocks have a larger radius. c) table of SchulzSpheres and Cyl_PolyRadius fits of water- and PBS-prepared micelles. Water prepared micelles fit to spherical form factors. PBS-prepared micelles have slightly larger Rg, and fit to cylindrical form factors. d) DLS size histogram of micelles prepared in water or PBS, plus a rerun of the sample prepared in water after dilution with PBS and standing 15 minutes at room temperature ("water-PBS"). The water-PBS sample shows that addition of salt quickly elongates micelles, as though they had been initially mixed in PBS, whereas a "water-water" dilution behaved like micelles mixed in water (not shown). Further testing of this phenomenon showed similarly that micelles prepared by salt annealing, i.e. mixed in salt, and left to equilibrate by dialysis into water, behave exactly as micelles mixed in PBS by DLS (Figure 3.7b). * = Fit is poor. This may be due to overlapping form factors wherein one ensemble is much larger and higher-signal than the ensemble captured by the SAXS.

generally for the PEG5k and PEG 20k cases. PBS causes unusual DLS behavior in these micelles. When prepared in water, the micelles scatter at a consistent intensity, and can be fit via a CONTIN or other regularization size fitting. When prepared or dialyzed from salt or PBS, DLS autocorrelation converges more slowly, but the scattering intensity will be inconsistent within the same sample even when measured successively, without clear trend in the intensity. This behavior is observed in samples

prepared in salt or PBS, including samples mixed in water then diluted with PBS (Figure 3.6d). The behavior manifests within 15 minutes of the addition of salt. Furthermore, samples mixed in salt or PBS, then treated by dialysis against water to remove the salt, retain this behavior as well.

3.3.4 Micelle Assembly Behavior Arising from Surface Peptide Charge

Density, Polylysine Length

DLS analysis of charged surface peptides (K7, K2Q5, mimic) mixed with dhRNA in water show similar sizes and are slightly but not significantly larger than the Q7-conjugated PEG-PLKs (Figure 3.7). As seen in 3.3.3, the addition of PBS causes highly variable DLS correlation and size measurements arising from elongation of the micelles. The SAXS measurements show that there is more complexity to the assemblies than DLS shows. As seen in Figure 3.8, the relative similarity of

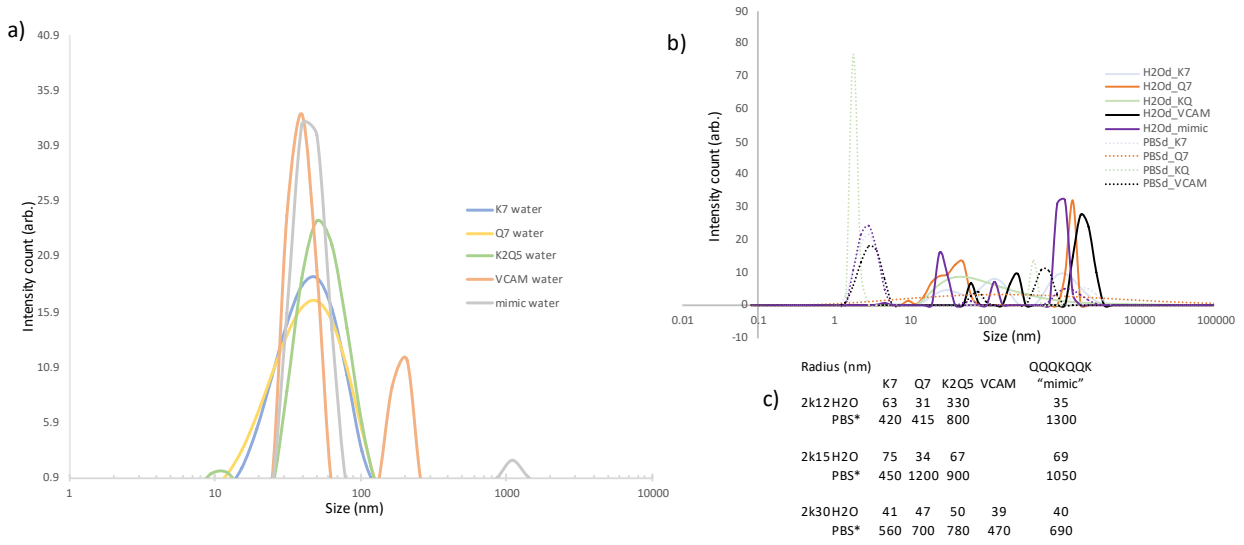

c)

Radius (nm)	K7	Q7	K2Q5	VCAM	QQQKQQK "mimic"
2k12H2O	63	31	330		35
PBS*	420	415	800		1300
2k15H2O	75	34	67		69
PBS*	450	1200	900		1050
2k30H2O	41	47	50	39	40
PBS*	560	700	780	470	690

Figure 3.7 a. DLS regularization fit of dhRNA 2k30 micelles prepared in water. Surface peptide charge has minimal effect on size. b. Micelles dialyzed from PBS show highly variable regularization fit, even if dialyzed into water ("H2Od" samples). The correlation curves (not shown) of the micelles showed widely variable intensity even within successive runs of the same sample. Contrast with the water-prepared micelles from a., which show a consistent calculated hydrodynamic radius. c. Approximate radii of micelles prepared with variable surface peptide sequences, by DLS. *PBS-prepared micelle regularizations are provided but are highly variable from sample to sample.

particle sizes identified by DLS misses a very deep shape dependence seen in the SAXS form factors. Most clearly, the charge-mimic peptide micelles have nearly spherical assembly, the Q7 peptide micelles have a wormlike chain shape, and the K7, K2Q5, and VCAM-binding micelles have fractal form factors, suggesting aggregated particles. The Q7 peptide micelles are found to have a 7.3 nm radius, 23 nm Kuhn length, and when taken with the DLS R_h of 40nm, a contour length of 1.3 μm. The mimic peptide micelles are more spheroid, but are somewhat rodlike. They have a 13 nm radius, which when taken with their R_h suggests an approximate 70 nm length. Both micelles exhibit DNA packing and liquid chainlike structure in their cores. The K7 and K2Q5 have structural curvature at q = 0.06 A^{-1}, which suggests that the aggregates are in fact composed of spheres with a building block radius of 1.6 nm. The K7 and K2Q5 fractals also have liquid cores with flexible-chain structure. The correlation lengths of 36.1 and 47 nm also agree with their hydrodynamic radii, and both suggest a

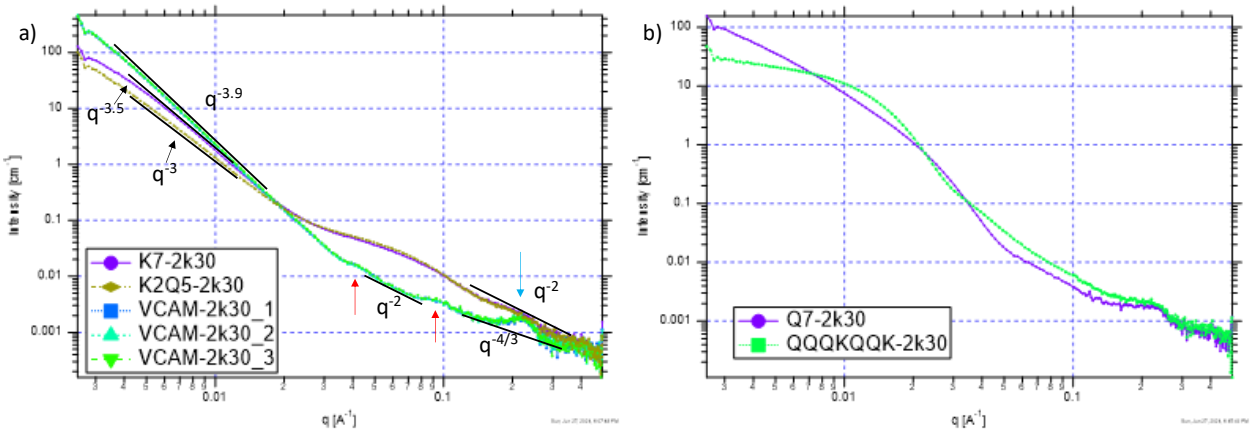

Figure 3.8 SAXS of peptide-2k30 dhRNA micelles prepared in water. a) fractal structures present in the cases of K7, K2Q5, and VHPKQHR (VCAM-targeting) peptides. The K7 and K2Q5 aggregates have wormlike internal structure with correlation lengths 36.1 nm and 47 nm, respectively, in agreement with a crew-cut structure and 4 nm PEG corona. The three VCAM samples, prepared in immediate succession with each other, show a large aggregated or spherical structure, which resolves to wormlike chains at approximately the 15 nm scale, and to semi-rigid chains at the 6.9 nm scale. The structure also contains a prominent DNA interhelix packing peak. b) Q7-2k30 assembles into wormlike structure 7.3 nm radius and 23 nm Kuhn length, and 1.3 μm contour length. The mimic-2k30 assembles into a rodlike structure with a 13 nm radius.

crew-cut PEG layer of approximately 4 nm. The VCAM micelle samples, however, have a Porod law slope at low q, indicating high signal from a much larger structure, as seen in the DLS data. However, some peaks do arise at q = 0.041 A^{-1} and 0.09 A^{-1}, corresponding to 15.3 and 6.9 nm respectively (Figure 3.8a, red arrows). The DNA packing peak at q = 0.21 A^{-1} is also much more prevalent in the VCAM sample than the others (cyan arrow). The shift of power law to chainlike occurs at a similar length scale to the Q7 and mimic peptide cases, so it is likely that the core of the structure is liquid, but densely packs into large aggregates. Finally, all the form factors show two common structural features of dhRNA micelles. First, there is a broad peak at q = 0.21 A^{-1}, most prominent in the VCAM form factor but present in all the 2k30 structures. Second, in all these structure factors there is a power law decay between the larger features of the structure factor and this peak which suggests a swollen chain structure, even in the nonfractal structure factors, implying a liquid core structure.

3.4 Discussion

3.4.1 Effect of Nucleic Acid on Micelle Assembly

While long double-stranded DNA is known to precipitate and long single-stranded RNA is known to liquid-liquid phase separate when mixed with polycations, the behavior of shorter nucleic acids has only recently begun to be studied[10,37–40]. The double-hairpin nucleic acid complex micelles are to our knowledge a novel system, and the underlying complexation is not yet well studied. The siRNA and siDNA, which are 21bp double-stranded nucleic acids, assemble into wormlike structures, while the dhRNA and dhDNA cases, which are novel, assemble into spherical micelles in the 5k and 10k PEG cases. Core behavior appears to be related to the state of the polyionic complex, with coacervates tending to form Gaussian chains in the core and solid precipitates favoring rigid-rod behavior[41–43]. Our group has reported the phase behavior of the complexes to be driven by the hybridization of the

nucleic acid in the core, with rodlike shape arising from the high charge density of double-stranded nucleic acid[10,44], but the double-hairpin nucleic acid case has not been explored. The double-hairpin nucleic acid appears to behave like a 39bp nucleic acid with 23 charges removed, which yields 71% of the charge density of a ds39 molecule. It stands to reason that this is near a critical charge density for the assembly of wormlike micelles, and lends further evidence that the increased flexibility of the single-stranded 23nt moiety does not influence the assembly so much as the reduced charge density does. The core structure also shows a dependence on the charge density of the PECs. The dsDNA-core micelles showed a rigid-rod form factor at the size scale of the polymer complexes, along with a mass fractal form factor at length scales as large as the diameter of the micelles. These observations suggest that the rodlike micelles have rigid precipitate cores with a networked or porous structure. One possibility for this structure is that the precipitates have trapped solvent or PEG within the core. However, as most polymer models assume a uniform scattering length density, without trapped solvent, this assertion is difficult to prove from the scattering data. What can be observed, however, is that the dsDNA micelles are themselves rodlike with rodlike polymer complexes in their cores, which raises the question of whether the shape of precipitated complexes predicts the shape of the micelles. Contrast with the dhDNA-core micelles, which have Gaussian chain behavior in the core, suggesting the complexes remain flexible and behave like a liquid within the micelle, though we have not yet directly studied the complexation of double-hairpin nucleic acids outside the context of micelles. The core structure of the micelles does not appear to predict or correlate strongly to the shape of the micelles themselves. PECs composed of double-stranded nucleic acid are capable of parallel packing in the core[44], and this can be observed in many of the liquid-core micelles. The rodlike precipitates, however, appear not to exhibit any consistent packing distance, which suggests that the precipitate mass fractal cores are amorphous in structure.

3.4.2 Effect of copolymer block lengths

While research has pointed to the length of the polyelectrolyte and neutral blocks as having a significant effect on the shape and size of the resulting micelles, an unclear pattern of size dependence still hinders rational design of polyelectrolyte complex micelles[26,45]. Jung et al. showed how a PAEMA60 cationic-neutral block copolymer showed that changing the N/P ratio from 1 to 1.5 changed the size dependence trends for neutral PEG, P(OEGMA) and PMAG blocks of similar contour length, from steric bulk to colloidal stability-dominated[27]. Harada and Kataoka have shown that block copolymer length could influence micelle size by affecting the density of the PEG shell layer of the micelle[45]. Previous work by our group and others[10,44,46] has shown that in the cases of ssDNA and dsDNA-core micelles, that the size of micelle cores decrease slightly with increasing PEG block length, while micelle size increased with increasing PLK block length. These trends have been shown to arise from changes in aggregation number, with increasing PEG reducing aggregation number and increasing PLK length increasing aggregation number[47]. Work by van der Kooij et al. has also shown micelles become more stable as the charged block of the copolymer or the homopolymer length is increased[46]. My work not only shows the same size dependences in the case of dsDNA, but further extends this trend to dhDNA-core micelles. That dhDNA-core micelles seem to have some shape dependence on the copolymer block lengths is novel. While my work is a preliminary look into this trend, it appears that there is a weak correspondence between PEG/PLK ratio and micelle shape, with higher ratios corresponding to spherical assembly. However, this forcing can easily be overwhelmed by the charge density of the nucleic acid itself, as the effect of block copolymer length ratio is too small to drive changes in shape near ssDNA or dsDNA-like charge densities. The dhDNA is likely near enough a critical charge density to allow a high PEG/PLK copolymer to form spherical micelles.

The purpose of analyzing micelle size and shape differences arising from the length of the polylysine in the core was to determine if a pattern could be established, analogous to the hydrophobic core volume of Israelachvilli's packing parameter[48]. When I set out to answer this question, I had reasoned that a larger core polylysine would necessitate a higher assembly number, as more nucleic acid is needed to neutralize the charge. This would increase core volume relative to the PEG area, which leads to a tendency to form elongated or worm-like structures in the hydrophobic case, but in the PEC case could also simply form a larger micelle. SAXS shows that the picture is too complex to directly apply the packing parameter theory to all PECs. While indeed the increase of PLK leads to a larger micelle because of increased core size, the nucleic acid charge density provides a set of assembly forces different from the hydrophobic force, and it is only at a charge density intermediate between single-stranded and double-stranded nucleic acid-polylysine complexes that we see a regime wherein Israelachvilli's design principles in terms of PEG area against PEC volume can help us predict micelle shape. Outside that critical region, we are instead likely to see spheres near single-stranded nucleic acid charge density and worms near double-stranded nucleic acid charge density. Future theoretical work could, however, focus on the critical region to determine whether the behavior of PECs of comparable charge density to dhDNA PECs exhibit forces comparable to the hydrophobic force, such that Israelachvilli's design principle would aid shape control of PEC micelles in this case.

3.4.3 Effect of salt

The major motivation for characterizing micelles in salt arose from observations that the VCAM-2k30 micelles in Kuo et al. were characterized from mixing in pure water[33]. Reasoning that injection volumes for human use are potentially large enough to cause local cytolysis at the site of injection, and that regardless the micelles could equilibrate *in situ*, I began characterizing micelles formed in PBS. Expecting spheres at the time, the poor convergence of the DLS data seemed indicative of

experimental error, but with time, and a reevaluation of my own assumptions along with concurrent work by labmates[10,44], it became clear the micelles were likely equilibrating with wormlike structure, and that the spherical micelles were likely a kinetically trapped state. This is not too surprising, since it is known both that solid polyelectrolyte complex precipitates typically liquefy at higher salt concentrations, and that polyelectrolyte complex core micelles composed of one block copolymer and one homopolymer tend to elongate with increasing salt, from spheres to worms to lamellae[44,46,49,50]. The results support some interesting conclusions. Salt does equilibrate the structure of the micelles, in concordance with the annealing procedure outlined in Lueckheide et al[44]. Rapid equilibration observed in the dilution experiments in DLS suggest that when we have injected VCAM1-targeting miR92a-inhibitor (a dhRNA) micelles into mice, the micelles equilibrate in the blood and may target *in situ* as wormlike structures, rather than spherical, regardless of the shape of the micelles at injection. Comparing the dilution of aqueous concentrated micelles with more water to dilution of aqueous micelles with PBS suggests that the equilibration of the micelles due to salt occurs within 15 minutes of the introduction of salt at room temperature. This result suggests strongly that the characterization of the micelles in 1x PBS solution is more indicative of the state of the micelles at the time of injection, as well as during blood circulation post-injection. As will be discussed in Chapter 4, PEG2k-PLK30 micelle is utilized as a delivery vehicle for miR92a inhibitor RNA. The rapid equilibration of micelles to wormlike structure in PBS implies that delivery of the miR92a inhibitor in an injection occurs via these wormlike micelles, although we have not attempted a direct observation of the binding event *in situ*. Further complicating this observation is the SAXS data, which indicates the presence of rodlike, but very short micelles where we would expect elongation. It is possible the micelles in the salt-addition experiments are RNA-core micelles and susceptible to autohydrolysis in a wider range of conditions than the DNA-core micelles. While the DLS experiments were carried out immediately upon mixing, the SAXS experiments were generally carried

out hours after mixing, and while the PBS was nuclease-free, it did not specify a Ca^{2+} or Mg^{2+} concentration. To minimize risk of breakdown, future SAXS samples should be mixed proximate to the experiment using definitively Mg/Ca-free salt. However, it is also possible that to understand the scaling of my micelles, we must distinguish discussion of the core radius from that of the hydrodynamic radius of the micelles. The DLS measures hydrodynamic radius, and the elongation observed in my experiments is consistent with other direct observations of hydrodynamic radius[46]. The SAXS measures the core radius, and the scaling theory of Rumyantsev et al. discusses how at higher salt concentrations the core radius decreases to a critical point, at which point micelles either dissolve or become rodlike depending upon the stability of the polyelectrolyte complex[50]. This could explain the apparent paradox in my results and suggests that experiments evaluating core behavior with increasing salt via SAXS in tandem with the hydrodynamic radius measurements of DLS could elucidate the differing behaviors of the micelles and their core with salt concentration.

While the formation of spherical particles, including micelles, remains a popular strategy for its simplicity and relative ease of characterization, wormlike micelles are emerging as a viable alternative because they offer the advantages of higher loading capacity, higher efficacy, and longer circulation in the blood stream[25,51–53]. Dalhaimer et al. demonstrated these advantages using biotinylated wormlike micelles with a 1 μm contour length to bind an avidin-coated surface, showing that the micelles retained high dynamic stability while also adsorbing completely to the avidin surface. Kim et al. used PLA micelles that would self-shorten in circulation, during which the cargo would be released over time, but furthermore showed that the longer wormlike micelles were able to navigate through porous gels that stopped 100 nm spheroids because of their ability to flex through the pores. Christian et al. observed how 1 μm flexible filaments could persist in circulation for over one day after intravenous injection, doubling the IC_{50} of paclitaxel cargo, with likely similar effect for other chemotherapeutic cargo as well. The wormlike micelle delivery is likely to allow many VCAM1

binding interactions scattered on a flexible micelle surface providing a dosing advantage over spherical particles[54,55]. Such additive affinity, along with the increased loading capacity, would allow for high overall binding affinity to VCAM1 expressed on the surface of inflamed endothelial cells, and therefore a high delivery efficacy of miR92a-inhibitor. Dalheimer et al. also proposed two possible mechanisms for wormlike micelle uptake by endocytosis. The first mechanism proposes that the entire micelle is pulled in whole by folding, and the second proposes that the micelle is broken into smaller pieces by the endocytic vesicles and taken in as multiple smaller pieces. While the exact mechanism is beyond the scope of my research, it is clear that wormlike micelles have an advantage for cellular delivery over spheroid micelles.

3.4.4 Effect of Surface Charge

When I set out on this project, one of the first questions I had was whether the charge of the VCAM targeting peptide (+2) had a significant effect on the size or shape of the micelle, because I had often run DLS and SAXS simply to run into wormlike and aggregated structures consistently. In addition, the low delivery rate of passive targeting merits having a binding peptide on the surface, if it does not strongly hinder the assembly[56]. There is a small swelling of the surface-charged micelles in water, suggesting a possible association of water with the micelle surface, or electrostatic polymer-polymer repulsion effects causing the charged surface peptides to straighten out more in solution. In contrast, the uncharged Q7 peptide would associate with the PEG layer more strongly, reducing the effective size of the micelle for diffusion. I had also speculated on the possibility that the charged peptides could rearrange themselves to associate with the RNA in the core, but since increased surface charge seems to increase size if anything, it is unlikely that the surface peptide is inverting into the core. The SAXS shows that there are indeed charge-related differences but that the story is much more complex than just whether the surface peptide is charged. The uncharged Q7 peptide micelle fits closely to a

flexible chain model, and thus likely is forming long, flexible wormlike micelles. The VCAM-mimicking peptide (QQQKQQK-2k30) assembles into distinct spheres and appears to avoid aggregation. However, the other charged peptide micelles aggregate into larger fractal structures. Srivastava et al. showed similar behavior in charged-neutral-charged triblock copolymer hydrogels, and indicated that at low polymer concentrations the polymers form disordered aggregates of spheres[57]. It is possible that charged peptides are associating with trace free RNA that did not complex into the cores, and the high ratio of peptides needed to neutralize the RNA charge (55:7 or 55:2) leads to bridging of micelles, creating a meshlike network of disordered micelles that appear in SAXS as fractals. If this is the case, then salt addition below the critical concentration for coacervate formation is likely to break up the aggregates. While the DLS of surface-peptide micelles prepared in PBS did not appear to show this, it is possible that an understanding of the behavior of the micelles themselves in response to salt will assist the understanding of the aggregation behavior and testing for breakup of the aggregates.

3.5 Conclusions

Taken as a whole, the main parameters that influence the assembly of oligonucleotide-core PEC micelles are the charge density of the nucleic acid, the length of the polylysine block that forms the PEC, the salt concentration of the solution to which the micelles are exposed, and the charge of the outer binding peptide. The high charge density of the double-stranded nucleic acid promotes rodlike micelles at equilibrium, which salt quickly facilitates. Longer polylysine yields larger micelle radius. Addition of salt appears to elongate micelles without appreciable elongation of the core. The sequence of the nucleic acid and the sequence of the surface peptide have little if any influence on assembly, though the charge of the peptide can cause unexpected assembly behavior and aggregate formation.

To further understand the tunability of these micelles for targeted nucleic acid delivery applications, experiments resolving the relationship of core size and structure to micelle size and structure with increasing salt are warranted, with attention to the presence of factors that degrade DNA or interfere with SAXS signal, to understand why despite such long micelles form as measured by hydrodynamic radius their core appears to swell only slightly and not elongate accordingly in SAXS. Having discerned a cause for that behavior, one can apply that knowledge to the design and analysis of experiments probing the aggregation behavior of micelles functionalized with charged molecules on their surface, and the effect of adding salt to those aggregates. These experimental results should solidify our understanding of the behavior of these micelles when injected into biological systems.

Chapter Bibliography

1. G Bungenberg De Jong, B. H. & Kruyt, H. R. *Chemistry.-Coacewation (Partial miscibility in colloid systems). (Preliminary Communication)*. (1929).
2. Bucur, C. B., Sui, Z. & Schlenoff, J. B. Ideal mixing in polyelectrolyte complexes and multilayers: Entropy driven assembly. *J. Am. Chem. Soc.* **128**, 13690–13691 (2006).
3. Spruijt, E., Westphal, A. H., Borst, J. W., Cohen Stuart, M. A. & Van Der Gucht, J. Binodal compositions of polyelectrolyte complexes. *Macromolecules* **43**, 6476–6484 (2010).
4. Priftis, D., Laugel, N. & Tirrell, M. Thermodynamic Characterization of Polypeptide Complex Coacervation. *Langmuir* **28**, 15947–15957 (2012).
5. Overbeek, J. T. & Voorn, M. J. Phase separation in polyelectrolyte solutions; theory of complex coacervation. *J. Cell. Physiol. Suppl.* **49**, (1957).
6. Veis, A. & Aranyi, C. Phase separation in polyelectrolyte systems. I. Complex coacervates of gelatin. *J. Phys. Chem.* **64**, 1203–1210 (1960).
7. Kudlay, A., Ermoshkin, A. V., De La Cruz, M. O. & Olvera De La Cruz, M. Complexation of Oppositely Charged Polyelectrolytes: Effect of Ion Pair Formation. *Macromolecules* **37**, 9231–9241 (2004).
8. Fu, J. & Schlenoff, J. B. Driving Forces for Oppositely Charged Polyion Association in Aqueous Solutions: Enthalpic, Entropic, but Not Electrostatic. *J. Am. Chem. Soc.* **138**, 980–990 (2016).
9. Record, M. T., Anderson, C. F. & Lohman, T. M. Thermodynamic analysis of ion effects on the binding and conformational equilibria of proteins and nucleic acids: The roles of ion association or release, screening, and ion effects on water activity. *Q. Rev. Biophys.* **11**, 103–178

(1978).

10. Vieregg, J. R. *et al.* Oligonucleotide−Peptide Complexes: Phase Control by Hybridization. *J. Am. Chem. Soc.* **140**, 1632–1638 (2018).

11. De Kruif, C. G., Weinbreck, F. & De Vries, R. Complex coacervation of proteins and anionic polysaccharides. *Current Opinion in Colloid and Interface Science* **9**, 340–349 (2004).

12. Mascotti, D. P. & Lohman, T. M. Thermodynamic extent of counterion release upon binding oligolysines to single-stranded nucleic acids. *Proc. Natl. Acad. Sci. U. S. A.* **87**, 3142–3146 (1990).

13. Israelachvili, J. N. Soft and Biological Structures. in *Intermolecular and Surface Forces* 535–576 (Elsevier, 2011).

14. Zajac, J., Chorro, C., Lindheimer, M. & Partyka, S. Thermodynamics of micellization and adsorption of zwitterionic surfactants in aqueous media. *Langmuir* **13**, 1486–1495 (1997).

15. Kim, W., Yamasaki, Y., Jang, W. D. & Kataoka, K. Thermodynamics of DNA condensation induced by poly(ethylene glycol)- block -polylysine through polyion complex micelle formation. *Biomacromolecules* **11**, 1180–1186 (2010).

16. Dowdy, S. F. Overcoming cellular barriers for RNA therapeutics. *Nature Biotechnology* **35**, 222–229 (2017).

17. Juliano, R. L. The delivery of therapeutic oligonucleotides. *Nucleic Acids Research* **44**, 6518–6548 (2016).

18. Allen, T. M. & Cullis, P. R. Liposomal drug delivery systems: From concept to clinical applications. *Advanced Drug Delivery Reviews* **65**, 36–48 (2013).

19. Kanasty, R., Dorkin, J. R., Vegas, A. & Anderson, D. Delivery materials for siRNA therapeutics. *Nature Materials* **12**, 967–977 (2013).

20. Lorenzer, C., Dirin, M., Winkler, A. M., Baumann, V. & Winkler, J. Going beyond the liver:

Progress and challenges of targeted delivery of siRNA therapeutics. *Journal of Controlled Release* **203**, 1–15 (2015).

21. Lächelt, U. & Wagner, E. Nucleic Acid Therapeutics Using Polyplexes: A Journey of 50 Years (and Beyond). *Chem. Rev.* **115**, 11043–11078 (2015).

22. Ponnuswamy, N. *et al.* Oligolysine-based coating protects DNA nanostructures from low-salt denaturation and nuclease degradation. *Nat. Commun.* **8**, (2017).

23. Voets, I. K., de Keizer, A. & Cohen Stuart, M. A. Complex coacervate core micelles. *Advances in Colloid and Interface Science* **147–148**, 300–318 (2009).

24. Champion, J. A., Katare, Y. K. & Mitragotri, S. Particle shape: A new design parameter for micro- and nanoscale drug delivery carriers. *Journal of Controlled Release* **121**, 3–9 (2007).

25. Venkataraman, S. *et al.* The effects of polymeric nanostructure shape on drug delivery. *Adv. Drug Deliv. Rev.* **63**, 1228–1246 (2011).

26. Tockary, T. A. *et al.* Tethered PEG Crowdedness Determining Shape and Blood Circulation Profile of Polyplex Micelle Gene Carriers. *Macromolecules* **46**, (2013).

27. Jung, S., Lodge, T. P. & Reineke, T. M. Structures and Protonation States of Hydrophilic-Cationic Diblock Copolymers and Their Binding with Plasmid DNA. *J. Phys. Chem. B* **122**, 2449–2461 (2018).

28. Miyata, K., Christie, R. J. & Kataoka, K. Polymeric micelles for nano-scale drug delivery. *React. Funct. Polym.* **71**, 227–234 (2011).

29. Miyata, K., Nishiyama, N. & Kataoka, K. Rational design of smart supramolecular assemblies for gene delivery: Chemical challenges in the creation of artificial viruses. *Chem. Soc. Rev.* **41**, 2562–2574 (2012).

30. Scholz, C. & Wagner, E. Therapeutic plasmid DNA versus siRNA delivery: Common and

different tasks for synthetic carriers. *Journal of Controlled Release* **161**, 554–565 (2012).

31. Hayashi, K. *et al.* Macromol. Rapid Commun. 6/2016. *Macromol. Rapid Commun.* **37**, 560–560 (2016).

32. Kwok, A., McCarthy, D., Hart, S. L. & Tagalakis, A. D. Systematic Comparisons of Formulations of Linear Oligolysine Peptides with siRNA and Plasmid DNA. *Chem. Biol. Drug Des.* **87**, 747–763 (2016).

33. Kuo, C. H. *et al.* Inhibition of atherosclerosis-promoting microRNAs via targeted polyelectrolyte complex micelles. *J. Mater. Chem. B* **2**, 8142–8153 (2014).

34. Provencher, S. W. A Constrained Regularization Method for Inverting Data Represented by Linear Algebraic or Integral Equations. *Comput. Phys. Commun.* 213–227 (1982).

35. Ilavsky, J. & Jemian, P. R. Irena: Tool suite for modeling and analysis of small-angle scattering. *J. Appl. Crystallogr.* **42**, 347–353 (2009).

36. Kline, S. R. Reduction and analysis of SANS and USANS data using IGOR Pro. *J. Appl. Crystallogr.* **39**, 895–900 (2006).

37. Shapiro, J. T., Leng, M. & Felsenfeld, G. Deoxyribonucleic acid-polylysine complexes. Structure and nucleotide specificity. *Biochemistry* **8**, 3219–3232 (1969).

38. Aumiller, W. M. & Keating, C. D. Phosphorylation-mediated RNA/peptide complex coacervation as a model for intracellular liquid organelles. *Nat. Chem.* **8**, 129–137 (2016).

39. Aumiller, W. M., Pir Cakmak, F., Davis, B. W. & Keating, C. D. RNA-Based Coacervates as a Model for Membraneless Organelles: Formation, Properties, and Interfacial Liposome Assembly. *Langmuir* **32**, 10042–10053 (2016).

40. Raspaud, E., Olvera De La Cruz, M., Sikorav, J. L. & Livolant, F. Precipitation of DNA by polyamines: A polyelectrolyte behaviour. *Biophys. J.* **74**, 381–393 (1998).

41. Spruijt, E. *et al.* Structure and dynamics of polyelectrolyte complex coacervates studied by

scattering of neutrons, X-rays, and light. *Macromolecules* **46**, 4596–4605 (2013).

42. Marciel, A. B., Srivastava, S. & Tirrell, M. V. Structure and rheology of polyelectrolyte complex coacervates. *Soft Matter* **14**, 2454 (2018).

43. Marciel, A. B., Chung, E. J., Brettmann, B. K. & Leon, L. Bulk and nanoscale polypeptide based polyelectrolyte complexes. *Adv. Colloid Interface Sci.* **239**, 187–198 (2017).

44. Lueckheide, M., Vieregg, J. R., Bologna, A. J., Leon, L. & Tirrell, M. V. Structure−Property Relationships of Oligonucleotide Polyelectrolyte Complex Micelles. *Nano Lett.* **18**, 7111–7117 (2018).

45. Harada, A. & Kataoka, K. Effect of Charged Segment Length on Physicochemical Properties of Core-Shell Type Polyion Complex Micelles from Block Ionomers. *Macromolecules* **36**, 4995–5001 (2003).

46. Van Der Kooij, H. M. *et al.* On the stability and morphology of complex coacervate core micelles: From spherical to wormlike micelles. *Langmuir* **28**, 14180–14191 (2012).

47. Marras, A. E., Campagna, T. R., Vieregg, J. R. & Tirrell, M. V. Physical Property Scaling Relationships for Polyelectrolyte Complex Micelles. *Macromolecules* **54**, 6585–6594 (2021).

48. Israelachvili, J. N. *Intermolecular and surface forces*. (Academic Press, 2011).

49. Wang, Q. & Schlenoff, J. B. The polyelectrolyte complex/coacervate continuum. *Macromolecules* **47**, 3108–3116 (2014).

50. Rumyantsev, A. M., Zhulina, E. B. & Borisov, O. V. Scaling Theory of Complex Coacervate Core Micelles. *ACS Macro Lett.* **7**, 811–816 (2018).

51. Dalhaimer, P., Engler, A. J., Parthasarathy, R. & Discher, D. E. Targeted worm micelles. *Biomacromolecules* **5**, 1714–1719 (2004).

52. Kim, Y., Dalhaimer, P., Christian, D. A. & Discher, D. E. Polymeric worm micelles as nano-carriers for drug delivery. *Nanotechnology* **16**, (2005).

53. Christian, D. A. *et al.* Flexible filaments for in vivo imaging and delivery: Persistent circulation of filomicelles opens the dosage window for sustained tumor shrinkage. *Mol. Pharm.* **6**, 1343–1352 (2009).

54. Truong, N. P., Whittaker, M. R., Mak, C. W. & Davis, T. P. The importance of nanoparticle shape in cancer drug delivery. *Expert Opinion on Drug Delivery* **12**, 129–142 (2015).

55. Katterman, C., Pierce, C. & Larsen, J. Combining Nanoparticle Shape Modulation and Polymersome Technology in Drug Delivery. *ACS Appl. Bio Mater.* **4**, 2853–2862 (2021).

56. Willhelm, S. *et al.* The possibility of engineering nanoparticles. *Nat. Rev. Mater.* **1**, (2016).

57. Srivastava, S., Levi, A. E., Goldfeld, D. J. & Tirrell, M. V. Structure, Morphology, and Rheology of Polyelectrolyte Complex Hydrogels Formed by Self-Assembly of Oppositely Charged Triblock Polyelectrolytes. *Macromolecules* **53**, 5763–5774 (2020).

Chapter 4
Delivery of miR92a microRNA Inhibitor *in vivo* using VCAM-1-targeting Polyelectrolyte Complex Micelles to Treat Atherosclerosis

Chapter Abstract

Mixing of PEG-PLK and RNA forms polyelectrolyte complex (PEC) micelles that protect the RNA in the core and permit functionality at the surface. Here we demonstrate the capabilities of PEC micelles by functionalizing the PEG-PLK with a VCAM-1 targeting peptide before mixing with miR92a inhibitor RNA to form wormlike aggregate micelles. These micelles are then shown to prevent plaque formation in atherosclerosis-susceptible mice.

4.1 Introduction

Polyelectrolyte micelles have a high potential as therapeutic delivery agents, and have been employed for the delivery of small molecules[1,2] and nucleic acids[3–5]. The micelle delivery strategy has several advantages, but several challenges. The greatest advantages of micelles are spontaneous assembly, potential for specific cell delivery via active targeting, and modular functionality[6,7]. It is possible to assemble micelles wherein the cargo hold in the core, the protective shell, and the targeting moiety are all replaceable in the design, so that the same overall micelle structure can be used for different

cell tissues and different therapeutic targets. It is also possible to use covalent linkages that break in certain conditions, as Oishi showed using acid-labile linkages in an siRNA-core complex micelle[8,9]. The main challenges of the micelle delivery strategy arise from the size of the micelles, as in general spherical particles over 100 nm or under 10 nm in diameter will be filtered out by the liver and kidneys, respectively[6,7]. In addition, the binding affinity of the micelles, which affects dosage, and immune response to the micelles are also important considerations when designing a delivery system[10,11]. To address these challenges, the community has found the use of nonspherical particles to be of interest[12–15]. Christian et al. demonstrated that filamentous micelles were able to evade biological filtration systems, which increased circulation time and reduced the needed dosage for therapeutic effect or diagnostic imaging, while Champion et al. found that macrophages could not bind the low-curvature length of elongated micelles, which prevented phagocytic destruction of the micelles[10,11]. In addition to the shape, the use of poly(ethylene glycol) (PEG) as a shell moiety has been shown to reduce the immunogenicity of the micelles *in vivo*, because PEG is biologically inert. However, care must be taken that the PEG does not interfere with uptake into the target tissue, because PEG is biologically inert[14,16]. Furthermore, while the micelle strategy has been employed to deliver DNA and siRNA, little is known about the delivery of RNA assembled into other secondary structures[16–18]. My work here aims to extend earlier work by the Tirrell group by delivering RNA-based inhibitors of miRNA *in vivo*[19,20]. The inhibitors have a double-hairpin structure with a single-stranded linker as the active moiety, and much of the assembly dynamics of the inhibitors in coacervate complex core micelles is covered in Chapter 3.

We chose to address atherosclerosis because its pathology is well suited to the targeted coacervate complex micelle strategy[21]. Atherosclerosis develops as a chronic disease, characterized by the buildup of fatty plaques under the endothelial lining of the arteries[22]. The lipid buildup causes inflammation and an immune response, but the macrophages, ill-suited to clear lipids, die within the

tissue as foam cells, so named for their spongy appearance[23]. The necrosis of the foam cells adds to the inflammation in a positive feedback loop, and eventually the buildup begins to break into and occlude the blood vessel, at which point it is covered by a fibrous cap[2425]. Eventually the fibrin in the cap wears down and the cap ruptures, which can result in fatal consequences such as heart attack or stroke[26]. Because atherosclerosis is a disease of immune dysfunction at its core, much work has focused on the pathways that govern immune response to the endothelial lining of the arteries, and further work has sought targets for atherosclerosis-specific delivery[25,27–29]. Davies et al. showed the role that the adhesion molecules VCAM-1, ICAM-1, PECAM, and E-selectin played in binding the integrins of the monocytes in the early stage of the disease[30]. Nakashima et al. demonstrated that *apoE*$^{-/-}$ mice expressed upregulated VCAM-1 and ICAM-1 in lesion-prone sites, suggesting a connection between the inflammation and subsequent disease progression[31]. Further work by Cybulsky showed that VCAM-1 knockout mice could not develop plaques, suggesting that VCAM-1 expression was causative of disease progression[32,33]. Our use of a VCAM-1 binding peptide (VHPKQHR) is informed by this causal relationship, because of the specificity of VCAM-1 expression to sites of developing plaques[34,35]. Upstream of the expression of VCAM-1 is disturbed blood flow mediated by suppression of phosphatidic acid phosphatase 2B (PPAP2B), a mechanically sensitive integral protein on the endothelial wall. At arterial branches and other sites of turbulent blood flow, PPAP2B is downregulated, which can trigger expression of microRNAs that mediate the immune response and VCAM-1 upregulation[36–41]. Among these, microRNA-92a (miR-92a) has been found to suppress the expression of Krüppel-like factor 2 (KLF2), which itself mediates vascular inflammation signaling including VCAM-1 expression[39,40,42]. The inhibition of miR-92a binding to KLF2 mRNA would therefore decrease the inflammatory response and rescue vascular cells by restoring an atherosclerosis-resistant phenotype. The work of the Fang group to establish the causal relation of miR-92a expression to atherosclerotic plaque formation and our collaboration to demonstrate the effectiveness

of our miR-92a-inhibiting PEC micelles at preventing the atherosclerotic pathway is covered in greater detail in Chapter 5.

When I began this project, our lab was interested in the use of self-assembling micelles to image the development of atherosclerosis and combat its progression. Earlier publications detail our group's work using peptide amphiphiles with REKA (fibrin-binding) peptide as well as VHPKQHR (VCAM1-binding) peptide to direct micelles to plaques via active targeting[19,43,44]. This work entailed mixing a 9:1 mixture of the targeting peptide amphiphile with Cy7 dye- or gadolinium-labeled amphiphile to enable imaging of the plaque using fluorescent imaging or magnetic resonance imaging, respectively. The Tirrell group was able to show with these peptide amphiphiles that the fibrous cap of the plaque plays an important role in late-stage lesion rupture. Naturally, the question arose if we could deliver therapeutics to inhibit plaque development or rupture. In collaboration with the Fang lab, our lab began to work to deliver miRNA inhibitors to plaques. However, given the charge of the RNA, and its fragility, it was clear a different approach would be needed to deliver the miR inhibitors. The group explored the possibility to use the charge as an asset, and focused on the polyelectrolyte complexation approach, which would assemble with the RNA in the core. Following Kataoka et al.[45], the Tirrell group pursued the strategy of using a PEG-polylysine (PEG-PLK) block copolymer for the coassembly, and attached to this the REKA and VCAM1-binding peptides to make targeting PEC micelles, which they were able to show bound to and inhibited the targeted miRNA in human endothelial cells (HECs)[20]. When I joined the project, it was clear that the PEC micelles worked *in vitro*, so the next step was to show the micelles working *in vivo*. The details of the structural relationships of the micelles, however, turned out to be less well understood than initially thought when I had joined, so the bulk of my project focused on the shape and internal structure of the micelles, which is covered in Chapter 3. Nonetheless, the characterization work could progress in parallel to the *in vivo* work. This chapter aims to show the preliminary results of our micelles treating

atherosclerosis, while Chapter 5, the resulting publication, encompasses the whole project and provides the context for these results.

4.2 Materials and Methods

4.2.1 Materials

miR92a inhibitor and control double-hairpin RNA were purchased from Dharmacon. Fmoc-protected amino acids and synthesis-grade solvents were purchased from Gyros Protein Technologies. Fmoc-PEG(2000)-COOH was purchased from JenKem. TentaGel R RAM Rink Amide (0.19mmol eq/g loading) was purchased from Rapp Polymere. Trifluoroacetic acid (TFA), triisopropylsilane (TIS), HATU, Piperidine (>98%) and N-Methylmorpholine (NMM) were purchased from Millipore-Aldrich. 2000 MWCO dialysis cartridges were obtained from Thermo Fisher. RNAse-free water and 1x PBS were purchased from New England Biolabs. VHPKQHR-PEG(2000)-PLK30 (VCAM-2k30) was synthesized using solid-phase peptide synthesis, with DMF as solvent, 0.4M NMM in DMF as base, HATU as activator, and 20% piperidine in DMF as deprotecting agent. For each step, a vial containing 4 equivalents of Fmoc amino acid and 3.9 equivalents of HATU was prepared. Rink Amide and Fmoc-lysine were used on a PS3 synthesizer (Gyros) to synthesize the PLK30, with 20 mins reaction time per amino acid. 2 equivalents Fmoc-PEG(2000)-OH with 1.9 equivalents HATU was then added by SPPS and allowed to react for 8h. For VCAM-targeting 2k30 the VHPKQHR sequence was added, 1h per amino acid using 4 equivalents amino acid and 3.9 equivalents HATU. After each addition step was a 2 x 10 min deprotection. Each step was followed with a DMF rinse to remove any unreacted agents. Beads were collected, rinsed with methanol to deswell, and dried before cleavage. Cleavage was carried out using 96% TFA, 3% water, 1%TIS, with gentle shaking for 2h. Samples were collected using DCM, allowed to evaporate to 5 mL, at which point product was collected by precipitation with 20 mL -80°C

diethyl ether. Sample was dried completely, redissolved in MilliQ 18MΩ water, and dialyzed 1 day at 3500 MWCO to remove any impurities. After dialysis, the sample was lyophilized to yield a fluffy white powder, which was stored at -20°C for stock use.

4.2.2 Formation of mir92a-Inhibiting Micelles

Stock solutions of nuclease-free 1mM miR92a inhibitor and miRNA nonsilencing control were prepared, as was 5mg/ml preparations of VCAM-PEG2k-PLK30 in water. The RNA was mixed into nuclease-free 1x PBS by vortexing. VCAM-2k30 was added for a 1:1 P/N ratio of 50 μL sample/mouse, then the solution was vortexed for 30s. Micelles were dialyzed against MilliQ water with a 2000 MWCO membrane overnight. Samples were then collected and diluted to yield 100 μL of injection sample per mouse.

4.2.3 Light Scattering Methods

Dynamic light scattering (DLS) was carried out using 50 μl samples in a Mobius-zeta dynamic scattering apparatus. Samples were measured for five seconds five times and averaged. Small-angle X-ray scattering (SAXS) was carried out at Argonne Advanced Photon Source, Beamline 12-ID-B. SAXS samples were measured using a flow cell apparatus to obtain 30 structure factors which were averaged for processing using the SANS Irena macros for size, shape, and structure determination.

4.2.4 Mouse Atherosclerosis Test by Tail Injection

The handling of the mice was carried out by the Fang lab. Transgenic *Apoe*$^{-/-}$ mice (Jackson Laboratory) were fed a high-fat diet of 21% w/w fat, 0.15% w/w cholesterol, 19.5% casein w/w (Harlan) for 8 weeks starting at age 12 weeks to develop plaques. Mice were shaved and sterilized for tail vein injection of 100 μL of 4 mg/kg or 8 mg/kg of miR inhibitor VCAM-2k30 (N = 7 @ 4 mg/kg, 8 @ 8 mg/kg), negative control miRNA VCAM-2k30 (N = 6, 5), naked miR inhibitor (N = 7, 9), or PBS (N = 8, 8).

Micelles were allowed to circulate for 1 week before mice were euthanized for *en face* analysis of aortic arch and root. *En face* analysis was also performed by the Fang lab. After sacrifice, aortas were harvested, fixed with 4% paraformaldehyde overnight at 4 °C, and stained with 2 mg/mL Oil Red O for 20 min. Aortas were rinsed with isopropanol and imaged for plaque size, which was quantified using ImageJ and normalized to average PBS control.

4.3 Results

4.3.1 Characterization of VCAM1-targeting miR92a inhibitor-loaded micelles

Micelle preparations show maximal scattering by DLS at a 1:1 charge ratio of polylysine to miR inhibitor. SAXS shows formation of dense aggregate micelles with 200nm correlation length scale when mixed in water (see Figure 3.8). Micelles prepared with nonsilencing control dhRNA show no significant difference in scattering behavior from miR92a-inhibitor micelles. Micelles formed in PBS showed broad DLS peaks and subtle SAXS scattering but too low signal for structure determination.

4.3.2 Reduction of Plaque Size Caused by VCAM1-targeted delivery of micelles carrying miR92a inhibitor

The mouse experiments were carried out by the Fang lab, who have graciously allowed me to reproduce the results of those experiments in this chapter. ApoE$^{-/-}$ mice fed a high fat diet, then injected with an 8mg/kg dosage of miR92a inhibitor show 50% reduction in atherosclerotic plaque lesion size after injection of naked miR92a inhibitor, and 75-80% reduction in lesion size after injection of miR-inhibitor-loaded VCAM1-targeting micelles, compared to PBS injection control (Figure 4.1). *En face* analysis of the aortic root shows significantly reduced fatty deposits as indicated by Oil Red O staining. These results indicate that miR92a injection is highly effective at reducing plaque development in mice.

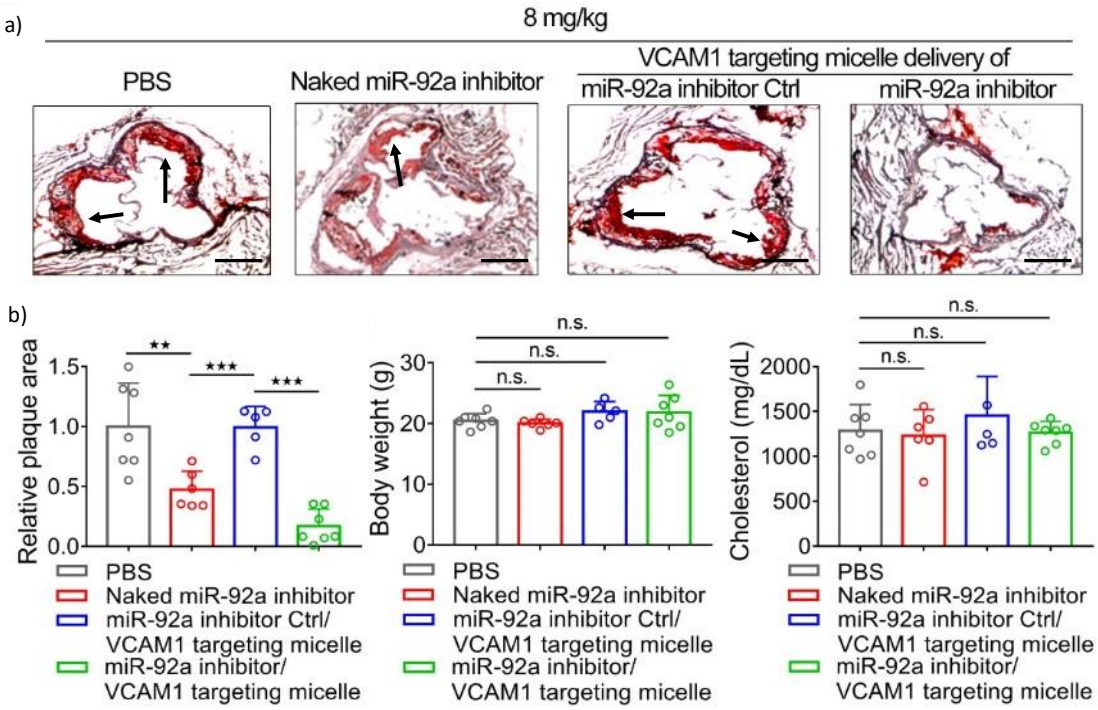

Figure 4.1. *In vivo* results of miR92a-inhibitor delivery via tail vein injection of VCAM-1 targeting PEG2k-PLK30 micelles at 8mg/kg dosage, in collaboration with Yun Fang. a) Aortic root stained with Oil Red O stain shows fewer fatty deposits in aortae treated with miR-inhibiting VCAM1-targeting micelles compared to controls. Arrows point to red-stained fatty plaques. Only miR-inhibitor micelles achieve significant knockdown at the aortic root. Scale bar 200 μm. b) Quantitative measurement of staining indicates miR-inhibitor micelles show significant knockdown in the aorta compared to noninhibitor controls, while micelle-free ("naked") miR-92a inhibitor also shows significant knockdown. Image courtesy of Myung-Jin Oh.

The same experiment was repeated at a 4mg/kg dosage (Figure 4.2). At this reduced dosage the VCAM1-targeting micelles showed nearly 75% reduction of plaques in the VCAM1-targeting micelles and very little reduction in any of the controls, indicating a clear therapeutic effect at the aortic root. The result also indicates a higher degree of therapeutic specificity in the targeting micelles is necessary to achieve effective treatment at the lower dosage.

4.4 Discussion

Earlier study of atherosclerotic plaque development showed that progression of plaques to the fibrous

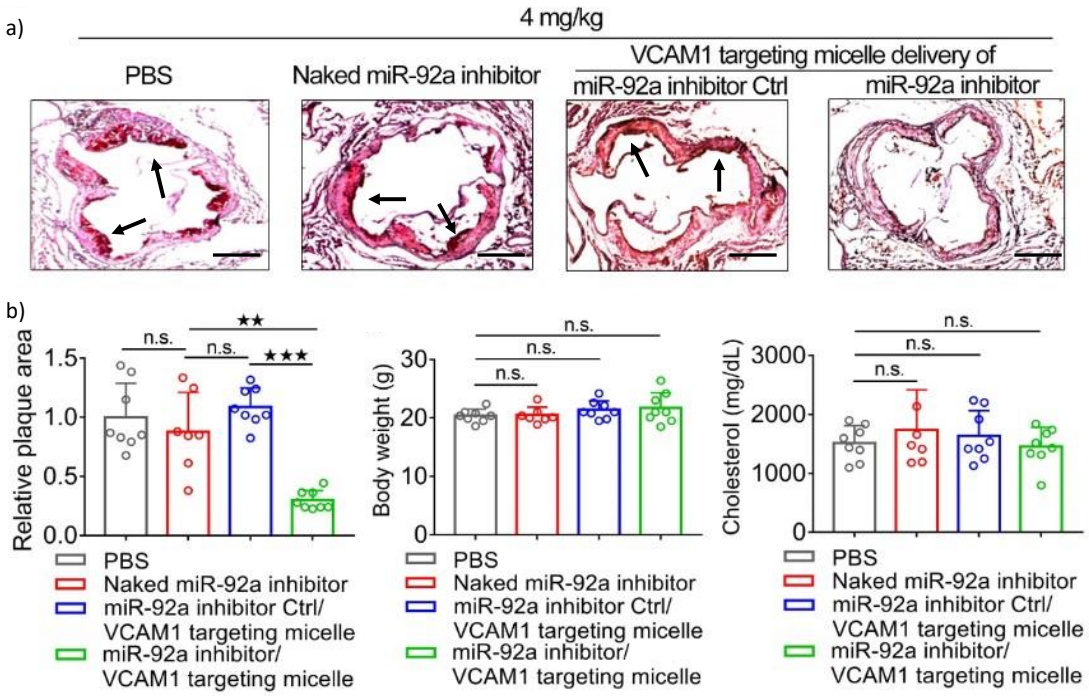

Figure 4.2. *In vivo* results of miR92a-inhibitor delivery via tail vein injection of VCAM-1 targeting PEG2k-PLK30 micelles at 4mg/kg dosage. a) Aortic root stained with Oil Red O stain shows fewer fatty deposits in aortae treated with miR-inhibitor micelles compared to PBS and naked controls. Arrows point to red-stained fatty plaques. Scale bar 200 μm. b) Quantitative measurement shows miR-inhibitor micelles show 75% knockdown in the *en face* aorta compared to noninhibitor micelle control. Control inhibitors and naked miR-92a without micelle do not show significant knockdown, indicating that the micelle formulation is necessary to achieve significant plaque reduction at 4mg/kg dosage. Image courtesy of Myung-Jin Oh.

cap stage indicated higher risk of cardiovascular events. The expression of VCAM-1 at earlier stages of plaque development[43] provides a possibility to prevent advanced plaque formation. We focused on preventing fat deposition in early-stage atherosclerosis by inhibiting miR92a expression, as miR92a has been shown to inhibit KLF2 and KLF4[36], leading to fat deposition, monocyte recruitment and plaque formation at sites of disturbed flow. The reduction of plaque lesion size in mice treated with miR92a inhibitor micelles without significant change in triglyceride or cholesterol levels shows that the plaque reduction is occurring because of physiological changes that prevent fat deposition despite the disturbed flow. This suggests that our micelles are promoting an atheronormal phenotype that resists

plaque development even with the high-fat diet, likely due to the restoration of KLF2 expression. The micelles also show some dose dependence, as the 4 mg/kg shows efficacy at the aortic root while 2 mg/kg (not shown) did not improve outcomes compared to controls. The *en face* analysis of the aortic root shows clear effect, that the micelle delivery of miR-92a inhibitor is reducing plaque burden in the mice. Following the results of this experiment we proceeded to test the relationship of miR-92a to atherosclerotic plaque development, and the effects of disturbed flow, more directly. Those results are shown in Chapter 5. This experiment demonstrated proof of the concept that polyelectrolyte complex micelles can be used as a therapeutic delivery apparatus for hairpin RNA inhibitors. Future experiments can explore the synthesis of polymers with alternative targeting peptides, to target other tissues, and appropriately chosen RNA in the core for therapeutic delivery. As for biological experiments, these micelles can be formulated and tested in porcine models and, eventually, in the clinic for treatment of atherosclerosis.

Chapter Bibliography

1. Miyata, K., Christie, R. J. & Kataoka, K. Polymeric micelles for nano-scale drug delivery. *React. Funct. Polym.* **71**, 227–234 (2011).
2. Kim, Y., Dalhaimer, P., Christian, D. A. & Discher, D. E. Polymeric worm micelles as nano-carriers for drug delivery. *Nanotechnology* **16**, (2005).
3. Lächelt, U. & Wagner, E. Nucleic Acid Therapeutics Using Polyplexes: A Journey of 50 Years (and Beyond). *Chem. Rev.* **115**, 11043–11078 (2015).
4. Cabral, H., Miyata, K., Osada, K. & Kataoka, K. Block Copolymer Micelles in Nanomedicine Applications. *Chemical Reviews* **118**, 6844–6892 (2018).
5. Sagara, K. & Kim, S. W. A new synthesis of galactose-poly(ethylene glycol)-polyethylenimine for gene delivery to hepatocytes. *J. Control. Release* **79**, 271–281 (2002).
6. Reddy, S. T. *et al.* Exploiting lymphatic transport and complement activation in nanoparticle vaccines. *Nat. Biotechnol.* **25**, 1159–1164 (2007).
7. Reddy, S. T., Rehor, A., Schmoekel, H. G., Hubbell, J. A. & Swartz, M. A. In vivo targeting of dendritic cells in lymph nodes with poly(propylene sulfide) nanoparticles. *J. Control. Release* **112**, 26–34 (2006).
8. Oishi, M., Sasaki, S., Nagasaki, Y. & Kataoka, K. pH-Responsive Oligodeoxynucleotide (ODN)−Poly(Ethylene Glycol) Conjugate through Acid-Labile β-Thiopropionate Linkage: Preparation and Polyion Complex Micelle Formation. *Biomacromolecules* **4**, 1426–1432 (2003).
9. Oishi, M., Nagasaki, Y., Itaka, K., Nishiyama, N. & Kataoka, K. Lactosylated poly(ethylene glycol)-siRNA conjugate through acid-labile β-thiopropionate linkage to construct pH-

sensitive polyion complex micelles achieving enhanced gene silencing in hepatoma cells. *J. Am. Chem. Soc.* **127**, 1624–1625 (2005).

10. Christian, D. A. *et al.* Flexible filaments for in vivo imaging and delivery: Persistent circulation of filomicelles opens the dosage window for sustained tumor shrinkage. *Mol. Pharm.* **6**, 1343–1352 (2009).
11. Champion, J. A. & Mitragotri, S. Shape induced inhibition of phagocytosis of polymer particles. *Pharm. Res.* **26**, 244–249 (2009).
12. Venkataraman, S. *et al.* The effects of polymeric nanostructure shape on drug delivery. *Adv. Drug Deliv. Rev.* **63**, 1228–1246 (2011).
13. Champion, J. A., Katare, Y. K. & Mitragotri, S. Particle shape: A new design parameter for micro- and nanoscale drug delivery carriers. *Journal of Controlled Release* **121**, 3–9 (2007).
14. Dalhaimer, P., Engler, A. J., Parthasarathy, R. & Discher, D. E. Targeted worm micelles. *Biomacromolecules* **5**, 1714–1719 (2004).
15. Park, J. H. *et al.* Magnetic iron oxide nanoworms for tumor targeting and imaging. *Adv. Mater.* **20**, 1630–1635 (2008).
16. Kursa, M. *et al.* Novel Shielded Transferrin-Polyethylene Glycol-Polyethylenimine/ DNA Complexes for Systemic Tumor-Targeted Gene Transfer. *Bioconjug. Chem.* **14**, 222–231 (2003).
17. Kanasty, R., Dorkin, J. R., Vegas, A. & Anderson, D. Delivery materials for siRNA therapeutics. *Nature Materials* **12**, 967–977 (2013).
18. Dowdy, S. F. Overcoming cellular barriers for RNA therapeutics. *Nature Biotechnology* **35**, 222–229 (2017).
19. Peters, D. *et al.* Targeting atherosclerosis by using modular, multifunctional micelles. *Proc. Natl. Acad. Sci.* **106**, 9815–9819 (2009).
20. Kuo, C. H. *et al.* Inhibition of atherosclerosis-promoting microRNAs via targeted

polyelectrolyte complex micelles. *J. Mater. Chem. B* **2**, 8142–8153 (2014).

21. Lobatto, M. E., Fuster, V., Fayad, Z. A. & Mulder, W. J. M. Perspectives and opportunities for nanomedicine in the management of atherosclerosis. *Nature Reviews Drug Discovery* **10**, 835–852 (2011).

22. Weber, C. & Noels, H. Atherosclerosis: Current pathogenesis and therapeutic options. *Nature Medicine* **17**, 1410–1422 (2011).

23. Moore, K. J. & Tabas, I. Macrophages in the pathogenesis of atherosclerosis. *Cell* **145**, 341–355 (2011).

24. Swirski, F. K. *et al.* Monocyte accumulation in mouse atherogenesis is progressive and proportional to extent of disease. *Proc. Natl. Acad. Sci. U. S. A.* **103**, 10340–10345 (2006).

25. Siess, W. *et al.* Lysophosphatidic acid mediates the rapid activation of platelets and endothelial cells by mildly oxidized low density lipoprotein and accumulates in human atherosclerotic lesions. *Proc. Natl. Acad. Sci. U. S. A.* **96**, 6931–6936 (1999).

26. Finn, A. V., Nakano, M., Narula, J., Kolodgie, F. D. & Virmani, R. Concept of vulnerable/unstable plaque. *Arterioscler. Thromb. Vasc. Biol.* **30**, 1282–1292 (2010).

27. Higuchi, K. *et al.* Endothelial Gab1 Deletion Accelerates Angiotensin II-Dependent Vascular Inflammation and Atherosclerosis in Apolipoprotein E Knockout Mice. *Circ. J.* **76**, 2031–2040 (2012).

28. De Vos, J. *et al.* Specific Targeting of Atherosclerotic Plaques in ApoE−/−Mice Using a New Camelid sdAb Binding the Vulnerable Plaque Marker LOX-1. *Mol. Imaging Biol.* **16**, 690–698 (2014).

29. Westerterp, M. *et al.* ATP-binding cassette transporters, atherosclerosis, and inflammation. *Circulation Research* **114**, 157–170 (2014).

30. Davies, M. J. *et al.* The expression of the adhesion molecules ICAM-1, VCAM-1, PECAM, and E-selectin in human atherosclerosis. *J. Pathol.* **171**, 223–229 (1993).

31. Nakashima, Y., Raines, E. W., Plump, A. S., Breslow, J. L. & Ross, R. Upregulation of VCAM-1 and ICAM-1 at atherosclerosis-prone sites on the endothelium in the apoE-deficient mouse. *Arterioscler. Thromb. Vasc. Biol.* **18**, 842–851 (1998).

32. Cybulsky, M. I. *et al.* A major role for VCAM-1, but not ICAM-1, in early atherosclerosis. *J. Clin. Invest.* **107**, 1255–1262 (2001).

33. Ley, K. & Huo, Y. VCAM-1 is critical in atherosclerosis. *J. Clin. Invest.* **107**, 1209–1210 (2001).

34. Nahrendorf, M. *et al.* Noninvasive vascular cell adhesion molecule-1 imaging identifies inflammatory activation of cells in atherosclerosis. *Circulation* **114**, 1504–1511 (2006).

35. Broisat, A. *et al.* Nanobodies targeting mouse/human VCAM1 for the nuclear imaging of atherosclerotic lesions. *Circ. Res.* **110**, 927–937 (2012).

36. Wu, C. *et al.* Mechanosensitive PPAP2B Regulates Endothelial Responses to Atherorelevant Hemodynamic Forces. *Circ. Res.* **117**, 41–53 (2015).

37. Small, E. M. & Olson, E. N. Pervasive roles of microRNAs in cardiovascular biology. *Nature* **469**, 336–342 (2011).

38. Fang, Y., Shi, C., Manduchi, E., Civelek, M. & Davies, P. F. MicroRNA-10a regulation of proinflammatory phenotype in athero-susceptible endothelium in vivo and in vitro. *Proc. Natl. Acad. Sci. U. S. A.* **107**, 13450–13455 (2010).

39. Fang, Y. & Davies, P. F. Site-specific microRNA-92a regulation of Krüppel-like factors 4 and 2 in atherosusceptible endothelium. *Arterioscler. Thromb. Vasc. Biol.* **32**, 979–987 (2012).

40. De Winther, M. P. J. & Lutgens, E. MiR-92a: At the heart of lipid-driven endothelial dysfunction. *Circulation Research* **114**, 399–401 (2014).

41. Davies, P. F., Civelek, M., Fang, Y. & Fleming, I. The atherosusceptible endothelium: Endothelial phenotypes in complex haemodynamic shear stress regions in vivo. *Cardiovasc. Res.* **99**, 315–327 (2013).

42. Wu, W. *et al.* Flow-dependent regulation of krüppel-like factor 2 is mediated by MicroRNA-92a. *Circulation* **124**, 633–641 (2011).

43. Chung, E. J. *et al.* In vivo biodistribution and clearance of peptide amphiphile micelles. *Nanomedicine Nanotechnology, Biol. Med.* **11**, 479–487 (2015).

44. Kelly, K. A., Nahrendorf, M., Yu, A. M., Reynolds, F. & Weissleder, R. In vivo phage display selection yields atherosclerotic plaque targeted peptides for imaging. *Mol. Imaging Biol.* **8**, 201–207 (2006).

45. Miyata, K., Nishiyama, N. & Kataoka, K. Rational design of smart supramolecular assemblies for gene delivery: Chemical challenges in the creation of artificial viruses. *Chem. Soc. Rev.* **41**, 2562–2574 (2012).

Chapter 5
Targeted polyelectrolyte complex micelles treat vascular complications *in vivo*

This chapter encompasses an article for submission to *Proceedings of the National Academy of Sciences*, adapted with permission. This chapter provides the context for my work in Chapters 3 and 4, establishing the biological relevance of my work, the necessity of polyelectrolyte micelles to address a major cardiovascular disease via RNA interference, and the interdisciplinary effort involved to bring this work to fruition. In Chapter 4, we explored the use of the polyelectrolyte micelles as a vehicle for delivering miRNA inhibitors. In this chapter, we shall see the Fang group's work showing that the miR-92a pathway is causative of atherosclerosis, my work to characterize micelles formed using an RNA inhibitor of miR-92a, and our collaborative work to show not only that miR-92a expression is reduced by the RNA delivery, but also that the micelles are necessary for effective reduction of atherosclerosis.

Chapter Abstract

Vascular disease is a leading cause of morbidity and mortality in the US and globally. Pathological vascular remodeling such as atherosclerosis and stenosis largely develop at arterial sites of curvature, branching, and bifurcation, where disturbed blood flow activates vascular endothelium. Current pharmacological treatments of vascular complications principally target systemic risk factors. Improvements are needed. We previously devised a targeted polyelectrolyte complex micelle to deliver therapeutic nucleotides to inflamed endothelium *in vitro* by displaying the peptide VHPKQHR targeting

vascular cell adhesion molecule 1 (VCAM-1) on the periphery of the micelle. This paper explores whether this targeted nanomedicine strategy effectively treats vascular complications *in vivo*. Disturbed flow-induced microRNA-92a (miR-92a) has been linked to endothelial dysfunction. We have engineered a new transgenic line (*miR-92a*$^{EC\text{-}TG}$/*Apoe*$^{-/-}$) establishing that selective miR-92a overexpression in adult vascular endothelium causally promotes atherosclerosis in *Apoe*$^{-/-}$ mice. We tested the therapeutic effectiveness of the VCAM1-targeting polyelectrolyte complex micelles to deliver miRNA inhibitors and treat pathological vascular remodeling *in vivo*. VCAM1-targeting micelles preferentially delivered miRNA inhibitors to inflamed endothelium *in vitro* and *in vivo*. The therapeutic effectiveness of anti-miR-92a therapy in treating atherosclerosis and stenosis in *Apoe*$^{-/-}$ mice is markedly enhanced by the VCAM1-targeting polyelectrolyte complex micelles. These results demonstrate a proof of concept to devise polyelectrolyte complex micelle-based targeted nanomedicine approaches treating vascular complications *in vivo*.

5.1 Introduction

Dysfunction of vasculature contributes enormously to human diseases but vascular-wall-targeted therapies are challenging to develop and scant. Current pharmacological treatments for vascular complications mainly address systematic risk factors but do not target the diseased blood vessel. Treatments of vascular disease remain suboptimal. Atherosclerosis, thickening and hardening of arterial walls, is a leading cause of mortality and morbidity in the U.S. and worldwide[1]. Despite well-established systemic risk factors, such as hypercholesterolemia and hypertension, atherosclerosis and pathological vascular remodeling largely occur in vascular sites such as curvatures, bifurcations, and bifurcations where local disturbed blood flow activates vascular endothelial cells[2–5]. In contrast, the straight parts of the artery are exposed to unidirectional flow and are largely resistant to

atherosclerosis. There is tremendous potential to devise innovative therapeutic strategies targeting activated endothelium to treat atherosclerosis and vascular complications.

Predominant roles of microRNA (miRNA) in mediating human diseases, including vascular complications, have been uncovered in recent years[6–8]. Dysregulated miRNAs are attractive therapeutic candidates since a single miRNA typically targets multiple genes that are often within the same pathway[9,10]. Nevertheless, it remains extremely challenging to deliver therapeutic nucleotides targeting dysregulated miRNAs to diseased tissues of interest. Systemic administration of nucleotides has typically resulted in unfavorable pharmacokinetic parameters resulting from rapid *in vivo* degradation and poor cellular uptake, leading to low bioavailability in target cells and unwanted side effects in non-target tissues[7]. Studies by us and others have linked aberrant miRNA expression to key cellular events related to atherosclerosis[10–13]. Specifically, disturbed flow markedly induces miR-92a in endothelial cells to increase vascular inflammation. In addition, reduced atherosclerosis was reported in mice administered a naked form of miR-92a inhibitor RNA in the circulation[14,15]; however, systemic delivery of miR-92a inhibitors was shown to result in miR-92a inhibition in a wide range of tissues in addition to vascular endothelium[14]. It remains to be determined whether increased endothelial miR-92a causatively drives atherosclerosis *in vivo*.

Nucleotide-based therapies could revolutionize future medical practice. For instance, dys-regulated miRNA can be corrected by specific mimics/inhibitors[7]. Polyelectrolyte complex micelles have great potential as gene delivery vehicles due to the ability to encapsulate negatively-charged nucleic acids forming a core by neutralizing the charge, while simultaneously protecting the nucleic acids from non-specific interactions and enzymatic degradation[16,17]. Moreover, we demonstrated that polyelectrolyte complex micelles can be functionalized to display small peptides to drive cell-targeting delivery of therapeutic nucleotides[18]. Limited distribution of pathological vascular remodeling at predictable vascular sites underscores that endothelial inflammation is an attractive target for vascular

wall-based therapies. For instance, disturbed flow markedly up-regulates Vascular Cell Adhesion Molecule 1 (VCAM-1) whose level is high in inflamed endothelium but remains low in healthy endothelium[19–21]. We have previously engineered polyelectrolyte complex micelles which display a targeting peptide (VHPKQHR) against VCAM-1 and encapsulate miRNA inhibitors in the core[18]. The effectiveness of this targeting polyelectrolyte complex micelle in treating atherosclerosis *in vivo* has not been tested.

By engineering a new atherogenic mouse line in which miR-92a is selectively induced in adult vascular endothelium, our data demonstrated the causative action of endothelial miR-92a up-regulation and atherosclerosis *in vivo*, demonstrating that endothelial miR-92a is an attractive therapeutic target for atherosclerosis treatments. Moreover, self-assembled VCAM1-targeting polyelectrolyte complex micelles markedly enhance the therapeutic effectiveness of the miR-92a inhibition strategy to treat atherosclerosis and stenosis induced by disturbed flow. These results provide a proof of principle that innovative targeted nanomedicine approaches can be devised for vascular wall-based therapies treating vascular disease.

5.2 Materials and Methods

5.2.1 Materials

miR92a inhibitor and control double-hairpin RNA were purchased from Dharmacon. N_3-PEG(2000)-MAL and MAL-PEG_{12}-DBCO were purchased from PEGWorks. VHPKQHRGC peptide and Cys-K30 peptide were purchased from Genscript. RNAse-free water and 1x PBS were purchased from New England Biolabs. VHPKQHR-PEG(2000)-PLK30 (VCAM-2k30) was synthesized as a one-pot reaction in pH7.4 buffer by conjugation of Cys-K30 with MAL-PEG_{12}-DBCO to form K30-DBCO, then click chemistry to attach the DBCO-K30 to the N_3-PEG-MAL to make MAL-PEG2k-PLK30,

and finally conjugation with VHPKQHRGC to yield VCAM-2k30. Sample was dialyzed 1 day at 3500 MWCO against MilliQ 18MΩ water to remove any impurities. After dialysis, the sample was lyophilized to yield a fluffy white powder, which was stored at -20°C for stock use.

5.2.2 Formation of miR-92a-Inhibiting Micelles

Stock solutions of nuclease-free 1mM miR-92a inhibitor and miRNA nonsilencing control were prepared, as was 5mg/ml preparations of VCAM-PEG2k-PLK30 in water. The RNA was mixed into nuclease-free 1x PBS by vortexing. VCAM-2k30 was added for a 1:1 P/N ratio of 50 μL sample/mouse, then the solution was vortexed for 30s. Micelles were dialyzed against MilliQ water with a 2000 MWCO membrane overnight. Samples were then collected and diluted to yield 100 μL of injection sample per mouse.

5.2.3 *miR-92a$^{EC\text{-}TG}$/Apoe$^{-/-}$* Triple-transgene Cre-Inducible Mouse Breeding

*mi*R-*92a*^{TG} and *CDH5(PAC)-CreERT2* transgenic mice (Jackson Laboratories) were crossed to obtain *mi*R-*92a*$^{EC\text{-}TG}$ double-transgene mice with tamoxifen-inducible miR-92a expression. *mi*R-*92a*$^{EC\text{-}TG}$ mice were then crossbred with *Apoe*$^{-/-}$ mice to generate triple-transgene mice with ApoE deficiency and inducible miR-92a overexpression.

5.2.4 miR-92a Expression in Endothelial Cells

Triple-transgene mice were administered tamoxifen or PBS for 7 consecutive days at age 7 weeks and fed a high-fat diet of 21% w/w fat, 0.15% w/w cholesterol, 19.5% casein w/w (Harlan) for 10 weeks. Lung endothelial tissue was harvested for real-time PCR assay of miR-92a expression.

5.2.5 Treatment of Atherosclerosis using VCAM-targeting miR-92a Inhibiting Micelles

Mice were fed a high-fat diet of 21% w/w fat, 0.15% w/w cholesterol, 19.5% casein w/w for 8 weeks

starting at age 12 weeks. Mice were shaved and sterilized for tail vein injection of 100 μL of 4 mg/kg or 8 mg/kg of miR inhibitor VCAM-2k30 (N = 7 @ 4 mg/kg, 8 @ 8 mg/kg), negative control miRNA VCAM-2k30 (N = 6, 5), naked miR inhibitor (N = 7, 9), or PBS (N = 8, 8). Micelles were allowed to circulate for 1 week before mice were euthanized for *en face* analysis of aortic arch and root. *En face* analysis was also performed by the Fang lab. After sacrifice, aortas were harvested, fixed with 4% paraformaldehyde overnight at 4 °C, and stained with 2 mg/mL Oil Red O for 20 min. Aortas were rinsed with isopropanol and imaged for plaque size, which was quantified using ImageJ and normalized to average PBS control.

5.3 Results

5.3.1 Endothelial-specific miR-92a overexpression causatively promotes atherosclerosis *in vivo*

To determine the causal role of endothelial miR-92a in atherogenesis *in vivo*, we generated a new *Apoe*$^{-/-}$ mouse line which enables inducible miR-92a overexpression in adult vascular endothelium. We engineered the inducible miR-92a transgenic line (*mi*R-*92a*^{TG}) by inserting the sequence of *mmu-mi*R-*92a* precursor in the ROSA26 locus in the C57BL/6 mice (Fig. 5.1A).The CAG promoter-driven miR-92a transgene was cloned after a PGK-neo-4xPA stop cassette[22] and inactive. The miR-92a transgene then can be activated by removing the PGK-neo-4xPA cassette by Cre recombinase-mediated recombination (Fig. 5.1B). To induce endothelial-specific miR-92a overexpression, the *mi*R-*92a*^{TG} line was bred with the *Cdh5(PAC)-CreERT2* mice with an inducible Cre recombinase under the control of the vascular endothelial cadherin (Cdh5) promoter[23], generating the endothelial-specific miR-92a transgenic mouse line (*mi*R-*92a*$^{EC\text{-}TG}$) (Fig. 5.1A). We then crossed the *mi*R-*92a*$^{EC\text{-}TG}$ mice with the atherogenic ApoE-deficient (*Apoe*$^{-/-}$) mice to generate the *mi*R-*92a*$^{EC\text{-}TG}$/*Apoe*$^{-/-}$ mice (Fig. 5.1A). Cdh5-

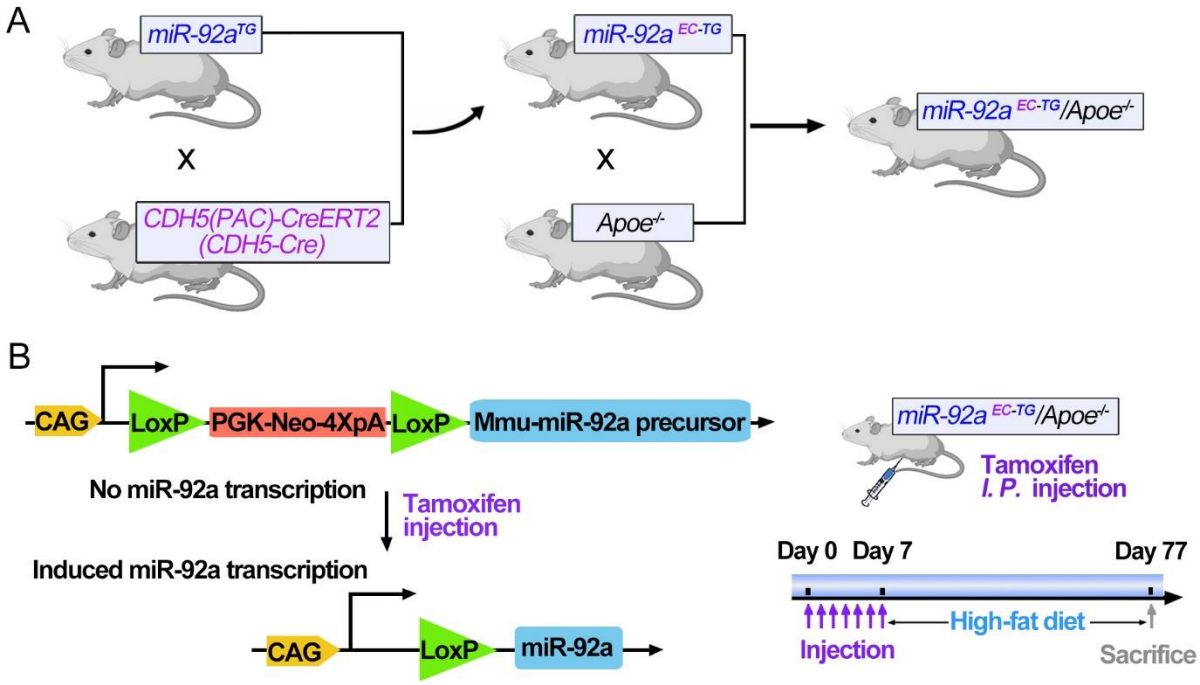
A
miR-92a TG
x
CDH5(PAC)-CreERT2 (CDH5-Cre)
miR-92a EC-TG
x
Apoe-/-
miR-92a EC-TG/Apoe-/-
B
CAG
LoxP
PGK-Neo-4XpA
LoxP
Mmu-miR-92a precursor
No miR-92a transcription
Tamoxifen injection
Induced miR-92a transcription
CAG
LoxP
miR-92a
miR-92a EC-TG/Apoe-/-
Tamoxifen I. P. injection
Day 0
Day 7
Day 77
Injection
High-fat diet
Sacrifice

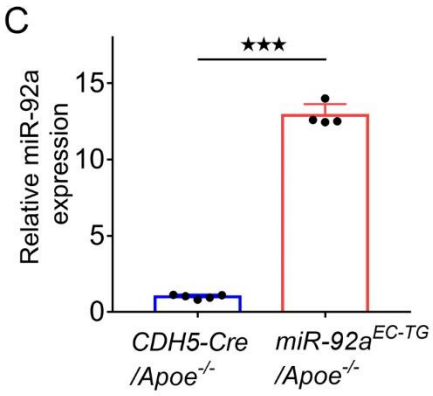
C
Relative miR-92a expression
★★★
CDH5-Cre /Apoe-/-
miR-92aEC-TG /Apoe-/-

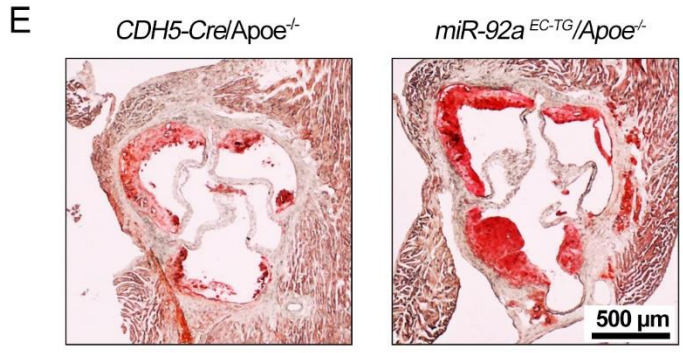
E
CDH5-Cre/Apoe-/-
miR-92a EC-TG/Apoe-/-
500 μm

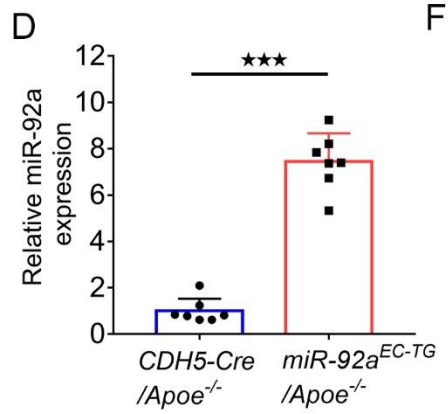
D
Relative miR-92a expression
★★★
CDH5-Cre /Apoe-/-
miR-92aEC-TG /Apoe-/-

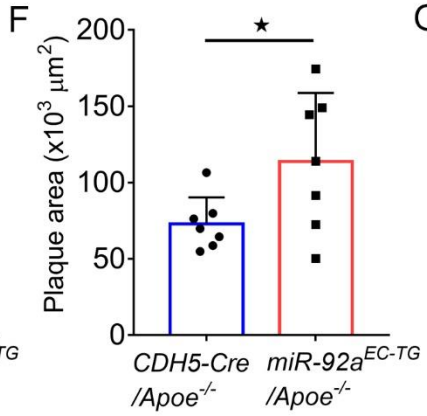
F
Plaque area (x10³ μm²)
★
CDH5-Cre /Apoe-/-
miR-92aEC-TG /Apoe-/-

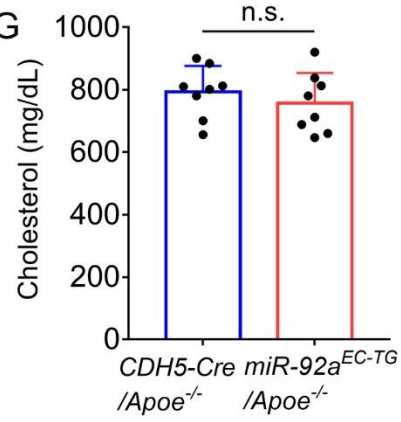
G
Cholesterol (mg/dL)
n.s.
CDH5-Cre /Apoe-/-
miR-92aEC-TG /Apoe-/-

Figure 5.1. Increased atherosclerosis in *Apoe*$^{-/-}$ mice by endothelial-specific overexpression of miR-92a. *(A)* The triple transgenic mice (*mi*R-*92a*$^{EC\text{-}TG}$/*Apoe*$^{-/-}$) were engineered by cross *mi*R-*92a*^{TG} and *CDH5(PAC)-CreERT2 (CDH5-Cre)* mice to obtain *mi*R-*92a*$^{EC\text{-}TG}$, then cross with *Apoe*$^{-/-}$ mice to generate *Apoe*$^{-/-}$ background, containing endothelial specific promotor, and conditional inducible miR-92a overexpression triple transgenic mice. *(B)* Construction of *mi*R-*92a*$^{EC\text{-}TG}$/*Apoe*$^{-/-}$ mice in which miR-92a expression is induced in adult vascular endothelium by tamoxifen-injections. *(C)* Increased miR-92a expression in lung endothelial cells isolated from tamoxifen-injected *mi*R-*92a*$^{EC\text{-}TG}$/*Apoe*$^{-/-}$ mice compared to lung endothelial cells isolated from tamoxifen-injected *Cdh5(PAC)-CreERT2/ Apoe*$^{-/-}$ *(CDH5-Cre/ Apoe*$^{-/-}$*)* mice (n= 4-5 biological samples). *(D)* Increased miR-92a expression in the endothelium-enriched intima of carotid artery in tamoxifen-injected *mi*R-*92a*$^{EC\text{-}TG}$/*Apoe*$^{-/-}$ mice compared to tamoxifen-injected *CDH5-Cre*/*Apoe*$^{-/-}$ mice (n= 7 biological samples). *(E, F)* Reduced atherosclerosis in the aortic root in tamoxifen-injected *mi*R-*92a*$^{EC\text{-}TG}$/ *Apoe*$^{-/-}$ mice compared to tamoxifen-injected *CDH5-Cre*/*Apoe*-/- mice (n= 7 biological samples). *(G)* The plasma cholesterol was not significantly affected by endothelial miR-92a overexpression in tamoxifen-injected *mi*R-*92a*$^{EC\text{-}TG}$/*Apoe*$^{-/-}$ mice compared to tamoxifen-injected *CDH5-Cre*/*Apoe*$^{-/-}$ mice (n= 8 biological samples). Statistical significance determined by multiple unpaired one-tailed t-test. All error bars are means ± standard deviation. n.s., not significant. *P ≤ 0.05; **P ≤ 0.01; ***P ≤ 0.001.

driven Cre recombinase was induced in the *mi*R-*92a*$^{EC\text{-}TG}$/*Apoe*$^{-/-}$ mice by 7 consecutive days of intraperitoneal injection of tamoxifen at week 7, following by 10-weeks high-fat diet feeding (Fig 5.1B). Endothelial miR-92a overexpression was confirmed by real-time PCR demonstrating a 12.9 fold increase of miR-92a in lung endothelial cells isolated from the tamoxifen-treated *mi*R-*92a*$^{EC\text{-}TG}$/*Apoe*$^{-/-}$ mice when compared to tamoxifen-treated *cdh5(PAC)-CreERT2*/*Apoe*$^{-/-}$ mice (Fig. 5.1C). In agreement with this result, we detected a 7.4 fold increase of miR-92a in the endothelium-enriched mouse carotid intima in the tamoxifen-treated *mi*R-*92a*$^{EC\text{-}TG}$/*Apoe*$^{-/-}$ mice when compared to tamoxifen-treated *Cdh5(PAC)-CreERT2*/*Apoe*$^{-/-}$ mice (Fig. 5.1D). Atherosclerotic burdens were quantified in aortic roots. Oil red O staining demonstrated that the lesion size in the aortic root is markedly increased 1.6 fold in tamoxifen-treated *mi*R-*92a*$^{EC\text{-}TG}$/*Apoe*$^{-/-}$ mice compared to those in the tamoxifen-treated *Cdh5(PAC)-CreERT2*/*Apoe*$^{-/-}$ mice (Figs. 5.1E and 5.1F). Neither the plasma cholesterol (Fig. 5.1G) nor the triglyceride (Figure 5.1F) was significantly affected by endothelial miR-92a overexpression. These results demonstrated that that endothelial miR-92a up-regulation causally promotes atherogenesis *in*

vivo.

5.3.2 VCAM1-targeting polyelectrolyte complex micelles effectively encapsulate miR-92a inhibitors

The atherogenic action of endothelial miR-92a (Figs. 5.1E and 5.1F) and its up-regulation by disturbed flow and oxidized low-density lipoprotein[10,14,15,24] suggest that miR-92a inhibition in inflamed endothelium is an attractive strategy to lessen atherosclerotic burdens. We have previously engineered functionalized polyelectrolyte complex micelles, which display targeting peptides against vascular cell adhesion molecule-1 (VCAM-1) expressed in inflamed endothelium, and which simultaneously encapsulate miR-92a inhibitors in the core[18] (Fig. 5.2A). We have further characterized this targeted nanoparticle and its self-assembling process. Briefly, poly-L-lysine (K30) was conjugated to the tail of polyethylene glycol (PEG, molecular weight 2000) to form a maleimide-terminated bio-macromolecular copolymer. A cysteine-modified VCAM1-targeting peptide VHPKQHR[25] was grafted on the head of PEG via thiol-maleimide reaction to form a three block polymers (VHPKQHR-PEG-K30). Poly-L-lysine is biodegradable and biocompatible, and its positive charge effectively complexes negatively charged nucleotides[26]. PEG has been shown to enhance the half-time of nano-materials in circulation[27]. VHPKQHR facilitates active binding and intracellular internalization of nano-materials in inflamed endothelium *in vitro* and *in vivo*[25,28]. To determine the condition by which the VHPKQHR-PEG-K30 polymers completely condense miR-92a inhibitor, we conducted an agarose gel retardation assay showing that a mass ratio (polymer/miR-92a inhibitor) of 2 or above resulted in complete miR-92 inhibitor encapsulation with no miR-92a inhibitor leaching (Fig. 5.2B). Ethidium bromide (EthBr) competitive binding assay further demonstrated the miR-92a inhibitor encapsulation by the VHPKQHR-PEG-K30 polymers (Fig. 5.2C). Specifically, EthBr-stained miRNA inhibitors in the naked form exhibited a strong fluorescence, which was largely abolished when miR-92a inhibitor was

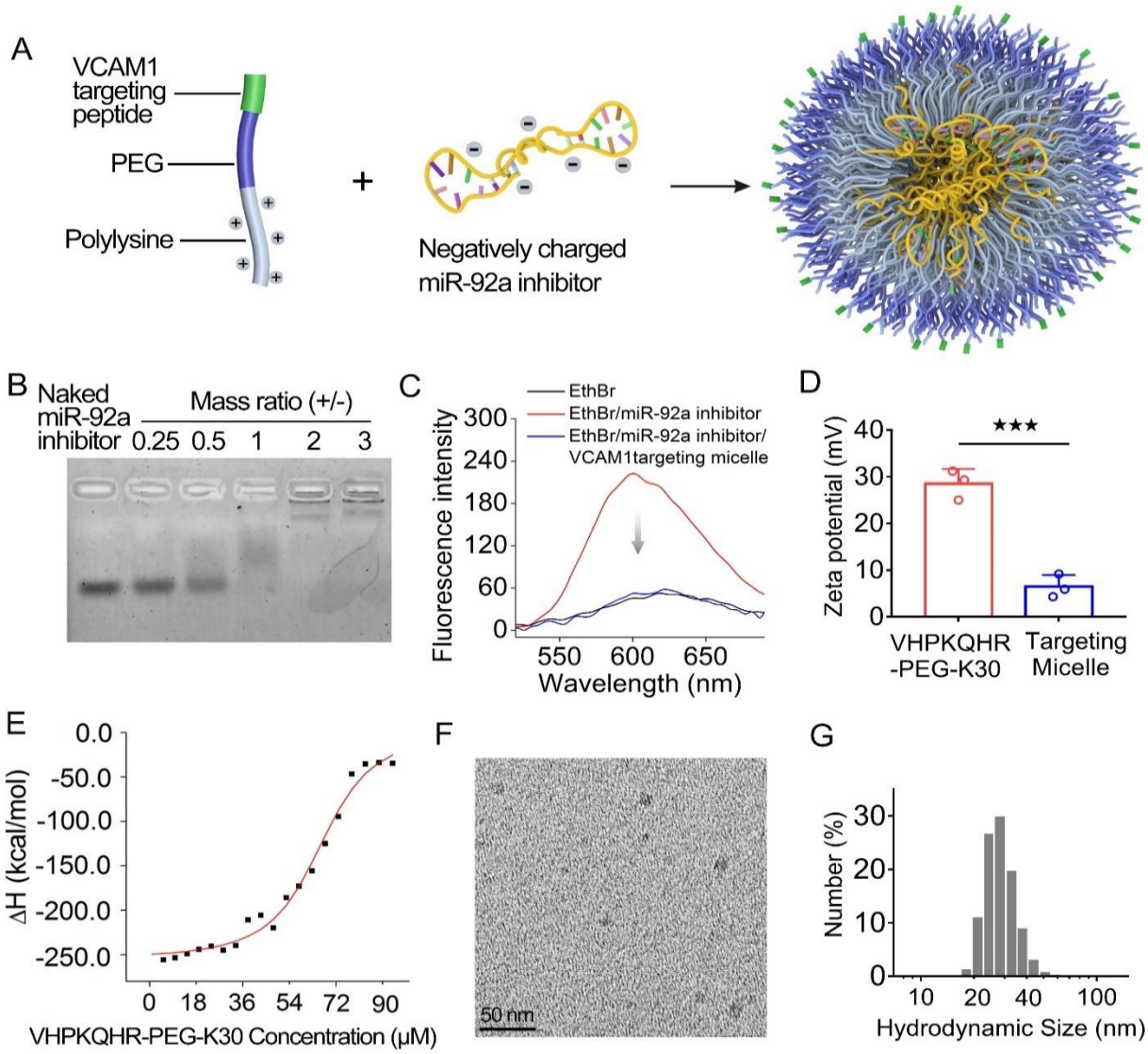

Figure 5.2. The formulation and characterizations of VCAM1-targeting polyelectrolyte complex micelles which encapsulate miRNA inhibitor. *(A)* The illustration of formation of VCAM1-targeting polyelectrolyte complexes encapsulating miRNA inhibitors in the core. *(B)* Condensation of miRNA inhibitor by the VHPKQHR-PEG-K30 at the mass ratio (polymer/miRNA inhibitor) of 2 or above demonstrated by an agarose gel retardation assay. *(C)* Encapsulation of miRNA inhibitor by the VHPKQHR-PEG-K30 demonstrated by the EthBr competitive binding assay. *(D)* Zeta potentials of the VHPKQHR-PEG-K30 and VCAM1-tageting micelles encapsulating miRNA inhibitor (n= 3). *(E)* Isothermal titration calorimetry (ITC) therogram of the assembling of VCAM1-targeting polyelectrolyte complex micelles encapsulating miRNA inhibitor. *(F)* A transmission electron microscopy (TEM) image of miRNA inhibitor encapsulated, VCAM1- targeting polyelectrolyte complex micelles in dry condition. *(G)* The hydrodynamic diameter of the miRNA inhibitor-encapsulated, VCAM1-targeting polyelectrolyte complex micelles. Statistical significance determined by multiple unpaired one-tailed t-test. All error bars are means ± standard deviation. n.s., not significant. *P ≤ 0.05; **P ≤ 0.01; ***P ≤ 0.001.

first mixed with the VHPKQHR-PEG-K30 polymers (Fig. 5.2C). No significant fluorescence was detected in EthBr in aqueous solution alone (Fig. 5.2C). The zeta potential of the VHPKQHR-PEG-K30 polymer was 28.5 mV and reduced to 6.5 mV after the electrostatic complexation with the miR-92a inhibitors (Fig. 5.2D).

We performed isothermal titration calorimetry (ITC) to determine the thermodynamic parameters driving the electrostatically dependent, self-assembly process of the targeted polyelectrolyte complex micelle, showing that it is an exothermic reaction with a decrease of enthalpy (ΔH=-255.2 ± 4.9 kcal/mol) (Fig. 5.2E), consistent with the Gibbs free energy (ΔG) of the binding value of −16.54 kcal/mol (Table. 1). Micelle self-assembly is associated with a negative change of entropy (ΔS=-0.8 kcal/mol/deg), in agreement with the transmission electron microscopy (TEM) images showing monodisperse micelles with a diameter of ~12.5 nm in dry condition (Fig. 5.2F) and a median hydrodynamic diameter of 28.2 nm in deionized (DI) water (Fig. 5.2G). The abovementioned results collectively demonstrate that the electrostatic interaction drives the exothermic self-assembly process to form electrostatically stable monodisperse nanoparticles composed of the VHPKQHR-PEG-K30 polymers and miRNA inhibitor.

VCAM1 Targeting micelle			
Temperature	ΔH (Kcal/mol)	ΔS (Kcal/mol/deg)	ΔG (Kcal/mol)
25.17 °C	-255.2± 4.9	-0.8	-16.54

Table 5.1. Thermodynamic parameters of the formation of VCAM1-targeting polyelectrolyte complex micelles encapsulating miR-92a inhibitor.

5.3.3 VCAM1-targeting polyelectrolyte complex micelles effectively deliver miRNA inhibitors to inflamed endothelial cells *in vitro*

We have determined the efficacy of VCAM1-targeting micelles to deliver miRNA inhibitors to inflamed

endothelium *in vitro*. Dy547-labeled miRNA inhibitors were employed to visualize the cellular uptake. Lipopolysaccharides (LPS) were used to induce inflammation in human aortic endothelial cells (HAEC), resulting in markedly increased expression of inflammatory and adhesive molecules such as

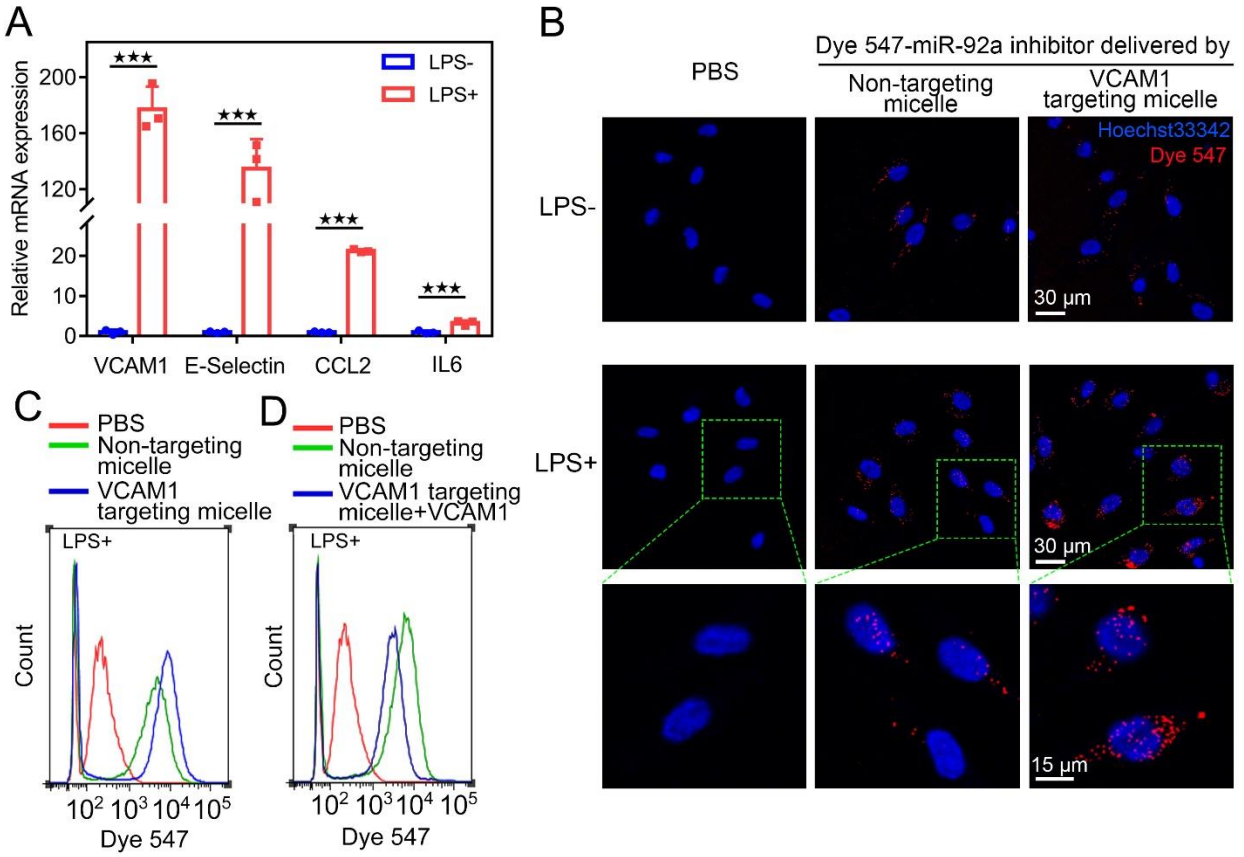

Figure 5.3. Delivery of miRNA inhibitor to inflamed vascular endothelium by VCAM1-targeting polyelectrolyte complex micelles *in vitro*. *(A)* Increased inflammation, demonstrated by elevated expression of VCAM-1, E-Selectin, CCL2, and IL-6 in human aortic endothelial cells (HAEC) treated with lipopolysaccharides (LPS) (n= 3 biological samples). *(B)* Representative confocal images demonstrating the cellular uptake of Dye 547-labeled miRNA inhibitor delivered by VCAM1-targeting polyelectrolyte complex micelles in LPS-treated HAEC but not quiescent control HAEC. Limited cellular uptake of Dy547-labeled miRNA inhibitor, delivered by non-targeting polyelectrolyte complex micelles, in LPS-treated or control HAEC. *(C)* Increased cellular uptake of Dy547-labeled miRNA inhibitor, detected by flow cytometry, by VCAM1-targeting polyelectrolyte complex micelles compared to non-targeting micelles in LPS-treated HAEC. *(D)* Reduced cellular uptake of Dye 547-labeled miRNA inhibitor delivered by VCAM1-targeting micelles in LPS-treated HAEC pre-treated with excess free VCAM1-targeting peptides. Statistical significance determined by multiple unpaired one-tailed t-test. All error bars are means ± standard deviation. n.s., not significant. *P ≤ 0.05; **P ≤ 0.01; ***P ≤ 0.001.

E-Selectin, CCL2, IL-6, and VCAM-1 (Fig. 5.3A). Control or LPS-treated HAEC were incubated with Dy547-labeled miRNA inhibitor (8 μg/mL), delivered by non-targeting or VCAM1-targeting micelles, for 30 mins. Very limited uptake of Dy547-labeled miRNA inhibitor, delivered by the non-targeting micelles was detected by confocal microscopy in control HAECs and in LPS-stimulated cells (Fig. 5.3B). In contrast, we detected a significant uptake of Dy547-labeled miRNA inhibitor when delivered by VCAM1- targeting micelles in LPS-treated HAEC but not in quiescent cells (Fig. 5.3B). Flow cytometry analyses verified a significantly increased Dy547 signal in LPS-stimulated HAEC treated with Dy547-labeled miRNA inhibitor delivered the VCAM1-targeting micelles compared to those delivered by non-targeting nanoparticles (Fig. 5.3C), further supporting an enhanced micelle uptake by the VCAM1-targeting peptide. Pre-treatment of LPS-stimulated HAEC with excess free VCAM1-targeting peptides, which blocked the interaction between the endothelial VCAM-1 and VHPKQHR-displayed micelles, significantly reduced the uptake of Dy547-labeled miRNA inhibitor delivered by the VCAM1-targeting micelles (Fig. 5.3D). Together, these data demonstrate that VCAM1-targeting polyelectrolyte complex micelles effectively deliver miRNA inhibitors to inflamed endothelial cells *in vitro*.

5.3.4 VCAM1-targeting polyelectrolyte complex micelles effectively deliver miRNA inhibitors to inflamed endothelium *in vivo*

We have conducted animal studies showing VCAM1-targeting micelles effectively deliver miRNA inhibitor to inflamed endothelial cells activated by disturbed flow *in vivo*, as described in this section. Partial carotid artery ligation (PCL) was conducted in mice to induce acute disturbed flow in the left carotid artery (Figure 5.4A), which significantly induced VCAM-1 expression in the endothelium. Twenty-four hours after the partial carotid ligations, Dy547-labeled miRNA inhibitor controls (4 mg/kg body weight) were administered to mice via tail veins in the naked form or in complex with non-targeting or VCAM1-targeting micelles (Figure 5.4B). Twenty-four hours after the injections,

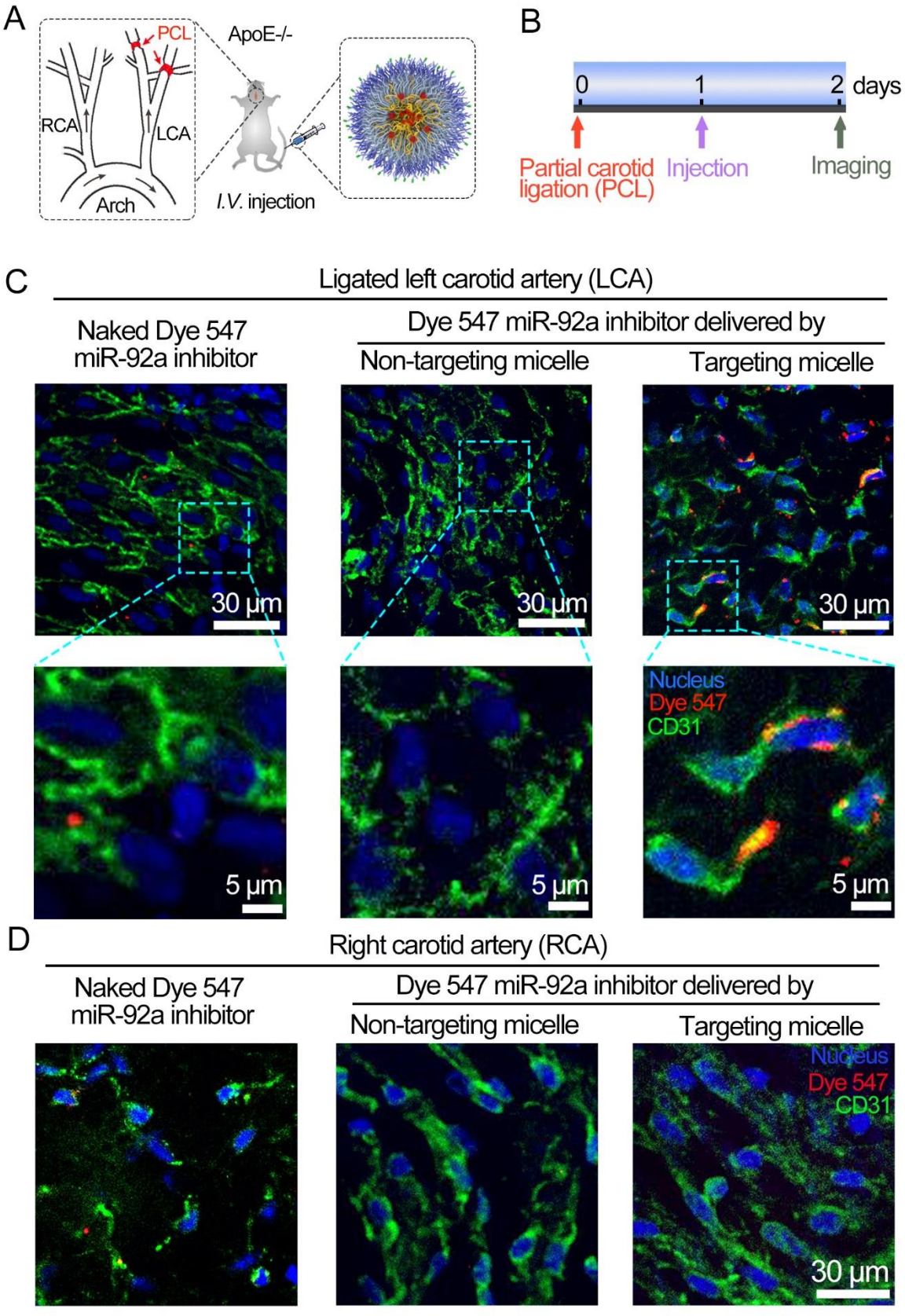
A
PCL
ApoE-/-
RCA
LCA
Arch
I.V. injection
B
0
1
2 days
Partial carotid ligation (PCL)
Injection
Imaging
C
Ligated left carotid artery (LCA)
Naked Dye 547 miR-92a inhibitor
Dye 547 miR-92a inhibitor delivered by
Non-targeting micelle
Targeting micelle
30 μm
5 μm
Nucleus
Dye 547
CD31
D
Right carotid artery (RCA)
Naked Dye 547 miR-92a inhibitor
Dye 547 miR-92a inhibitor delivered by
Non-targeting micelle
Targeting micelle
Nucleus
Dye 547
CD31
30 μm

Figure 5.4. Delivery of miRNA inhibitor to activated vascular endothelium by VCAM1-targeting polyelectrolyte complex micelles *in vivo*. *(A)* A diagram depicting the partial carotid ligation (PCL) in the left carotid artery (LCA) in *Apoe*$^{-/-}$ mice and tail-vein injections of Dye 547-labeled miRNA inhibitor in the naked form or encapsulated in the polyelectrolyte complex micelles. *(B)* The experimental design. *(C) En face* images of ligated left carotid arteries in *Apoe*$^{-/-}$ mice subjected to an injection of Dye 547-labeled miRNA inhibitor in the naked form or encapsulated in micelles. Green: CD31; Blue: nuclei; Red: Dye 547. *(D) En face* images of non-ligated right carotid arteries (RCA) in *Apoe*$^{-/-}$ mice subjected to an injection of Dye 547-labeled miRNA inhibitor in the naked form or encapsulated in micelles. Green: CD31; Blue: nuclei; Red: Dye 547.

mouse carotids were collected, and *en face* immunofluorescence images were taken to determine the cellular uptake of miRNA inhibitors. The Dy547 signaling is negligible in the CD31 positive vascular endothelium in the ligated carotid artery when Dy547-labeled miRNA inhibitors were delivered in the naked form or by non-targeting micelles (Figure 5.4C). In contrast, significant Dy547 fluorescence was detected in the vascular endothelium in the ligated artery when Dy547-labeled miRNA inhibitor control was delivered by VCAM1-targeting nanoparticles (Figure 5.4C). No significant Cy5 signal was detected in the quiescent endothelium in the non-ligated right carotid artery in mice administered with Dy547-labeled miRNA inhibitor controls in the naked form or in complex with non-targeting or VCAM1-targeting micelles (Figure 5.4D). These results collectively demonstrate that VCAM1-targeting polyelectrolyte complex micelles effectively deliver miRNA inhibitors to inflamed endothelium *in vivo*.

5.3.5 VCAM1-targeting, miR-92a inhibitor-encapsulated polyelectrolyte complex micelles significantly reduced aortic atherosclerosis in *Apoe*$^{-/-}$ mice

The therapeutic effectiveness of the VCAM1-targeting polyelectrolyte complex in treating vascular complications was tested *in vivo*. We chose to investigate early-stage atherosclerotic lesions in *Apoe*$^{-/-}$ mice, since previous studies suggested that disturbed flow-induced miR-92a primes vascular endothelium for an enhanced inflammatory response to systemic atherogenic stimuli. The study design is illustrated in Figure 5.5A. *Apoe*$^{-/-}$ mice were fed a high-fat diet starting at 16 weeks of age for 4 weeks

to induce early atherosclerosis. VCAM1-targeting micelles were loaded with either a sequence-scrambled miRNA inhibitor control or miR-92a inhibitors. One tail vein injection of PBS, naked miR-92a inhibitor, or VCAM1-targeting micelles encapsulating miRNA inhibitor controls or miR-92a inhibitors was administered two weeks after the start of high-fat diet (week 18). Inhibitors and inhibitor controls were delivered at 8 mg/kg of body weight. *Apoe*$^{-/-}$ mice were sacrificed at week 20 (after 4 weeks of Western diet) for atherosclerosis analysis.

Oil Red O quantification in aortic roots detected a significant reduction (53%) of atherosclerotic lesions in mice treated with naked miR-92a inhibitors at 8 mg/kg body weight when compared to PBS-treated controls (Figure 5.5B and 5.5C). Notably, aortic root lesion is further decreased when miR-92a inhibitors (8 mg/kg body weight) were administered in the complex with VCAM1-targeting micelles, by 83% when compared to PBS-treated controls and by 36% when compared to mice administered with naked miR-92a inhibitors (Figure 5.5B and 5.5C). There results demonstrated an enhanced therapeutic effectiveness of anti-miR-92a therapy by the VCAM1-targeting polyelectrolyte complex micelle. Aortic lesions were not affected by administration of VCAM1-targeting nanoparticles carrying miRNA inhibitor controls, demonstrating that VCAM-1 targeting itself without miR-92a inhibitors has no effect on atherogenesis. Weight (Figure 5.5D) and plasma cholesterol (Figure 5.5E) in the *Apoe*$^{-/-}$ mice were not changed by the administration of naked miR-92a inhibitors or targeted nanoparticles.

We subsequently conducted the experiments using miR-92a inhibitors at 4 mg/kg body weight, hypothesizing that targeted polyelectrolyte complex micelles will enhance the therapeutic effectiveness of miR-92a inhibitors at a lower dose, using the same study design illustrated in Figure 5.5A. At 4 mg/kg body weight, the naked form of miR-92a inhibitors did not have significant effect on the size of atherosclerotic lesions in the aortic root when compared to those in PBS-treated or sequence scrambled inhibitor controls (Figures 5.5F and 5.5G). However, we detected a marked reduction of aortic root lesions (by 70% when compared to PBS-treated controls) in *Apoe*$^{-/-}$ mice subjected to one

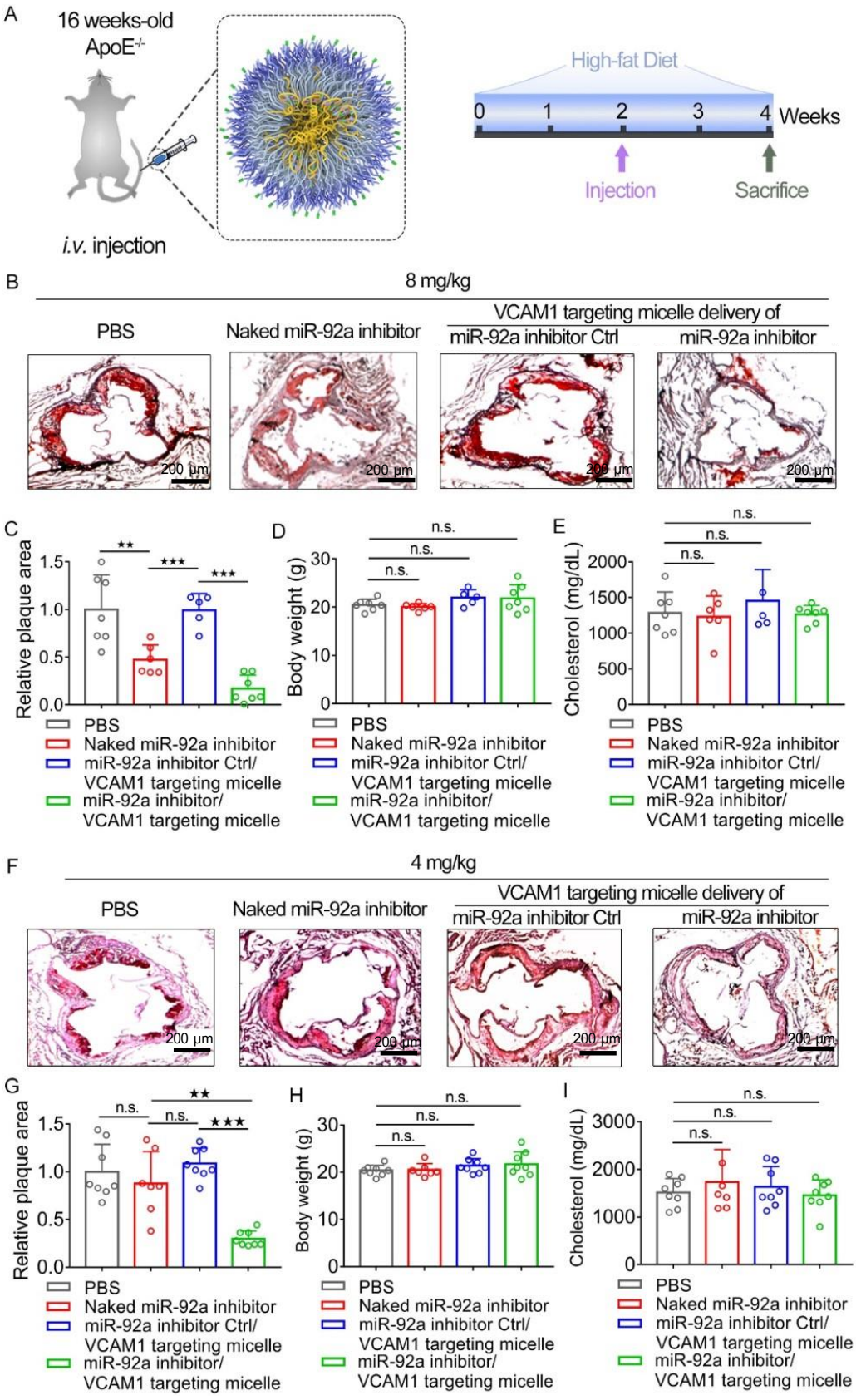
A
16 weeks-old
ApoE-/-
i.v. injection
High-fat Diet
0 1 2 3 4 Weeks
Injection
Sacrifice
B
8 mg/kg
PBS
Naked miR-92a inhibitor
VCAM1 targeting micelle delivery of
miR-92a inhibitor Ctrl
miR-92a inhibitor
200 μm
C
Relative plaque area
D
Body weight (g)
E
Cholesterol (mg/dL)
n.s.
PBS
Naked miR-92a inhibitor
miR-92a inhibitor Ctrl/
VCAM1 targeting micelle
miR-92a inhibitor/
VCAM1 targeting micelle
F
4 mg/kg
G
H
I

Figure 5.5. The therapeutic effectiveness of the anti-miR-92a therapy treating atherosclerosis in *Apoe*$^{-/-}$ mice by VCAM1-targeting polyelectrolyte complex micelles. *(A)* The experimental design. *(B)* Representative images of aortic root lesions in *Apoe*$^{-/-}$ mice subjected to an injection of miR-92a inhibitor (8 mg/kg body weight) in the naked form or encapsulated in VCAM1-targeting micelles or miRNA inhibitor control delivered by VCAM1-targeting micelles. *(C)* Aortic root lesion quantifications in *Apoe*$^{-/-}$ mice subjected to an injection of miR-92a inhibitor (8 mg/kg body weight) in the naked form or encapsulated in VCAM1-targeting micelles or miRNA inhibitor control delivered by VCAM1-targeting micelles) (n= 5-7 biological samples). *(D)* Body weights and *(E)* cholesterol levels of *Apoe*$^{-/-}$ mice subjected to an injection of miR-92a inhibitor (8 mg/kg body weight) in the naked form or encapsulated in VCAM1-targeting micelles or miRNA inhibitor control delivered by VCAM1-targeting micelles (n= 5-7 biological samples). *(F)* Representative images of aortic root lesions in *Apoe*$^{-/-}$ mice subjected to an injection of miR-92a inhibitor (4 mg/kg body weight) in the naked form or encapsulated in VCAM1-targeting micelles or miRNA inhibitor control delivered by VCAM1-targeting micelles. *(G)* Aortic root lesion quantifications in *Apoe*$^{-/-}$ mice subjected to an injection of miR-92a inhibitor (4 mg/kg body weight) in the naked form or encapsulated in VCAM1-targeting micelles or miRNA inhibitor control delivered by VCAM1-targeting micelles) (n= 7-8 biological samples). *(H)* Body weights and *(I)* cholesterol levels of *Apoe*$^{-/-}$ mice subjected to an injection of miR-92a inhibitor (4 mg/kg body weight) in the naked form or encapsulated in VCAM1-targeting micelles or miRNA inhibitor control delivered by VCAM1-targeting micelles (n= 7-8 biological samples). Statistical significance determined by multiple unpaired one-tailed t-test. All error bars are means ± standard deviation. n.s., not significant. *P ≤ 0.05; **P ≤ 0.01; ***P ≤ 0.001.

tail-vein injection of miR-92a inhibitors at 4 mg/kg body weight when encapsulated in VCAM1-targeting polyelectrolyte complex micelles (Figures 5.5F and 5.5G). Lesions were not affected by the injection of VCAM1-targeting micelles carrying sequence-scrambled inhibitor controls. Weight (Figure 5.5H) and plasma cholesterol (Figure 5.5I) in mice were not changed by the administration of naked miR-92a inhibitors or targeted nanoparticles. These results are consistent with previous studies showing high dose (≥16 mg/kg body weight) of naked miR-92a inhibitors conferred anti-atherogenic effects and demonstrated that VCAM1-targeting polyelectrolyte complex markedly enhances the therapeutic effectiveness of miR-92a inhibition therapies treating atherosclerosis *in vivo*.

5.3.6 VCAM1-targeting, miR-92a inhibitor-encapsulated polyelectrolyte complex micelles markedly reduce pathological vascular remodeling induced by acute disturbed flow

We then determined the therapeutic potency of the targeted micelles in reducing pathological vascular

remolding induced by acute disturbed flow. Partial carotid ligations (Figure 5.6A) were performed to induce acute disturbed flow in high fat diet-fed *Apoe*$^{-/-}$ mice, which promotes endothelial inflammation and vascular remodeling. Fourteen days after the ligation, pathological vascular remodeling was shown

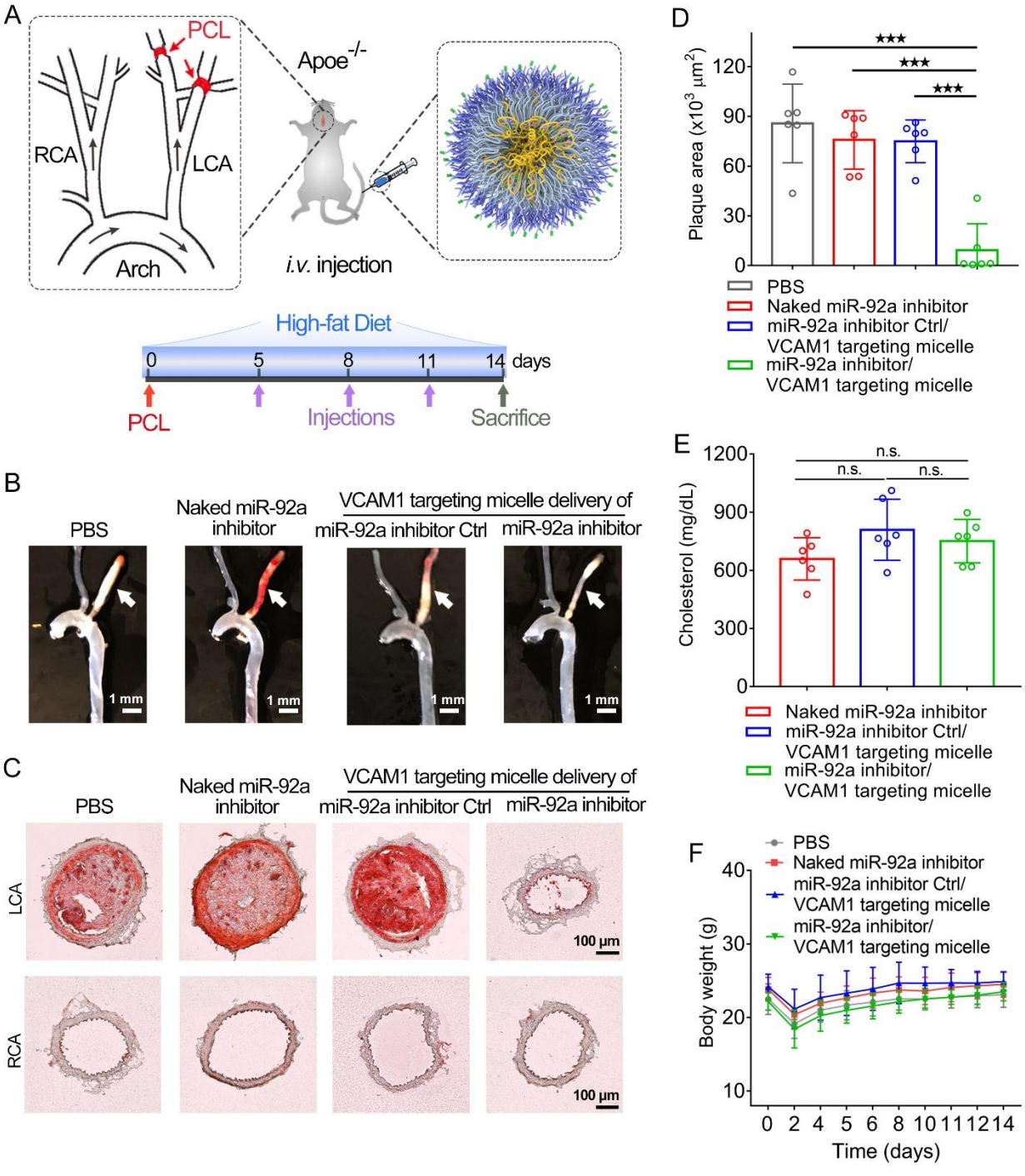

Figure 5.6. The therapeutic effectiveness of the anti-miR-92 therapy treating disturbed flow-induced vascular remodeling in *Apoe*$^{-/-}$ mice by VCAM1-targeting polyelectrolyte complex micelles. *(A)* The experimental design. *(B)* Representative images of disturbed flow-induced vascular remodeling in the ligated left carotid artery in *Apoe*$^{-/-}$ mice subjected to the injections of miR-92a inhibitor (three injections of 2 mg/kg miR-92a inhibitor body weight) in the naked form or encapsulated in VCAM1-targeting micelles or miRNA inhibitor control delivered by VCAM1-targeting micelles. *(C)* Representative cryosection images of the ligated left carotid artery (LCA) and non-ligated right carotid artery (RCA) in in *Apoe*$^{-/-}$ mice subjected to the injections of miR-92a inhibitor (three injections of 2 mg/kg miR-92a inhibitor body weight) in the naked form or encapsulated in VCAM1-targeting micelles or miRNA inhibitor control delivered by VCAM1-targeting micelles. *(D)* Lesion quantifications of the ligated left carotid artery in *Apoe*$^{-/-}$ mice subjected to the injections of miR-92a inhibitor (three injections of 2 mg/kg miR-92a inhibitor body weight) in the naked form or encapsulated in VCAM1-targeting micelles or miRNA inhibitor control delivered by VCAM1-targeting micelles (n= 6 biological samples). (E) Serum cholesterol levels and (F) Body weights of *Apoe*$^{-/-}$ mice subjected to the injections of miR-92a inhibitor (three injections of 2 mg/kg miR-92a inhibitor body weight) in the naked form or encapsulated in VCAM1-targeting micelles or miRNA inhibitor control delivered by VCAM1-targeting micelles (n= 6 biological samples). Statistical significance determined by multiple unpaired one-tailed t-test. All error bars are means ± standard deviation. n.s., not significant. *$P \leq 0.05$; **$P \leq 0.01$; ***$P \leq 0.001$.

by Oil red O staining in the ligated left carotid artery while the right carotid artery developed no sign of vascular remodeling (Figures 5.6B and 5.6C). Administration of miR-92a inhibitors at 2 mg/kg, in the naked form or in complexes with VCAM1-targeting micelles, via the tail vein on day 5, 8, and 11 after the surgery (Figure 5.6A). Histological sections of liver, kidney, lung, and spleen did not detect significant differences in these tissues in mice subjected to injections of miR-92a inhibitor and/or targeted micelles when compared to those in PBS-treated controls. Disturbed flow-induced carotid lesions were markedly reduced (by 89.2 % compared to PBS-injected controls) by the treatment of miR-92a inhibitors delivered by VCAM1-tageting micelles when compared to PBS-injected controls (Figures 5.6B, 5.6C, and 5.6D). In sharp contrast, injections of naked miR-92a inhibitors at the same regimen had no effect on the carotid lesions induced by acute disturbed flow (Figures 5.6B, 5.6C, and 5.6D). Lesion size was not affected by the injections of VCAM1-targeting micelles in complex with inhibitor controls (Figures 5.6B, 5.6C, and 5.6D). Serum cholesterol levels (Figure 5.6E) and body

weights (Figure 5.6F) were not altered by the injections of miRNA inhibitors or nanoparticles. These data again strongly support the enhanced therapeutic effectiveness of anti-miR-92a therapy treating pathological vascular remodeling by the VCAM1-targeting polyelectrolyte complex micelles.

5.4 Discussion

Pathological vascular remodeling, such as occurs in atherosclerosis and stenosis, largely develops at vascular curvatures, bifurcations and branches where endothelial cells are activated by local disturbed flow[2–5]. However, current pharmacological therapies of vascular complications mainly target systematic risk factors but not the diseased vasculature. The focal nature of atherosclerosis provides a unique opportunity to develop novel therapies targeting disease-causing mechanosensitive mechanisms in endothelium induced by disturbed flow. Previous studies have demonstrated that disturbed flow markedly increases miR-92a expression to promote endothelial dysfunction[10,14,15,24] but whether elevated endothelial miR-92a causatively drives atherogenesis *in vivo* remains to be determined. In addition, targeted delivery of therapeutic nucleotides such as miR-92a inhibitors to activated endothelium *in vivo* remains extremely challenging, limiting future translational developments. We engineered, in this work, a new mouse line demonstrating that miR-92a overexpression solely in adult vascular endothelium causatively increases atherosclerosis. Moreover, we devised a precision nanomedicine approach targeting inflamed endothelium employing VCAM1-targeting polyelectrolyte complex micelles, which markedly enhanced the therapeutic effectiveness of the anti-miR-92a therapy in treating atherosclerosis and stenosis in *Apoe*$^{-/-}$ mice. Our results show that dysregulated miRNAs are attractive therapeutic candidates to treat vascular diseases. Moreover, we demonstrated that self-assembled, multi-functional polyelectrolyte complex micelle is an effective nanomedicine strategy to deliver therapeutic nucleotides treating vascular complications *in vivo* (Fig. 5.7).

Blood vessels cover 43,000-75,000 ft^2 surface area in an adult human while vascular disease typically occurs in a very small fraction of this area that is characterized by local inflammation[2–5]. Anti-inflammatory therapy such as Canakinumab which inhibits interleukin-1β provides unequivocal evidence that atherosclerosis can be treated by suppression of inflammation[29]. Nevertheless, controlled

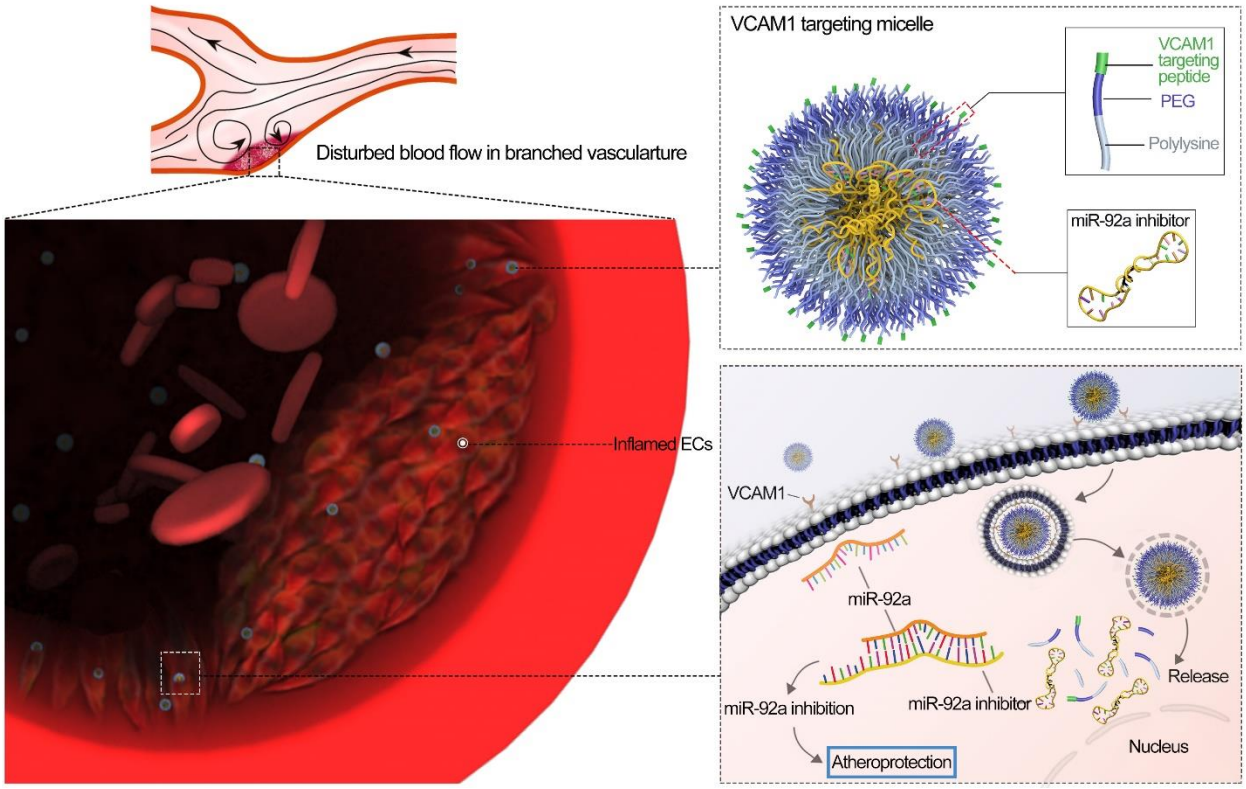

Figure 5.7. Schematic diagram depicting that VCAM1-targeting polyelectrolyte complex micelles deliver miR-92a inhibitor to inflamed endothelial cells treating pathological vascular remodeling induced by local disturbed blood flow.

vascular inflammation is important for tissue homeostasis and host defense against the pathological organisms. Systemic approaches to reduce vascular inflammation carry the inevitable risk of increased pathogen infections and delaying tissue repair. Indeed, a higher incidence of serious and sometimes fatal infections has been reported in patients treated with Canakinumab[29]. Previous studies have suggested that nano-scale systems can be engineered to detect the physical, morphological, and cellular

attributes of vascular diseases[25,30–32]. This study supports the use of nanomedicine, by which innovative nano-carriers are engineered to spatially target inflamed vascular cells, as an attractive strategy to manage local vascular inflammation.

Polyelectrolyte complex micelles are excellent gene delivery vehicles attributable to their ability to encapsulate charged nucleotides forming a core by neutralizing the charges via self-assembling, while simultaneously protecting the nucleic acids from non-specific interactions and enzymatic degradation[16–18]. *In vivo* delivery of therapeutic nucleotides to diseased tissues of interest has often been problematic due to the small size, charge and instability of the nucleic acid[33]. We previously engineered a targeted polyelectrolyte complex micelle that encapsulates miRNA inhibitors in the core and displays targeting peptides against VCAM-1 on the surface[18]. In the current work, we further optimized the formulation and characterized this targeted nanoparticle. Agarose gel retardation, EthBr competitive binding assay, zeta potential measurements, and TEM images collectively demonstrated that miRNA inhibitors were successfully condensed by the VHPKQHR-PEG-K30 polymer, forming a nanometer sized (28 nm) polyelectrolyte complex micelles. Isothermal titration calorimetry measurements demonstrated that this self-assembling process is exothermic with a decrease of enthalpy (ΔH=-255.2 ± 4.9 kcal/mol), consistent with the Gibbs free energy (ΔG) of the binding value of −16.54 kcal/mol. The organization of miRNA inhibitors and PEG-polylysine polymers into a high ordered structure of micelles is supported by the TEM images and negative change of entropy (ΔS=-0.8 kcal/mol/deg) after the self-assembling. Supramolecular assembly driven by non-covalent interactions, such as electrostatic interactions here, is valuable for future functional optimization owing to its facile modularity; minor changes of individual building blocks may fine-tune the properties of the complex[34–36], a process that might be required to translate this application from mice to humans.

Although a tremendously important and prevalent health issue, vascular disease such as atherosclerosis is currently underserved by the nanotechnology community, especially relative to cancer

nanomedicine[37–39]. To address the ongoing challenges of vascular wall-based therapies targeting diseased blood vessels, we engineered the polyelectrolyte complex micelle to display the VCAM1-targeting peptide VHPKQHR. Disturbed flow markedly up-regulates VCAM-1[40], the expression of which increases in activated endothelium but remains low in healthy endothelium[19–21]. Our results demonstrate that the VCAM1-targeting strategy drives active delivery of miRNA inhibitors to inflamed endothelium *in vitro* and to DF-activated endothelium *in vivo*, consistent with previous studies showing that VHPKQHR facilitates VCAM1-mediated intracellular internalization of nanomaterials in endothelium *in vitro* and *in vivo*[25,28]. VCAM-1 is a major endothelial adhesion molecule mediating inflammation-associated vascular adhesion and leukocyte trans-endothelial migration. In addition to pathological arterial remodeling such as atherosclerosis and aneurysm, increased endothelial VCAM-1 is associated in dysfunction of microvasculature such as acute respiratory distress syndrome (ARDS) induced by bacterial or viral (e.g. influenza and SARS-CoV-2 virus) infections[41]. Moreover, elevated VCAM-1 has been implicated in various human disorders, including age-related neurodegeneration, rheumatoid arthritis, asthma, transplant rejection, and cancer[42–44]. These results show a tremendous translational potential of polyelectrolyte complex micelles targeting VCAM-1.

Our new transgenic mouse line established the causal action of increased endothelial miR-92a in atherogenesis, further supporting that endothelial miR-92a is an ideal target for atherosclerotic therapies. Reduced atherosclerosis has been reported in *Ldlr*$^{-/-}$ mice and Angiotensin II-infused *Apoe*$^{-/-}$*/EC-SREBP2(N)-Tg* mice subjected to systemic administration of miR-92a inhibitors[14,15]. Nevertheless, it is possible that miR-92a inhibition in non-endothelial cells contributes to the reduced atherosclerosis since miR-92a is implicated in cellular homeostasis of various cell types such as macrophages[45], smooth muscle cells[46], and lymphocytes[47]. Our results showed that miR-92a induction solely in adult vascular endothelium causatively promotes atherosclerosis in *Apoe*$^{-/-}$ mice, in agreement with the reduced neointimal hyperplasia in the wire-injured iliac artery in mice with miR-92a deletion

in endothelia and leukocytes[48].

Future translational potential of miRNA therapies could be limited by high doses of naked miRNA inhibitors/mimics required to achieve therapeutic effectiveness. Employing naked miR-92a inhibitors, reduced atherosclerosis was reported in *Ldlr*$^{-/-}$ mice subjected to six doses at 8-16 mg/kg body weight[14] and in *Apoe*$^{-/-}$/*EC-SREBP2(N)-Tg* mice administered with two doses at 16 mg/kg body weight[15]. We demonstrated in *Apoe*$^{-/-}$ mice that one injection of naked miR-92a inhibitor at 8 mg/kg body weight, but not at 4 mg/kg body weight, markedly reduced aortic root atherosclerosis. Typically, high-dose and high-frequency of administration is required to compensate the rapid degradation of therapeutic nucleotides in the circulation and poor cellular uptake at the targeted sites[7]. Our results showed that the anti-atherosclerotic action of miR-92a inhibitor at 4 mg/kg body weight can be achieved employing the VCAM1-targeting polyelectrolyte micelle, consistent with its active targeting capacity to inflamed endothelium. A recent clinical trial reported that a single intravenous dose of miR-92a inhibitor ranging from 0.01 to 1.5 mg/kg body weight is well tolerated in human[49]. We tested here the therapeutic effectiveness of miR-92a inhibitor at 2 mg/kg body weight in treating carotid atherosclerosis induced by acute disturbed flow. While three injections of naked miR-92a inhibitor at 2 mg/kg body weight had no effect on the lesion size in the ligated carotid artery, markedly reduced lesions were detected in mice subjected to the same regimen in which miR-92a inhibitor was delivered by VCAM1- targeting polyelectrolyte complex micelles. These results underscore the significance of targeted delivery strategies for nucleotide-based therapies.

In summary, we elucidated the causal role of elevated endothelial miR-92a in atherogenesis and established the therapeutic effectiveness of VCAM1-targeting, miR-92a inhibitor-encapsulated polyelectrolyte complex micelles to lessen atherosclerosis *in vivo*. This study established a proof of concept employing innovative nanomedicine approaches to deliver therapeutic nucleic acids treating

vascular diseases, the current number one killer in the U.S. and globally and projected to remain the single leading cause of death for years to come[1]. Nucleotide-based therapies have unique potential to revolutionize future medical practice. For instance, dysregulated microRNAs (miRNA) can be corrected by specific mimics/inhibitors; disease-causing genes can be silenced by small interfering RNAs; disease-protective genes can be boosted by transcripts; genetic mutations can be corrected by genome editing. The modularity of our polyelectrolyte complex micelle platform allows the capability to present a variety of different cell targeting mechanisms on the micelle corona and to encapsulate various types of nucleotides in the micelle core. It is our long-term goal to achieve tissue-specific manipulation of multiple disease-causing processes with therapeutic nucleotides since most complex human diseases such as atherosclerosis and stenosis are results of various pathological mechanisms in a wide range of cells and contexts.

5.5 Conclusion and Future Directions

Our study shows that VCAM1-targeting miR92a-inhibiting micelles are effective in mice at reducing atherosclerotic plaque burden. Previous work on the development of atherosclerosis demonstrates the causal relationship from disturbed flow to miR92a expression to atherosclerotic plaque buildup. It follows from the results that the successful delivery of miR92a inhibitor prevents plaque formation in inflamed endothelium, by restoring an anti-inflammatory phenotype at sites of disturbed flow. The dose response of the micelle formulation shows that the active targeting of VCAM1 by the micelle construct itself is necessary to deliver miR92a inhibitor at levels sufficient for miR92a knockdown.

This micelle system is also promising for its modularity. The VCAM1 targeting is readily synthesized on the cationic block copolymer, and is orthogonal to the RNA in the core, which should allow mixing and matching of the active targeting and therapeutic properties of the micelle system.

The ease of block copolymer synthesis allows a wide variety of peptide ligands to be used with the PEG2k-PLK30 copolymer, or other polymers as appropriate for delivery. The basic principles shown for the double-hairpin RNA-core micelles can be extended to micelles encapsulating other nucleotides of interest, including dsRNA-like small interfering RNA and single-stranded antisense oligoRNA, with further potential for delivering messenger RNA or genes for transfection. The platform has a high potential for therapeutic and diagnostic use in a wide range of tissues and diseases.

To our knowledge, this is the first study of the structure-assembly relationship of miRNA-like hairpin-ss-hairpin oligonucleotides in a polyelectrolyte complex core micelle. PEG-PLK/nucleic acid micelles are an effective vehicle for RNA delivery, and the elongation of the micelles in saline appears to promote better binding to the target tissue. The PEG2k-PLK30 micelles are a useful vehicle for delivering miRNA inhibitors via active targeting, and many of the same principles of polyelectrolyte complexation of single- and double-stranded nucleic acids apply to the miRNA inhibitors. Some questions remain regarding the structure of the micelles, for example the shape of the aggregates and the causes of the aggregation for micelles functionalized with short cationic peptides. The aggregation is likely to be due to residual RNA not contained within the micelle cores, and the addition of physiological salt concentration should break up the aggregates without affecting the micelles in this hypothesis. Further study of their behavior in saline solution will also help elucidate their behavior after IV injection.

Chapter Bibliography

1. Virani, S. S. *et al.* Heart Disease and Stroke Statistics-2021 Update A Report from the American Heart Association. *Circulation* **143**, E254–E743 (2021).
2. Zhou, J., Li, Y.-S. & Chien, S. Shear Stress–Initiated Signaling and Its Regulation of Endothelial Function. *Arterioscler. Thromb. Vasc. Biol.* **34**, 2191–2198 (2014).
3. Davies, P. F., Civelek, M., Fang, Y. & Fleming, I. The atherosusceptible endothelium: Endothelial phenotypes in complex haemodynamic shear stress regions in vivo. *Cardiovasc. Res.* **99**, 315–327 (2013).
4. Gimbrone, M. A., Jr & García-Cardeña, G. Endothelial Cell Dysfunction and the Pathobiology of Atherosclerosis. *Circ. Res.* **118**, 620 (2016).
5. Hahn, C. & Schwartz, M. A. Mechanotransduction in vascular physiology and atherogenesis. *Nat. Rev. Mol. Cell Biol.* **10**, 53 (2009).
6. Mendell, J. T. & Olson, E. N. MicroRNAs in stress signaling and human disease. *Cell* **148**, 1172 (2012).
7. Rooij, E. van & Olson, E. N. MicroRNA therapeutics for cardiovascular disease: opportunities and obstacles. *Nat. Rev. Drug Discov.* **11**, 860 (2012).
8. Urbich, C., Kuehbacher, A. & Dimmeler, S. Role of microRNAs in vascular diseases, inflammation, and angiogenesis. *Cardiovasc. Res.* **79**, 581–588 (2008).
9. Fang, Y., Shi, C., Manduchi, E., Civelek, M. & Davies, P. F. MicroRNA-10a regulation of proinflammatory phenotype in athero-susceptible endothelium in vivo and in vitro. *Proc. Natl. Acad. Sci. U. S. A.* **107**, 13450–13455 (2010).
10. Fang, Y. & Davies, P. F. Site-specific microRNA-92a regulation of Krüppel-like factors 4 and

2 in atherosusceptible endothelium. *Arterioscler. Thromb. Vasc. Biol.* **32**, 979–987 (2012).

11. Son, D. J. *et al.* The atypical mechanosensitive microRNA-712 derived from pre-ribosomal RNA induces endothelial inflammation and atherosclerosis. *Nat. Commun. 2013 41* **4**, 1–15 (2013).

12. Rayner, K. J. *et al.* MiR-33 contributes to the regulation of cholesterol homeostasis. *Science (80-.).* **328**, 1570–1573 (2010).

13. Marquart, T. J., Allen, R. M., Ory, D. S. & Baldán, Á. miR-33 links SREBP-2 induction to repression of sterol transporters. *Proc. Natl. Acad. Sci. U. S. A.* **107**, 12228–12232 (2010).

14. Loyer, X. *et al.* Inhibition of MicroRNA-92a Prevents Endothelial Dysfunction and Atherosclerosis in Mice. *Circ. Res.* **114**, 434–443 (2014).

15. Chen, Z. *et al.* Oxidative Stress Activates Endothelial Innate Immunity via Sterol Regulatory Element Binding Protein 2 (SREBP2) Transactivation of MiRNA-92a. *Circulation* **131**, 805 (2015).

16. Marras, A. E., Ting, J. M., Stevens, K. C. & Tirrell, M. V. Advances in the Structural Design of Polyelectrolyte Complex Micelles. *J. Phys. Chem. B* **125**, 7076–7089 (2021).

17. Miyata, K., Nishiyama, N. & Kataoka, K. Rational design of smart supramolecular assemblies for gene delivery: Chemical challenges in the creation of artificial viruses. *Chem. Soc. Rev.* **41**, 2562–2574 (2012).

18. Kuo, C. H. *et al.* Inhibition of atherosclerosis-promoting microRNAs via targeted polyelectrolyte complex micelles. *J. Mater. Chem. B* **2**, 8142–8153 (2014).

19. Davies, M. J. *et al.* The expression of the adhesion molecules ICAM-1, VCAM-1, PECAM, and E-selectin in human atherosclerosis. *J. Pathol.* **171**, 223–229 (1993).

20. Nakashima, Y., Raines, E. W., Plump, A. S., Breslow, J. L. & Ross, R. Upregulation of VCAM-

1 and ICAM-1 at atherosclerosis-prone sites on the endothelium in the apoE-deficient mouse. *Arterioscler. Thromb. Vasc. Biol.* **18**, 842–851 (1998).

21. Cybulsky, M. I. *et al.* A major role for VCAM-1, but not ICAM-1, in early atherosclerosis. *J. Clin. Invest.* **107**, 1255–1262 (2001).

22. Mao, J., Barrow, J., McMahon, J., Vaughan, J. & McMahon, A. P. An ES cell system for rapid, spatial and temporal analysis of gene function in vitro and in vivo. *Nucleic Acids Res.* **33**, e155–e155 (2005).

23. Sörensen, I., Adams, R. H. & Gossler, A. DLL1-mediated Notch activation regulates endothelial identity in mouse fetal arteries. *Blood* **113**, 5680–5688 (2009).

24. Wu, W. *et al.* Flow-dependent regulation of krüppel-like factor 2 is mediated by MicroRNA-92a. *Circulation* **124**, 633–641 (2011).

25. Nahrendorf, M. *et al.* Noninvasive vascular cell adhesion molecule-1 imaging identifies inflammatory activation of cells in atherosclerosis. *Circulation* **114**, 1504–1511 (2006).

26. Ahn, C. H., Chae, S. Y., Bae, Y. H. & Kim, S. W. Synthesis of biodegradable multi-block copolymers of poly(l-lysine) and poly(ethylene glycol) as a non-viral gene carrier. *J. Control. Release* **97**, 567–574 (2004).

27. Jokerst, J. V, Lobovkina, T., Zare, R. N. & Gambhir, S. S. Nanoparticle PEGylation for imaging and therapy. *Nanomedicine (Lond).* **6**, 715 (2011).

28. Kheirolomoom, A. *et al.* Multifunctional Nanoparticles Facilitate Molecular Targeting and miRNA Delivery to Inhibit Atherosclerosis in ApoE–/– Mice. *ACS Nano* **9**, 8885–8897 (2015).

29. Ridker, P. M. *et al.* Antiinflammatory Therapy with Canakinumab for Atherosclerotic Disease. *N. Engl. J. Med.* **377**, 1119–1131 (2017).

30. Peters, D. *et al.* Targeting atherosclerosis by using modular, multifunctional micelles. *Proc. Natl.*

Acad. Sci. **106**, 9815–9819 (2009).

31. Mlinar, L. B., Chung, E. J., Wonder, E. A. & Tirrell, M. Active targeting of early and mid-stage atherosclerotic plaques using self-assembled peptide amphiphile micelles. *Biomaterials* **35**, 8678–8686 (2014).

32. Chung, E. J. *et al.* Monocyte-Targeting Supramolecular Micellar Assemblies: A Molecular Diagnostic Tool for Atherosclerosis. *Adv. Healthc. Mater.* **4**, 367–76 (2015).

33. Höbel, S. & Aigner, A. Polyethylenimines for siRNA and miRNA delivery in vivo. *Wiley Interdiscip. Rev. Nanomedicine Nanobiotechnology* **5**, 484–501 (2013).

34. Tu, R. S. & Tirrell, M. Bottom-up design of biomimetic assemblies. *Adv. Drug Deliv. Rev.* **56**, 1537–1563 (2004).

35. Aida, T., Meijer, E. W. & Stupp, S. I. Functional Supramolecular Polymers. *Science* **335**, 813 (2012).

36. Acar, H. *et al.* Self-assembling peptide-based building blocks in medical applications. *Adv. Drug Deliv. Rev.* **110–111**, 65–79 (2017).

37. Chung, E. J. & Tirrell, M. Recent Advances in Targeted, Self-Assembling Nanoparticles to AddressVascular Damage Due to Atherosclerosis. *Adv. Healthc. Mater.* **4**, 2408 (2015).

38. Lewis, D. R., Kamisoglu, K., York, A. W. & Moghe, P. V. Polymer-based therapeutics: nanoassemblies and nanoparticles for management of atherosclerosis. *Wiley Interdiscip. Rev. Nanomedicine Nanobiotechnology* **3**, 400–420 (2011).

39. Gadde, S. & Rayner, K. J. Nanomedicine Meets microRNA. *Arterioscler. Thromb. Vasc. Biol.* **36**, e73–e79 (2016).

40. Wu, C. *et al.* Mechanosensitive PPAP2B Regulates Endothelial Responses to Atherorelevant Hemodynamic Forces. *Circ. Res.* **117**, 41–53 (2015).

41. Huang, R.-T. *et al.* Experimental Lung Injury Reduces Krüppel-like Factor 2 to Increase

Endothelial Permeability via Regulation of RAPGEF3–Rac1 Signaling. *Am. J. Respir. Crit. Care Med.* **195**, 639 (2017).

42. Yousef, H. *et al.* Aged blood impairs hippocampal neural precursor activity and activates microglia via brain endothelial cell VCAM1. *Nat. Med.* **25**, 988 (2019).

43. Kong, D.-H., Kim, Y. K., Kim, M. R., Jang, J. H. & Lee, S. Emerging Roles of Vascular Cell Adhesion Molecule-1 (VCAM-1) in Immunological Disorders and Cancer. *Int. J. Mol. Sci.* **19**, (2018).

44. Schlesinger, M. & Bendas, G. Vascular cell adhesion molecule-1 (VCAM-1)—An increasing insight into its role in tumorigenicity and metastasis. *Int. J. Cancer* **136**, 2504–2514 (2015).

45. Lai, L. *et al.* MicroRNA-92a Negatively Regulates Toll-like Receptor (TLR)-triggered Inflammatory Response in Macrophages by Targeting MKK4 Kinase *. *J. Biol. Chem.* **288**, 7956–7967 (2013).

46. Zhang, L. *et al.* miR-92a inhibits vascular smooth muscle cell apoptosis: role of the MKK4–JNK pathway. *Apoptosis 2014 196* **19**, 975–983 (2014).

47. Xiao, C. *et al.* Lymphoproliferative disease and autoimmunity in mice with elevated miR-17−92 expression in lymphocytes. *Nat. Immunol.* **9**, 405 (2008).

48. Daniel, J.-M. *et al.* Inhibition of miR-92a improves re-endothelialization and prevents neointima formation following vascular injury. *Cardiovasc. Res.* **103**, 564 (2014).

49. Abplanalp, W. T. *et al.* Efficiency and Target Derepression of Anti-miR-92a: Results of a First in Human Study. *Nucleic Acid Ther.* **30**, 335–345 (2020).